

LEONARD SHAW

AFFDL-TM-74-79-FYA

AIR FORCE FLIGHT DYNAMICS LABORATORY
DIRECTOR OF SCIENCE & TECHNOLOGY
AIR FORCE SYSTEMS COMMAND
WRIGHT-PATTERSON AIR FORCE BASE OHIO



AERO-ACOUSTIC ENVIRONMENT OF RECTANGULAR CAVITIES WITH
LENGTH TO DEPTH RATIOS OF FIVE AND SEVEN

D. L. SMITH
L. L. SHAW
R. D. TALMADGE
D. E. SEELEY

April 1974

Approved for public release; distribution unlimited

Reproduced From
Best Available Copy

20000404 037

AQU00-05-0840

AFFDL-TM-74-79-FYA

AERO-ACOUSTIC ENVIRONMENT OF RECTANGULAR CAVITIES
WITH LENGTH TO DEPTH RATIOS OF FIVE AND SEVEN

D. L. SMITH
L. L. SHAW
R. D. TALMADGE
D. E. SEELY

APRIL 1974

Approved for public release; distribution unlimited.

NOTICES

When Government drawings, specifications, or other data are used for any purpose other than in connection with a definitely related Government procurement operation, the United States Government thereby incurs no responsibility nor any obligation whatsoever; and the fact that the Government may have formulated, furnished, or in any way supplied the said drawings, specifications, or other data, is not to be regarded by implication or otherwise as in any manner licensing the holder or any other person or corporation, or conveying any rights or permission to manufacture, use, or sell any patented invention that may in any way be related thereto.

Copies of this report should not be returned unless return is required by security considerations, contractual obligations, or notice on a specific document.

REPORT DOCUMENTATION PAGE			Form Approved OMB No. 0704-0188
<p>Public reporting burden for this collection of information is estimated to average 1 hour per response, including the time for reviewing instructions, searching existing data sources, gathering and maintaining the data needed, and completing and reviewing the collection of information. Send comments regarding this burden estimate or any other aspect of this collection of information, including suggestions for reducing this burden, to Washington Headquarters Services, Directorate for Information Operations and Reports, 1215 Jefferson Davis Highway, Suite 1204, Arlington, VA 22202-4302, and to the Office of Management and Budget, Paperwork Reduction Project (0704-0188), Washington, DC 20503.</p>			
1. AGENCY USE ONLY (Leave blank)	2. REPORT DATE	3. REPORT TYPE AND DATES COVERED	
	APRIL 1974	Final October 1971 - April 1974	
4. TITLE AND SUBTITLE AERO-ACOUSTIC ENVIRONMENT OF RECTANGULAR CAVITY WITH A LENGTH TO DEPTH RATIOS OF FIVE AND SEVEN		5. FUNDING NUMBERS	
6. AUTHOR(S) L.L. SHAW, D.L. SMITH, R.D. TALMADGE, D. E. SEELY			
7. PERFORMING ORGANIZATION NAME(S) AND ADDRESS(ES) Vehicle Dynamics Division Air Force Flight Dynamics Laboratory Dir of Science & Technology Air Force Systems Command Wright-Patterson AFB OH 45433		8. PERFORMING ORGANIZATION REPORT NUMBER	
9. SPONSORING/MONITORING AGENCY NAME(S) AND ADDRESS(ES) Air Force Flight Dynamics Laboratory Dir of Science & Technology Air Force Systems Command Wright-Patterson AFB OH 45433 POC: LEONARD L. SHAW, AFRL/VASS, 937-255-5200		10. SPONSORING/MONITORING AGENCY REPORT NUMBER AFFDL-TM--74-79-FYA	
11. SUPPLEMENTARY NOTES			
12a. DISTRIBUTION AVAILABILITY STATEMENT APPROVED FOR PUBLIC RELEASE, DISTRIBUTION UNLIMITED		12b. DISTRIBUTION CODE	
13. ABSTRACT (Maximum 200 words) The complete program included the flight testing of 5 cavity configurations; three empty cavities, one with an ogive store, and a closed cavity configuration to determine the existing boundary layer characteristics. All flight tests have been completed. The results for one of the empty cavities and the closed cavity were presented in Reference 1 with the results for the remaining three configurations being presented in this report.			
<p>Each of the 5 configurations were tested at constant pressure altitudes of 3,000 ft, 20,000 ft, and 30,000 ft. The range of Mach numbers tested were 0.61 - 0.93 at 3,000 ft and 0.61 - 1.30 for 20,000 ft and 30,000 ft. Continuous data were recorded as the aircraft slowly accelerated from the lowest Mach number to the highest Mach number. For each flight condition, with the open cavity, fluctuating pressures were measured at nine locations in the cavity and static pressures were measured at three cavity locations. In addition vibration levels were measured with an accelerometer. For the closed cavity instrumentation was provided to define the boundary layer characteristics prior to opening the cavity which included a microphone, thermocouple, static pressure port and pressure rake.</p>			
<p>Data were recorded on an FM magnetic tape recorder and data reduction and analysis were performed in the laboratory. Details of the test procedures, instrumentation, data reduction and analysis are given in Appendix A.</p>			
14. SUBJECT TERMS	15. NUMBER OF PAGES 130		
	16. PRICE CODE		
17. SECURITY CLASSIFICATION OF REPORT UNCLASSIFIED	18. SECURITY CLASSIFICATION OF THIS PAGE UNCLASSIFIED	19. SECURITY CLASSIFICATION OF ABSTRACT UNCLASSIFIED	20. LIMITATION OF ABSTRACT SAR

FOREWORD

This research was performed by the Aero-Acoustics Branch, Vehicle Dynamics Division, Air Force Flight Dynamics Laboratory, Wright-Patterson Air Force Base, Ohio. This effort was initiated under Project 1471 "Aero-Acoustic Problems in Flight Vehicles", Task 147102, "Aero-Acoustics".

The work was performed by Messrs. L. L. Shaw, D. L. Smith, and R. D. Talmadge of the Aero-Acoustics Branch and Mr. D. E. Seely of the Aerospace Dynamics Branch, during the period of October 1971 to April 1974. This memorandum covers only the results of three of the five configurations tested. The results of the other two configurations are presented in AFFDL-TM-74-19-FYA "Aero-Acoustic Environment of a Rectangular Cavity with a Length to Depth Ratio of Four".

The manuscript was released by the authors in April 1974 as a technical memorandum.

This technical memorandum has been reviewed and is approved.

Axel W. Kolb
AXEL W. KOLB
Chief, Aero-Acoustics Branch
Vehicle Dynamics Division

TABLE OF CONTENTS

Section	Page
I Introduction.....	1
II Test Program Summary.....	2
III Results.....	3
IV Conclusions	5
Appendix A - Description of Test Article and Instrumentation.....	6
Appendix B - Experimental Procedures and Results..	8
Appendix C - Table and Figures.....	25
References.....	118

LIST OF ILLUSTRATIONS

	Page
Table 1 Pressure Reference Data	26
Figure 1 Standard SUU-41 Munitions Dispenser Pod	27
Figure 2 Standard and Modified SUU-41 Dispenser Pod	28
Figure 3 Modified SUU-41 Pod Mounted on RF-4C Aircraft	29
Figure 4 Modified SUU-41 Pod with 5.7 Inch Deep Cavity	30
Figure 5 Store Containing Cavity Configuration	31
Figure 6 Close-up View of Ogive Store Mounted in the 5.7 Inch Deep Cavity	32
Figure 7 Open Cavity Instrumentation Location	33
Figure 8 Block Diagram of Data Acquisition Instrumentation	34
Figure 9 Data Reduction System	35
Figure 10 One-Third Octave Band Spectra for Open and Closed L/D = 5 Configuration at 3,000 Foot Altitude and Mach 0.82	36
Figure 11 Longitudinal Variation of Static Pressure for L/D = 5 and $P_{\infty} = 6.76$ psia	37
Figure 12 Total Spread of all the Normalized Static Pressure Data	38
Figure 13 Comparison of Current Recovery Factors for L/D = 7 Cavity with Ogive Store to Wind Tunnel Results from Reference 3	39
Figure 14 Thermal Recovery Factors as a Function of Mach Number for L/D = 7 with Ogive Store at an Altitude of 20,000 Feet	40
Figure 15 Narrowband (2 Hz) Spectrum from Microphone C for an Altitude of 20,000 Feet at Mach 0.61 for L/D = 5	41
Figure 16 Narrowband (2 Hz) Spectrum from Microphone C for an Altitude of 20,000 Feet at Mach 0.82 for L/D = 5	42
Figure 17 Narrowband (2 Hz) Spectrum from Microphone C for an Altitude of 20,000 Feet at Mach 1.05 for L/D = 5	43
Figure 18 Narrowband (2 Hz) Spectrum from Microphone C for an Altitude of 20,000 Feet at Mach 1.30 for L/D = 5	44
Figure 19 Narrowband (2 Hz) Spectrum from Microphone C for an Altitude 20,000 at Mach 0.61 for L/D = 7	45

	Page
Figure 20 Narrowband 2 (Hz) Spectrum from Microphone C for an Altitude of 20,000 Feet at Mach 0.82 for L/D = 7	46
Figure 21 Narrowband (2 Hz) Spectrum from Microphone C for an Altitude of 20,000 Feet at Mach 1.05 for L/D = 7	47
Figure 22 Narrowband (2 Hz) Spectrum from Microphone C for an Altitude of 20,000 Feet at Mach 1.30 for L/D = 7	48
Figure 23 Narrowband (2 Hz) Spectrum from Microphone C for an Altitude of 20,000 Feet at Mach 0.61 for L/D = 7 with Store	49
Figure 24 Narrowband (2 Hz) Spectrum from Microphone C for an Altitude of 20,000 Feet at Mach 0.82 for L/D = 7 with Store	50
Figure 25 Narrowband (2 Hz) Spectrum from Microphone C for an Altitude of 20,000 Feet at Mach 1.05 for L/D = 7 with Store	51
Figure 26 Narrowband (2 Hz) Spectrum from Microphone C for an Altitude of 20,000 Feet at Mach 1.30 for L/D = 7 with Store	52
Figure 27 Nondimensional Resonant Frequencies as a Function of Mach Number	53
Figure 28 Acceleration Spectra from Accelerometer J at an Altitude of 3,000 Feet and Mach Number of 0.82	54
Figure 29 Comparison of Actual and Vibration Induced SPL for the L/D = 7 Configuration at a Mach Number of 0.82 and Altitude of 3,000 Feet	55
Figure 30 Overall Time Histories from the Modified SUU-41 Pod for L/D = 5	56
Figure 31 Overall Time Histories from the Modified SUU-41 Pod for L/D = 7	57
Figure 32 One-Third Octave Band Spectra from Microphone A for a Mach Number of 0.82 and L/D Ratio of 5	58
Figure 33 One-Third Octave Band Spectra from Microphone B for a Mach Number of 0.82 and L/D Ratio of 5	59
Figure 34 One-Third Octave Band Spectra from Microphone C for a Mach Number of 0.82 and L/D Ratio of 5	60
Figure 35 One-Third Octave Band Spectra from Microphone D for a Mach Number of 0.82 and L/D Ratio of 5	61

	Page
Figure 36 One-Third Octave Band Spectra from Microphone E for a Mach Number of 0.82 and L/D Ratio of 5	62
Figure 37 One-Third Octave Band Spectra from Microphone F for a Mach Number of 0.82 and L/D Ratio of 5	63
Figure 38 One-Third Octave Band Spectra from Microphone G for a Mach Number of 0.82 and L/D Ratio of 5	64
Figure 39 One-Third Octave Band Spectra from Microphone H for a Mach Number of 0.82 and L/D Ratio of 5	65
Figure 40 One-Third Octave Band Spectra from Microphone I for a Mach Number of 0.82 and L/D Ratio of 5	66
Figure 41 One-Third Octave Band Spectra from Microphone A for a Mach Number of 0.82 and L/D Ratio of 7	67
Figure 42 One-Third Octave Band Spectra from Microphone B for a Mach Number of 0.82 and L/D Ratio of 7	68
Figure 43 One-Third Octave Band Spectra from Microphone C for a Mach Number of 0.82 and L/D Ratio of 7	69
Figure 44 One-Third Octave Band Spectra from Microphone D for a Mach Number of 0.82 and L/D Ratio of 7	70
Figure 45 One-Third Octave Band Spectra from Microphone E for a Mach Number of 0.82 and L/D Ratio of 7	71
Figure 46 One-Third Octave Band Spectra from Microphone F for a Mach Number of 0.82 and L/D Ratio of 7	72
Figure 47 One-Third Octave Band Spectra from Microphone G for a Mach Number of 0.82 and L/D Ratio of 7	73
Figure 48 One-Third Octave Band Spectra from Microphone H for a Mach Number of 0.82 and L/D Ratio of 7	74
Figure 49 One-Third Octave Band Spectra from Microphone I for a Mach Number of 0.82 and L/D Ratio of 7	75
Figure 50 Longitudinal Variation of the Mode 2 Resonant Frequency One-Third Octave Band Peak for L/D = 5	76
Figure 51 One-Third Octave Band Peaks from Microphones C and H for 3,000 Feet Altitude and Mach = 0.82 Depicting L/D Effect	77
Figure 52 Maximum One-Third Octave Band Level as a Function of L/D for 3,000 Feet Altitude and Mach 0.82	78
Figure 53 One-Third Octave Band Spectra from Microphone C at an Altitude of 3,000 Feet for L/D = 5	79

	Page
Figure 54 One-Third Octave Band Spectra from Microphone C at an Altitude of 20,000 Feet for L/D = 5	80
Figure 55 One-Third Octave Band Spectra from Microphone C at an Altitude of 30,000 Feet for L/D = 5	81
Figure 56 One-Third Octave Band Spectra from Microphone C at an Altitude of 3,000 Feet for L/D = 7	82
Figure 57 One-Third Octave Band Spectra from Microphone C at an Altitude of 20,000 Feet for L/D = 7	83
Figure 58 One-Third Octave Band Spectra from Microphone C at an Altitude of 30,000 Feet for L/D = 7	84
Figure 59 One-Third Octave Band Spectra Depicting Mach Number Effect from Microphone C for L/D = 5 and 20,000 Foot Altitude	85
Figure 60 One-Third Octave Band Spectra Depicting Mach Number Effect from Microphone C for L/D = 7 and 20,000 Foot Altitude	86
Figure 61 Comparison of the Prediction Scheme with Data for L/D = 5 from 3,000 Foot Altitude and Mach 0.82	87
Figure 62 Comparison of the Prediction Scheme with Data for L/D = 7 from 3,000 Foot Altitude and Mach 0.82	88
Figure 63 One-Third Octave Band Spectra from the L/D = 5 Configuration Depicting Longitudinal Broadband Variation	89
Figure 64 One-Third Octave Band Spectra from the L/D = 7 Configuration Depicting Longitudinal Broadband Variation	90
Figure 65 One-Third Octave Band Spectra from Microphone H for a Mach Number of 0.82 Depicting L/D Effort	91
Figure 66 Broadband Level Versus Strouhal Number	92
Figure 67 One-Third Octave Band Spectra from Microphone A of the L/D = 7 with Store Configuration at a Mach Number of 0.82	93
Figure 68 One-Third Octave Band Spectra from Microphone B of the L/D = 7 with Store Configuration at a Mach Number of 0.82	94
Figure 69 One-Third Octave Band Spectra from Microphone C of the L/D = 7 with Store Configuration at a Mach Number of 0.82	95

	Page
Figure 70 One-Third Octave Band Spectra from Microphone D of the L/D = 7 with Store Configuration at a Mach Number of 0.82	96
Figure 71 One-Third Octave Band Spectra from Microphone E of the L/D = 7 with Store Configuration at a Mach Number of 0.82	97
Figure 72 One-Third Octave Band Spectra from Microphone F of the L/D = 7 with Store Configuration at a Mach Number of 0.82	98
Figure 73 One-Third Octave Band Spectra from Microphone G of the L/D = 7 with Store Configuration at a Mach Number of 0.82	99
Figure 74 One-Third Octave Band Spectra from Microphone H of the L/D = 7 with Store Configuration at a Mach Number of 0.82	100
Figure 75 One-Third Octave Band Spectra from Microphone I of the L/D = 7 with Store Configuration at a Mach Number of 0.82	101
Figure 76 One-Third Octave Band Spectra from Microphone C of the L/D = 7 with Store Configuration for an Altitude of 3,000 Feet	102
Figure 77 One-Third Octave Band Spectra from Microphone C of the L/D = 7 with Store Configuration for an Altitude of 20,000 Feet	103
Figure 78 One-Third Octave Band Spectra from Microphone C of the L/D = 7 with Store Configuration for an Altitude of 30,000 Feet	104
Figure 79 Comparison of the One-Third Octave Band Spectra from the L/D = 7 Empty and Store Configuration for a Mach Number of 0.61 and Altitude of 3,000 Feet	105
Figure 80 Comparison of One-Third Octave Band Spectra from the L/D = 7 Empty and Store Configuration for a Mach Number of 0.71 and Altitude of 3,000 Feet	106
Figure 81 Comparison of One-Third Octave Band Spectra from the L/D = 7 Empty and Store Configuration for a Mach Number of 0.82 and Altitude of 3,000 Feet	107
Figure 82 Comparison of One-Third Octave Band Spectra from the L/D = 7 Empty and Store Configuration for a Mach Number of 0.93 and Altitude of 3,000 Feet	108

	Page
Figure 83 Comparison of One-Third Octave Band Spectra from the L/D = 7 Empty and Store Configuration for a Mach Number of 0.61 and Altitude of 30,000 Feet	109
Figure 84 Comparison of One-Third Octave Band Spectra from the L/D = 7 Empty and Store Configuration for a Mach Number of 0.82 and Altitude of 30,000 Feet	110
Figure 85 Comparison of One-Third Octave Band Spectra from the L/D = 7 Empty and Store Configuration for a Mach Number of 1.05 and Altitude of 30,000 Feet	111
Figure 86 Comparison of One-Third Octave Band Spectra from the L/D = 7 Empty and Store Configuration for a Mach Number of 1.30 and Altitude of 30,000 Feet	112
Figure 87 Comparison of Measured and Predicted One-Third Octave Band Spectra for L/D = 5 and Mach Number 0.82 at 3,000 Feet Altitude	113
Figure 88 Comparison of Measured and Predicted One-Third Octave Band Spectra for L/D = 7 and Mach Number 0.82 at 3,000 Feet Altitude	114
Figure 89 Comparison of Measured and Predicted One-Third Octave Band Spectra for L/D = 5 at 30,000 Feet Altitude	115
Figure 90 Comparison of Measured and Predicted One-Third Octave Band Spectra for L/D = 7 at 30,000 Feet Altitude	116
Figure 91 Comparison of Spectra from the Working Example and the Prediction Scheme from Reference 3	117

LIST OF SYMBOLS

P_{rms}, P	Root mean square fluctuating pressure
q	Free stream dynamic pressure
M	Free stream Mach number
P_c	Cavity static pressure
P_∞	Free stream static pressure
L	Cavity length
X/L	Nondimensional cavity location
SPL	Sound pressure level
α	Constant
S	Strouhal number (fL/V)
f	Frequency
V	Free stream velocity
D	Cavity depth
K	Ratio of the specific heats (C_p/C_v)
T	Temperature

SUBSCRIPTS

n, m	Integers that define mode number
max	Maximum value
X/L	Nondimensional cavity location

I. INTRODUCTION

Cavities, or rectangular cutouts, exposed to fluid flow can produce an intense aero-acoustic environment. Past experience has shown that severe fluctuating pressures exist in aircraft weapons bays under certain flight conditions. The amplitude of the fluctuating pressures can be sufficiently high to cause structural damage, malfunction of equipment, and problems with store separation and trajectories.

The aero-acoustic phenomena associated with pressure oscillations excited by flow over open cavities has been studied during the past twenty years by several investigators (References 1 - 8). Some knowledge has been gained about the phenomenon but due to the complex nature of the problem, it is not completely understood. Methods to predict the pressure oscillations in shallow cavities have been reported in Reference 3. These methods are empirical and are based on wind tunnel results. A test program was established in the Air Force Flight Dynamics Laboratory to verify and/or refine these data from flight tests. Five cavity configurations were tested. This report presents the results obtained for the cavities with a length to depth ratio (L/D) of 5 and 7. In addition, results from a cavity with a store are included. The measured data were correlated with the empirical wind tunnel aero-acoustic predictions and with the prediction method that resulted from the L/D = 4 data (Reference 1). Equations similar to those used to predict the pressure oscillations for a cavity with L/D = 4 were determined for the other L/D ratios. A brief description of the flight test program is given in Section II and the prediction method for each L/D ratio is presented in Section III. Section IV presents the major conclusions determined from this effort. A detailed description of the cavities, instrumentation and data reduction methods is given in Appendix A. Appendix B presents the test procedure and results, and Appendix C contains all of the Tables and Figures.

II. TEST PROGRAM SUMMARY

The complete program included the flight testing of five cavity configurations; three empty cavities, one with an ogive store, and a closed cavity configuration to determine the existing boundary layer characteristics. All flight tests have been completed. The results for one of the empty cavities and the closed cavity were presented in Reference 1 with the results for the remaining three configurations being presented in this report.

Each of the five configurations were tested at constant pressure altitudes of 3,000 ft, 20,000 ft, and 30,000 ft. The range of Mach numbers tested were 0.61 - 0.93 at 3,000 ft and 0.61 - 1.30 for 20,000 ft and 30,000 ft. Continuous data were recorded as the aircraft slowly accelerated from the lowest Mach number to the highest Mach number. For each flight condition, with the open cavity, fluctuating pressures were measured at nine locations in the cavity and static pressures were measured at three cavity locations. In addition, vibration levels were measured with an accelerometer. For the closed cavity, instrumentation was provided to define the boundary layer characteristics prior to opening the cavity which included a microphone, thermocouple, static pressure port and pressure rake.

Data were recorded on a FM magnetic tape recorder and data reduction and analysis were performed in the laboratory. Details of the test procedures, instrumentation, data reduction and analysis are given in Appendix A.

III. RESULTS

The principal result of this effort is the aero-acoustic environment prediction method. The method is presented in five steps.

STEP I - Determine the resonant frequencies with the modified Rossiter expression (Reference 3):

$$f_m = \frac{V}{L} \frac{\frac{m-0.25}{M}}{\left(1 + \frac{K-1}{2} M^2\right)^{1/2}} + 1.75 \quad m = 1, 2, 3 \quad (1)$$

where V is the free-stream velocity, L is the cavity length and M is the free-stream Mach number.

STEP II - Determine the peak one-third octave normalized SPL for f_1 , f_2 , and f_3 with:

$$20 \log (P_2^{\max}/q) = \begin{cases} -8 + 20 \log (-M^2 + 2M - 0.7) & L/D = 5 \\ -14 + 20 \log (-M^2 + 2M - 0.7) & L/D = 7 \end{cases} \quad (2)$$

$$20 \log (P_1^{\max}/q) = \begin{cases} 20 \log (P_2^{\max}/q) - 6 & L/D = 5 \\ 20 \log (P_2^{\max}/q) - 2 & L/D = 7 \end{cases} \quad (3)$$

$$20 \log (P_3^{\max}/q) = 20 \log (P_2^{\max}/q) \quad L/D = 5, 7 \quad (4)$$

where P_n^{\max} are the maximum fluctuating pressures for each mode frequency; f_n and q is the free-stream dynamic pressure.

STEP III - Determine the peak one-third octave band amplitude at the desired longitudinal position for each resonant frequency with the following equation:

$$20 \log \left(\frac{P_n}{q} \right)_{X/L} = \begin{cases} 20 \log \left(\frac{P_n \max}{q} \right) -10 [2 -X/L -|\cos^{\alpha_n} X/L|] & L/D = 5 \\ 20 \log \left(\frac{P_n \max}{q} \right) -10 [2.7 -1.7 X/L -|\cos^{\alpha_n} X/L|] & L/D = 7 \end{cases} \quad (5)$$

n=1,2,3

where

$$\begin{aligned} \alpha_1 &= 3.5 \\ \alpha_2 &= 6.3 \\ \alpha_3 &= 10.0 \end{aligned}$$

STEP IV - Determine the peak normalized one-third octave band levels of the broadband spectrum at the location in the cavity from:

$$20 \log \left(\frac{P_b}{q} \right)_{X/L} = \begin{cases} 20 \log \left(\frac{P_2 \max}{q} \right) -11 -12 (1 -X/L) & L/D = 5 \\ 20 \log \left(\frac{P_2 \ max}{q} \right) -5 -18 (1 -X/L) & L/D = 7 \end{cases} \quad (6)$$

STEP V - Determine the normalized broadband spectrum from Figure 66.

Another significant finding from the flight test was that dynamic pressure (q) scaling did not account for the total variation in the SPL with altitude for certain cavity locations; however, at two cavity locations scaling with q did account for the complete change in the SPL with a change in the altitude, i.e., the SPL referenced to q was the same for any altitude. This same result was found in Reference 1 for a cavity with an L/D ratio of four. Previous investigators have shown that for a fixed Mach number q scaling accounted for any significant change in the SPL for various pressure altitudes. The reason they did not observe this phenomenon could be due to the cavity positions analyzed. The position selected could be one at which q scaling accounts for all pressure altitude variations.

The prediction method presented above is based on empirical results which were selected to give the highest sound pressure levels in the cavity. Although scaling with q failed at some points in the cavity the predicted levels will be conservative at these locations.

IV. CONCLUSIONS

The experimental investigation reported herein indicates the following conclusions:

1. The cavity resonant frequencies can be accurately predicted by the modified Rossiter formula.
2. The amplitude prediction methods in Reference 3 were conservative in predicting both the resonant and broadband SPL observed in actual flight tests.
3. The method described in the results section is recommended for predicting more realistic SPLs for L/D ratios near 5 and 7 and a Mach number in the range of 0.6 to 1.3.
4. The longitudinal variation of the rms amplitude associated with each resonant frequency can be described as ordered modes.
5. At the rear of the cavity the broadband spectrum for constant flight conditions is nearly the same for all L/D ratios.
6. The maximum broadband levels increased towards the aft end of the cavity by approximately 12 dB for L/D = 5 and 18 dB for L/D = 7.
7. Increasing the L/D ratio reduces the peak amplitude of the resonant frequencies.
8. The fluctuating pressures in the boundary layer 7 inches ahead of the cavity are significantly affected by the cavity resonances. The levels at the resonant frequencies are nearly the same as in the front of the cavity and at frequencies above 500 Hz the levels are increased by about 10 dB.

APPENDIX A

Description of Test Article and Instrumentation

CAVITY MODEL

The cavities were 40 inches long, 9 inches wide, and either 8 inches or 5.7 inches deep. They were constructed with 0.250 inch thick aluminum (6061-T6) with two 1.50 inch X 1.50 inch X 0.25 inch aluminum (6061-T6) angles welded to the bottom for additional support. The additional support raised the natural frequency of the structure, and thus it was hoped that the resonant frequencies of the structure and the acoustic resonant frequencies were far enough apart to prevent significant coupling of the two. An accelerometer was mounted in the floor of the cavity about three-fourths of the distance from the leading edge to measure the structural vibration amplitudes and frequencies to determine whether or not they would interfere with the microphone measurements. The cavities were mounted in a modified SUU-41 munition dispenser pod. A picture of a standard pod is shown in Figure 1* and the necessary modifications are shown in Figure 2. The SUU-41 pod was carried on the triple ejection rack (TER) of the left pylon of the aircraft. Figure 3 schematically illustrates the mounting. A picture of the pod with the 5.7 inch deep ($L/D = 7$) cavity is shown in Figure 4.

The cavity with a L/D ratio of 7 was tested with an ogive store mounted in it as well as empty. Figure 5 shows the relative size of the store with respect to the cavity. It should be noted that the outer edge of the store is $3/4$ of an inch inside the plane of the opening of the cavity. The significance of this will be explained in the results section of the report. A picture of the store mounted in the cavity is shown in Figure 6.

INSTRUMENTATION

The cavities were instrumented with nine microphones, one accelerometer, a thermocouple and three static pressure ports. The location of the instrumentation is shown in Figure 7 with a typical microphone mounting also

* All Tables and Figures referenced are in Appendix C

shown. The type and models of all instrumentation are presented in Figure 8.

The overall system response for the Model 902H crystal accelerometer was flat within \pm 5 percent from 2 to 6000 Hz. The system response for the Model MVA 2100 microphones was flat within 2 dB from 5 to 6000 Hz while the Model MVA 2400 was flat within 2 dB from 2 to 6000 Hz.

The accelerometer was calibrated in the laboratory using a Brüel and Kjaer Type 1606 vibration preamplifier (\pm 1 g calibrator). The microphones were calibrated in the laboratory with a General Radio Type 1552-B sound level calibrator. The measurements system, once installed in the aircraft, was calibrated with an insert voltage to account for signal loss through the cables.

DATA REDUCTION PROCEDURES

All data were continuously recorded on two fourteen channel type recorders. The magnetic tapes recorded in-flight were played back in the laboratory on a Honeywell 7400 record-reproduce system. Overall time histories and one-third octave band analysis were performed over the frequency range of 12.5 Hz to 10,000 Hz using a General Radio multi-channel rms detector interfaced with a 2116 Hewlett-Packard digital computer. The time histories were correlated with the specific flight conditions which were recorded on a voice channel.

For selected microphone and accelerometer data narrowband (2 Hz) analyses were performed using a 9300 power spectral density analyzer. The system linearity is \pm 0.5 dB for a discrete frequency input. Narrowband analysis was also obtained using a Hewlett-Packard 5450 Fourier analyzer. The data reduction system used is schematically shown in Figure 9.

APPENDIX B

Experimental Procedures and Results

TEST PROCEDURES

The three altitudes at which the flight tests were flown are 3,000 ft, 20,000 ft, and 30,000 ft. The tests include flights for the Mach number ranges 0.61 to 0.93 for 3,000 ft and 0.61 to 1.30 for 20,000 ft, and 30,000 ft. Data were obtained at all Mach numbers between the two extremes since the aircraft was slowly accelerated from the lowest to the highest Mach number (approximately 2 to 3 minutes) with data being recorded continuously. The majority of the flights requiring speeds in excess of $M = 0.9$ below 30,000 ft were flown over Lake Huron with the remaining flights being flown over Washington Courthouse, Ohio.

TEST RESULTS

Boundary Layer Characteristics

Data from the flat plate configuration was presented in Reference 1. It was shown that the boundary layer profiles existing at the leading edge of the cavities agree reasonably well with those for fully developed turbulent flow (see Figure 9, Reference 1).

The boundary layer existing at the cavity entrance when the cavity is open is different from that measured for the closed cavity configuration due to the upstream propagation of the pressure fluctuations occurring in the cavity. A comparison is shown in Figure 10 of the spectra from the microphone located upstream from the cavity entrance for the closed and open configuration ($L/D = 5$) at a Mach number of 0.82 and an altitude of 3,000 feet. The boundary layer fluctuating pressure spectrum is significantly affected by the cavity response. Figure 10 also includes the spectra from Microphone C located near the front of the cavity. At the cavity resonances the levels in the boundary layer for the open configuration are seen to be nearly the same as those in the front of the cavity and are considerably higher (~ 40 dB) than those obtained in the closed configuration. At frequencies above 500 Hz the open cavity increases the levels in the boundary layer by about 10 dB and at these frequencies the levels are greater than

they are in the cavity. These effects were found to be true for all of the cavity configurations and all flight conditions. Additional flat plate boundary layer noise measurements from Microphone A for various altitudes and speeds are presented in Reference 1.

Static Pressures

Static pressures were measured at three locations in the cavity. Two pressure transducers were located in the rear half of the floor and one in the aft wall (see Figure 7). The data are presented as the difference between the cavity static pressure P_c and the free-stream static pressure P_∞ normalized with the free-stream static pressure. The data shown in Figure 11 are representative of that for the entire test. It is seen that the cavity static pressure increases towards the rear of the cavity as earlier investigators (References 3, 6, and 8) observed. As the Mach number is increased the static pressure increased reaching its maximum at the maximum speed, however, there were exceptions as can be seen in Figure 11. It must be pointed out that one cannot extrapolate this observation very far beyond the range of the test because it was found in Reference 3 (for wind tunnel tests) that the static pressure at the rear of the cavity starts to decrease around $M = 2$. This trend was also noted in Reference 6.

Static pressure data for all L/D ratios were compared but no apparent trend with L/D was observed. The total spread of all the data recorded (all Mach numbers, all L/D ratios and all altitudes) at each position is shown in Figure 12. The maximum pressure increases towards the rear of the cavity and the total spread in the data increases towards the aft end with the data spread at the rear a factor of 3 greater than at the center.

The cavity with a L/D ratio of 7 was flown with and without an ogive store symmetrically mounted in it. The total spread of the static pressures at each position with the ogive store is also presented in Figure 12. The observed static pressures with the ogive store were generally within the range of those obtained in the empty configuration.

Cavity Temperatures

In the past, investigators have assumed the temperature in the cavity to be nearly equal to the free-stream static temperature as opposed to the free-stream stagnation temperature. Cavity temperatures for wind tunnel tests were presented for the first time in Reference 3 and it was shown that the temperatures inside the cavity approach the free-stream stagnation temperature.

Cavity temperatures were measured in the flight test with a thermo-couple mounted near the center of the aft wall (see Figure 7). The results for the $L/D = 7$ with store configuration are shown in Figure 13, along with wind tunnel results from Reference 3. It can be seen that the wind tunnel data show a trend for the cavity temperature to approach the stagnation temperature with increasing Mach number. At the lower Mach numbers the flight data fall well above the wind tunnel results but at supersonic speeds the data agree quite well. The reason for high recovery factors at the lower speeds is believed to be due to the flight profiles. The sequence of recording data was generally from the lowest altitude to the highest, thus the cavity walls would be at a temperature above the stagnation temperature each time the aircraft changed altitude. It is believed that this temperature excess is the cause of the higher recovery factors at the lower Mach numbers. Figure 14 shows two consecutive runs at an altitude of 20,000 ft displaying a reduction in recovery factors for the second set of temperature measurements. This tends to substantiate the above explanation since the second temperature measurements are for the same flight conditions at a later time and the cavity wall temperature was lower due to the increased soak time. The reduction in recovery factors for the second set indicates that the measured temperature is affected by the duration of time the aircraft is at the same altitude.

Due to anomalies in the temperature measurements, acceptable data were obtained for only two test configurations, $L/D = 7$ with store and $L/D = 5$. The $L/D = 5$ results displayed the same trend as for the $L/D = 7$ with store configurations presented in Figure 13. Thus, it appears that L/D ratio or

the addition of a store does not affect the temperature trend in the cavity and it is concluded that the temperature in a cavity exposed to free-stream flow approaches the free-stream stagnation temperature as was found in the wind tunnel tests of Reference 3.

Resonant Frequencies

Narrowband (2 Hz) frequency spectra were obtained from various microphone locations to identify the discrete resonant frequencies in the recorded data. Typical narrowband spectra are shown in Figures 15 - 26 for Microphone C at an altitude of 20,000 ft and various Mach numbers and for the three test configurations. The predicted resonant frequencies are depicted in the figures by dashed lines for the first three modes. The narrowband energy distribution is more apparent in the higher Mach number spectra. The nondimensional resonant frequencies or Strouhal number ($S = fL/V$) were calculated for each observed resonant frequency f . The free-stream velocity was calculated from the free-stream static temperature and measured Mach number. Only those resonant frequencies that were about 5 dB or more above the broadband level were used to calculate the nondimensional frequencies. The calculated Strouhal numbers for all three L/D ratios are presented in Figure 27 along with the data from Reference 3 for L/D ratios of 4, 5.7, and 7. The solid curves represent the modified Rossiter equation for the Strouhal relation given by:

$$S = \frac{\frac{m - 0.25}{M}}{\left(1 + \frac{K-1}{2} M^2\right)^{1/2}} + 1.75 \quad m = 1, 2, 3 \quad (1)$$

It is seen that the nondimensional resonant frequencies vary little with the L/D ratio. Variations in the ambient pressure (altitude) also had little effect as the data in Figure 27 include all test altitudes. The addition of a store did not affect the frequency as can also be seen in the figure. It was observed in Reference 3 that the resonant frequencies were relatively

insensitive to variations in these variables but they determine in an unknown way the "occurrence" of the discrete frequencies.

The modified Rossiter formula, Equation (1), is seen in Figure 27 to be a good fit to the flight data and is thus recommended for predicting the resonant frequencies of a cavity with L/D ratios between 4 and 7.

Vibration Levels

The vibration levels were measured by an accelerometer mounted on the floor of the cavity at 3/4 of the cavity length from the leading edge (see Figure 7). Data were recorded continuously by the same instrumentation as that used with the microphones and one-third octave band analyses were performed for various test conditions. A typical spectrum for each test configuration is shown in Figure 28. There is only a small difference between the L/D = 5 and L/D = 7 spectra. A significant reduction in the low frequencies is seen in the spectrum from the store configuration.

The vibration sensitivity of the microphones used was 90 dB/1g, i.e., 1g of acceleration of the microphone would produce not more than a 90 dB reading. Figure 29 shows the measured spectra for Microphone E (the nearest one to the accelerometer, see Figure 7) along with the corresponding spectra induced in a microphone due to the measured acceleration for an altitude of 3,000 ft and a Mach number of 0.82. There is a 30 dB or more difference between the two curves at all frequencies, therefore, it can be assumed that the vibration effect on the microphones was insignificant. It was also assumed throughout the report that the acoustic energy input to the system from the vibration of the walls was negligible.

Fluctuating Pressures

Fluctuating pressures were measured at the nine locations shown in Figure 7 for all three test altitudes. The data were obtained from microphones at these locations and were recorded continuously as the aircraft slowly accelerated from the lowest to the highest Mach number. The

recorded data were analyzed at approximately every 0.1 Mach number using a two second sample time. For the frequencies of interest this insures a good statistical representation of the data. Throughout the report the fluctuating pressures are either presented as sound pressure levels referenced to 20 $\mu\text{N}/\text{m}$ or are normalized to the free-stream dynamic pressure (q) and presented logarithmically. The dynamic pressures were computed from the free-stream Mach number and free-stream static pressures. These are presented in Table 1 for each pressure altitude and Mach number. In addition Table 1 includes the quantity required to convert the logarithmic normalized fluctuating pressures to sound pressure levels, i.e., add the last columns of Table 1 to 20 $\log p/q$ to obtain the sound pressure level referenced to 20 $\mu\text{N}/\text{m}$.

The overall fluctuating pressure time histories from Microphone C for all three altitudes and a L/D ratio of 5 are presented in Figure 30 with the same data for a L/D ratio of 7 presented in Figure 31. These time histories are representative of all the data observed except the spread between the data at each altitude differs at different positions along the cavity. This variation will be discussed in greater detail below when the one-third octave band data are presented.

The time histories indicate that the overall SPL increases with Mach number to some maximum value and then decreases with further increases in the Mach number. It appears that the Mach number which corresponds to the maximum SPL is a function of the L/D ratio. The time histories for the L/D = 5 configuration indicate a Mach number of about 1.25 for the maximum overall SPL while L/D = 7 data show that the maximum occurs about 1.15. If these values are extrapolated linearly to an L/D ratio of 4, a Mach number of 1.30 would be predicted for the maximum SPL. The time histories for the L/D = 4 configuration presented in Reference 1 displayed no maximum for Mach numbers up to 1.30. In light of the present data this is expected since the maximum SPL should occur near Mach 1.30 and no data were available for higher Mach numbers.

Figures 32 through 40 present the one-third octave band spectra from Microphone A through I at a Mach number of 0.82 for the L/D ratio of 5.

The same data for the L/D ratio of 7 are presented in Figures 41 through 49. Data for each test altitude (3,000 ft; 20,000 ft, 30,000 ft) are included. The resonant peaks in the spectra are evident and appear most strongly at the lowest altitude. It is also evident that the deeper cavity displays higher SPLs for the same conditions. The data for the L/D ratio of 4, Reference 1, indicated that dynamic pressure scaling did not account for the total spread in the data at all microphone locations. It was shown that the only positions in the cavity that scaled reasonably well were at $X/L = 0$ and 0.5 with the other microphone locations failing by as much as 30 dB. The flight data from the other two L/D ratios follow the same trend, i.e., dynamic pressure scaling accounts for the total spread in the data only at cavity locations $X/L = 0$ and $X/L = 0.5$. The lack of scaling for the mode 2 frequency of the $L/D = 5$ configuration at a Mach number of 0.82 can easily be seen in Figure 50. At $X/L = 1.0$ there is 28 dB spread in the scaled data.

It was shown in Reference 3 that the longitudinal variation of the mode frequency amplitudes could be described as ordered modes. Ramped sinusoidal functions were used to define these mode shapes and they were fit to the 3,000 ft data in Reference 1. The accuracy of the fit was very good. Since q scaling fails at certain cavity locations, considerable conservatism (for the higher altitudes) will result when predicting the aero-acoustic environment in the cavity at those positions that do not scale, however, from an engineering standpoint this conservatism is acceptable. The same approach was used with the data presented in this report, i.e., only the 3,000 ft data were used to modify the prediction equations.

The data for L/D ratios of 5 and 7 were compared to the mode shape equation derived for the $L/D = 4$ configuration. The curves did not fit the data very well with differences as large as 20 dB. These large differences are attributed to two major variations in the aero-acoustic environment. First, the increase in the SPL from the fore end to the aft end of the cavity is greater for the shallower cavities. Wind tunnel data (References 3 and 6) indicate the same trend. Figure 51 displays this trend by presenting one-third octave band peak data from Microphones C and H, which are

located in the fore and aft end respectively, for a Mach number of 0.82 and altitude of 3,000 ft. The increase for $L/D = 4$ is about 7 dB and for $L/D = 7$ it is around 18 dB. This would result in about an 11 dB error if the prediction equations do not account for this variation. Second, the amplitude of the mode 2 frequencies decrease for larger L/D ratios. It is seen in Figure 51 that the mode 2 amplitude at the rear of the cavity (Microphone H) decreases 12 dB for the L/D variation while the mode 2 amplitude at the front of the cavity (Microphone C) decreases about 23 dB. This results in an 11 dB increase in the amplitude rise towards the rear of the cavity for the range of L/D ratios presented.

The other mode frequencies did not follow the same trend as mode 2 as can be seen in Figure 52. Mode 1 amplitude increases around 1 dB at $L/D = 5$ then decreases about 3 dB at $L/D = 7$. Mode 3 amplitude increases until it is nearly equal to the mode 2 SPL. The prediction equations must take these variations into account. Also included in Figure 52 are data points from Reference 8 for modes 2 and 3 at L/D ratios of 4 and 6. Although the agreement in levels is not particularly good, the basic trends are the same. The agreement in trends is quite good.

Data from Microphone C for the $L/D = 5$ configuration for various Mach numbers from all three test altitudes are presented in Figures 53 - 55 and the same data for the $L/D = 7$ configuration are presented in Figures 56 - 58. The data indicate that the amplitude of the mode frequencies, relative to the broadband level, increases with Mach number. Also it can be noted that the mode frequencies increase with Mach number. The Mach number effects on each mode frequency are summarized in Figures 59 - 60. The $L/D = 5$ results, Figure 59, show modes 2 and 3 having nearly equal amplitudes up to about Mach 0.9 and then mode 3 drops to about 10 dB below mode 2 at Mach 1.3. Mode 1 is consistently the lowest of the three modes. Figure 60 indicates that for $L/D = 7$ the amplitudes of the resonant modes do not vary more than 5 dB at any Mach number.

The prediction equations developed in Reference 1 were modified to account for changes in the L/D ratio based upon the above data. The modified equations for the amplitudes of the first three mode frequencies are as follows:

$$20 \log \left(\frac{P_2 \text{ max}}{q} \right) = \begin{cases} -8 + 20 \log (-M^2 + 2M - 0.7) & L/D = 5 \\ -14 + 20 \log (-M^2 + 2M - 0.7) & L/D = 7 \end{cases} \quad (2)$$

$$20 \log \left(\frac{P_1 \text{ max}}{q} \right) = \begin{cases} 20 \log \left(\frac{P_2 \text{ max}}{q} \right) - 6 & L/D = 5 \\ 20 \log \left(\frac{P_2 \text{ max}}{q} \right) - 2 & L/D = 7 \end{cases} \quad (3)$$

$$20 \log \left(\frac{P_3 \text{ max}}{q} \right) = 20 \log \left(\frac{P_2 \text{ max}}{q} \right) \quad L/D = 5, 7 \quad (4)$$

where $P_1 \text{ max}$, $P_2 \text{ max}$ and $P_3 \text{ max}$ are the one-third octave band sound pressure levels at the rear of the cavity for the first three resonant modes respectively.

The equations used to predict the longitudinal distribution of the amplitude for each mode were also modified to reflect L/D variations. The resulting mode shape equations are as follows:

$$20 \log \left(\frac{P_n}{q} \right)_{X/L} = \begin{cases} 20 \log \left(\frac{P_n \text{ max}}{q} \right) - 10 [2 - X/L - |\cos \alpha_n X/L|] & L/D = 5 \\ 20 \log \left(\frac{P_n \text{ max}}{q} \right) - 10 [2.7 - 1.7 X/L - |\cos \alpha_n X/L|] & L/D = 7 \end{cases} \quad (5)$$

$n = 1, 2, 3$

$$\alpha_1 = 3.5$$

$$\alpha_2 = 6.3$$

$$\alpha_3 = 10.0$$

where $20 \log \left(\frac{P}{q} \right)_{X/L}$ are one-third octave band sound pressure levels for the mode frequencies at nondimensional locations in the cavity and $20 \log \left(\frac{P}{q} \right)_{\text{max}}$ are the one-third octave band sound pressure levels for the mode frequencies at the rear of the cavity. These equations are plotted in Figure 61 for a L/D ratio of 5 and in Figure 62 for a L/D ratio of 7. The measured data for an altitude of 3000 feet and Mach number of 0.82 are also presented in both figures. The agreement is seen to be quite good for both configurations with the maximum error being about 4 dB. With the equations presented thus far it is possible to predict the one-third octave band levels of each of the first three resonant frequencies as a function of Mach number, cavity longitudinal position and L/D ratio. However, to predict the complete one-third octave band spectrum the broadband levels are needed.

Broadband Levels

It was shown in Reference 1, for L/D = 4, that the broadband levels increase towards the rear of the cavity. The magnitude of the increase was 10 dB and was assumed linear for prediction purposes. The flight data for the L/D ratios of 5 and 7 show that this increase is larger for shallower cavities as was also noted in Reference 3. Figure 63 presents the one-third octave band spectra at locations along the cavity for an altitude of 30,000 ft and Mach number of 0.82 for the L/D = 5 configuration. The same data for the L/D = 7 configuration are presented in Figure 64. Both figures clearly indicate the increase of the broadband levels toward the rear of the cavity. Figure 63, for L/D = 5, indicates an increase of about 13 dB while Figure 64, for L/D = 7, shows an increase of about 17 dB. For prediction purposes these increases were assumed linear along the cavity.

The difference between the resonant peaks and the maximum broadband levels were observed to decrease with increasing L/D ratio. This trend is easily noted in Figure 65 for data from the rear of the cavity. There is a 15 dB difference for L/D = 4, around 11 dB for L/D = 5, and near 5 dB for L/D = 7.

The shape of the broadband spectrum is essentially the same for all three L/D ratios. Broadband data from other cavity locations collapsed nearly as well as that at the rear of the cavity. Since the shape of the broadband essentially does not vary with L/D ratio a similar prediction curve as developed in Reference 1 for L/D = 4 was utilized for the other L/D ratios. The higher frequency end of the curve was adjusted to obtain better agreement with the data. Also, the prediction equations were modified to account for variations in levels at longitudinal positions and to account for the difference between the resonant peaks and the maximum broadband levels as was noted above.

The resulting equations to predict the maximum broadband levels are:

$$20 \log \left(\frac{P_b \text{ max}}{q} \right) = \begin{cases} 20 \log \left(\frac{P_2 \text{ max}}{q} \right) - 11 - 12 (1-X/L) & \text{L/D} = 5 \\ 20 \log \left(\frac{P_2 \text{ max}}{q} \right) - 5 - 18 (1-X/L) & \text{L/D} = 7 \end{cases} \quad (6)$$

where P_b is the rms pressure in the peak one-third octave band of the broadband spectrum. Figure 66 presents the resulting curve for predicting the broadband levels in a cavity for various L/D ratios.

Effect of Store Insertion

In order to determine the effect a store has on the fluctuating pressure environment in the cavity an ogive store was mounted in the L/D = 7 configuration as shown in Figures 5 and 6. This configuration was tested for the same flight conditions as the empty cavities and the same data were obtained. Figures 67 - 75 present data from Microphones A through I for each test altitude at Mach 0.82. Figures 76 - 78 present data from Microphone C for various Mach numbers. The figures reveal variations from the empty cavity data. Figures 79 - 86 illustrate these differences by comparing the spectra from the empty and the store containing cavities for several test conditions. A major effect of store insertion is seen to be a reduction in the amplitude of the low frequencies.

The reduction in low frequencies is seen to increase with altitude for the same Mach number. The effect of the store on the resonant peaks is difficult to distinguish at the Mach numbers which were flight tested. These effects become more apparent at higher Mach numbers (i.e., see Figure 85) and generally result in a decrease of 3 - 4 dB in the first three resonant peaks.

It was concluded in Reference 3 that the location of the store, with regards to store-shear layer interaction, was the determining factor as to the magnitude of reduction that would be realized. If the store does not interact with the shear layer, little reduction will occur. Also, it was observed that if the store is not wide enough to effectively fill the cavity mouth area the undisturbed portion of the shear layer is still capable of exciting cavity resonances. The wind tunnel data of Reference 3 showed that one store (2 inches wide in a 7 inch wide cavity opening) at Mach 0.8 resulted in only a 3 dB reduction in the peak fluctuating pressures while a two store configuration resulted in approximately 16 dB reduction. The flight tested store was 4 inches wide giving an area closure ratio between the referenced one and two configurations. In general, for the flight test Mach numbers the reduction in the level of the first three resonant frequencies was between those found in Reference 3. However, sufficient data are not available to generalize the effects of the store-in-cavity configuration. This can be clearly seen by careful examination of the data presented in Figure 46 of Reference 3, considering both Mach number and store effects.

Prediction Method for Fluctuating Pressures

The results presented above can be used to predict the characteristics of the fluctuating pressure which will occur in open rectangular cavities. The step by step procedure required to obtain the one-third octave band spectra at various locations in the cavity are given below:

Step 1 - Determine the first three resonant frequencies with the modified Rossiter equation from:

$$f_m = \frac{V}{L} \frac{\frac{m-0.25}{M}}{\left(1 + \frac{K-1}{2} M^2\right)^{1/2}} + 1.75 \quad m = 1, 2, 3, \quad (1)$$

Step 2 - Determine the maximum normalized one-third octave band amplitude for each frequency from:

$$20 \log \left(\frac{P_2 \text{ max}}{q} \right) = \begin{cases} -8 + 20 \log (-M^2 + 2M - 0.7) & L/D = 5 \\ -14 + 20 \log (-M^2 + 2M - 0.7) & L/D = 7 \end{cases} \quad (2)$$

$$20 \log \left(\frac{P_1 \text{ max}}{q} \right) = \begin{cases} 20 \log \left(\frac{P_2 \text{ max}}{q} \right) - 6 & L/D = 5 \\ 20 \log \left(\frac{P_2 \text{ max}}{q} \right) - 2 & L/D = 7 \end{cases} \quad (3)$$

$$20 \log \left(\frac{P_3 \text{ max}}{q} \right) = 20 \log \left(\frac{P_2 \text{ max}}{q} \right) \quad L/D = 5, 7 \quad (4)$$

Step 3 - Determine the longitudinal variation of the one-third octave band amplitude for each mode frequency from:

$$20 \log \left(\frac{P_n}{q} \right) = \begin{cases} 20 \log \left(\frac{P_n \text{ max}}{q} \right) - 10 [2 - X/L - |\cos \alpha_n X/L|] & L/D = 5 \\ 20 \log \left(\frac{P_n \text{ max}}{q} \right) - 10 [2.7 - 1.7 X/L |\cos \alpha_n X/L|] & L/D = 7 \end{cases} \quad (5)$$

$$n = 1, 2, 3$$

$$\alpha_1 = 3.5$$

$$\alpha_2 = 6.3$$

$$\alpha_3 = 10.0$$

Step 4 - Determine the peak normalized one-third octave band level of the broadband spectrum at the location in the cavity from:

$$20 \log \left(\frac{P_{b \text{ max}}}{q} \right) = \begin{cases} 20 \log \left(\frac{P_2 \text{ max}}{q} \right) -11 -12 (1-X/L) & L/D = 5 \\ 20 \log \left(\frac{P_2 \text{ max}}{q} \right) -5 -18 (1-X/L) & L/D = 7 \end{cases} \quad (6)$$

Step 5 - Determine the normalized broadband spectrum from Figure 66.

The prediction method given above is empirical and applies to rectangular cavities with L/D ratios in the range of 5 and 7 and for a Mach number range from 0.6 to 1.3.

Comparison of Predicted Results to Flight Data

Spectra resulting from the prediction equations were compared to the flight data for several test conditions. Figure 87 presents the measured and predicted spectra for the L/D = 5 configuration at Mach 0.82 and 3,000 ft altitude while Figure 88 presents the same data for L/D = 7. The agreement is seen to be quite good for all six cases presented. A comparison was also made for Mach numbers of 0.61 and 1.30 to determine how well the equations predicted the spectra at the Mach number extremes. The results of this comparison are shown in Figures 89 and 90. It is apparent that the prediction equations do quite well over the entire spectrum at the upper Mach number limit of 1.30 but tend to under-predict the broadband spectrum at the lower Mach number limit of 0.61.

Working Example

For clarity an example is presented illustrating the use of the prediction method and a comparison is made of results of this method to those obtained from Reference 3.

Consider the case of an aircraft flying at Mach 0.9 near sea level with an open nearly rectangular cavity 20 ft long and L/D ratio of either

5 or 7. It is desired to predict the aero-acoustic environment at the rear of the cavity for L/D = 5 and at the front, center and rear for L/D = 7. The solution is as follows:

From Step 1, Equation (1), the first 3 mode frequencies for both cases are determined to be:

$$f_1 = 15 \text{ Hz}$$

$$f_2 = 34 \text{ Hz}$$

$$f_3 = 54 \text{ Hz}$$

Equations (2), (3), and (4) of Step 2 are used to calculate the maximum normalized amplitude for each mode frequency and results in the following values:

for L/D = 5

$$20 \log (\frac{P_1}{q} \max) = -24$$

$$20 \log (\frac{P_2}{q} \max) = -18$$

$$20 \log (\frac{P_3}{q} \max) = -18$$

for L/D = 7

$$20 \log (\frac{P_1}{q} \max) = -27$$

$$20 \log (\frac{P_2}{q} \max) = -25$$

$$20 \log (\frac{P_3}{q} \max) = -25$$

The amplitude of each mode frequency at the desired longitudinal location is determined from Step 3, Equation (5). The results, referenced to $20 \mu\text{N/m}^2$, are:

for L/D = 5 at X/L = 1

$$SPL_1 = 165$$

$$SPL_2 = 171$$

$$SPL_3 = 171$$

for L/D = 7 at X/L = 1

$$SPL_1 = 162$$

$$SPL_2 = 164$$

$$SPL_3 = 164$$

at $X/L = 0.5$

$$SPL_1 = 145$$

$$SPL_2 = 155$$

$$SPL_3 = 148$$

at $X/L = 0.0$

$$SPL_1 = 145$$

$$SPL_2 = 147$$

$$SPL_3 = 147$$

The peak normalized one-third octave band levels of the broadband spectra for each location are determined from Step 4, Equation (6). These are:

for $L/D = 5$

$$20 \log \left(\frac{P_b}{q} \right)_{X/L = 0.5} = -29$$

for $L/D = 7$

$$20 \log \left(\frac{P_b}{q} \right)_{X/L = 1.0} = -30$$

$$20 \log \left(\frac{P_b}{q} \right)_{X/L = 0.5} = -39$$

$$20 \log \left(\frac{P_b}{q} \right)_{X/L = 0} = -48$$

The final step is to determine the broadband spectra from Figure 66.

The spectra obtained are shown in Figure 91 along with the spectrum that would result using the scheme offered in Reference 3. It is seen that the scheme from Reference 3 is conservative for all cases presented with conservatism being the greatest at the fore end of the cavity. It should be noted that the current prediction equations account for the relative variation of the resonant frequency amplitude and the longitudinal distribution of

the resonant frequency amplitudes as well as the broadband levels. The spectrum for the center of the cavity does not show modes 1 and 3; the reason for this is the longitudinal distribution of the resonant amplitudes. Figure 61 shows that modes 1 and 3 have nodes near the center of the cavity and thus the prediction scheme takes this into account, and results in the spectra given in Figure 91 for this particular location.

APPENDIX C
TABLE AND FIGURES

MACH NR	STATIC PRESSURE P_∞ (psia)	DYNAMIC PRESSURE q_∞ (psia)	$20 \log \left(\frac{P_{ref}}{q_\infty} \right)$ (dB)
0.61	4.37	1.12	172
	6.76	1.73	175
	13.17	3.37	181
0.71	4.37	1.56	174
	6.76	2.41	178
	13.17	4.69	184
0.82	4.37	2.06	177
	6.76	3.19	181
	13.17	6.21	186
0.93	4.37	2.66	179
	6.76	4.11	183
	13.17	8.01	189
1.05	4.37	3.35	181
	6.76	5.19	185
	13.17	10.11	191
1.17	4.37	4.18	183
	6.76	6.47	187
	13.17	12.60	193
1.30	4.37	5.17	185
	6.76	8.00	189
	13.17	15.58	194

TABLE 1 PRESSURE REFERENCE DATA

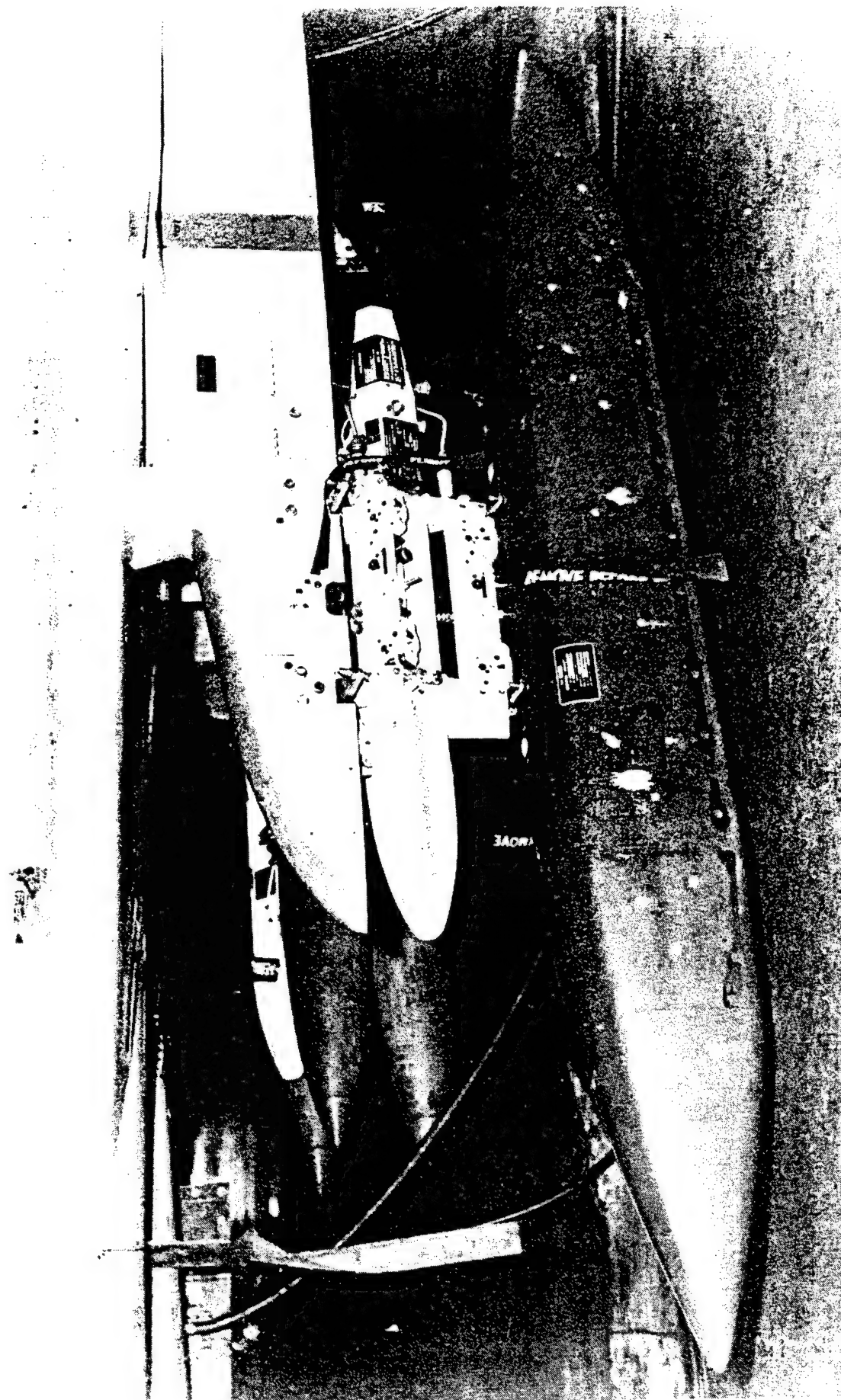
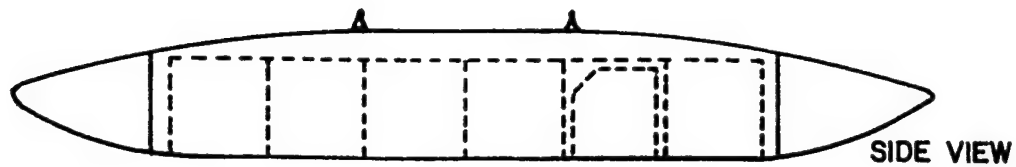
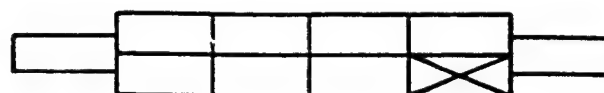


FIGURE 1 STANDARD SUU-41 MUNITIONS
DISPENSER POD

STANDARD MUNITIONS PACKAGE

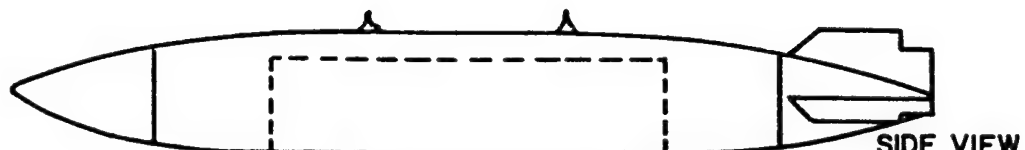


SIDE VIEW

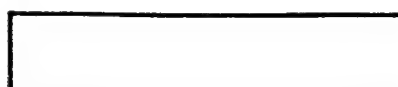


BOTTOM VIEW

STANDARD POD



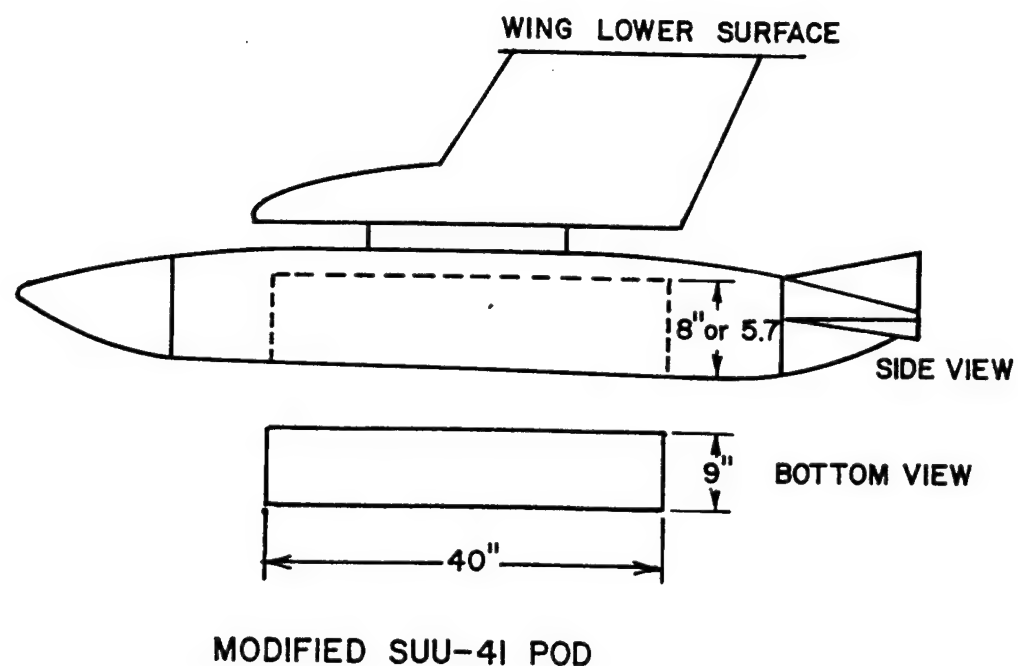
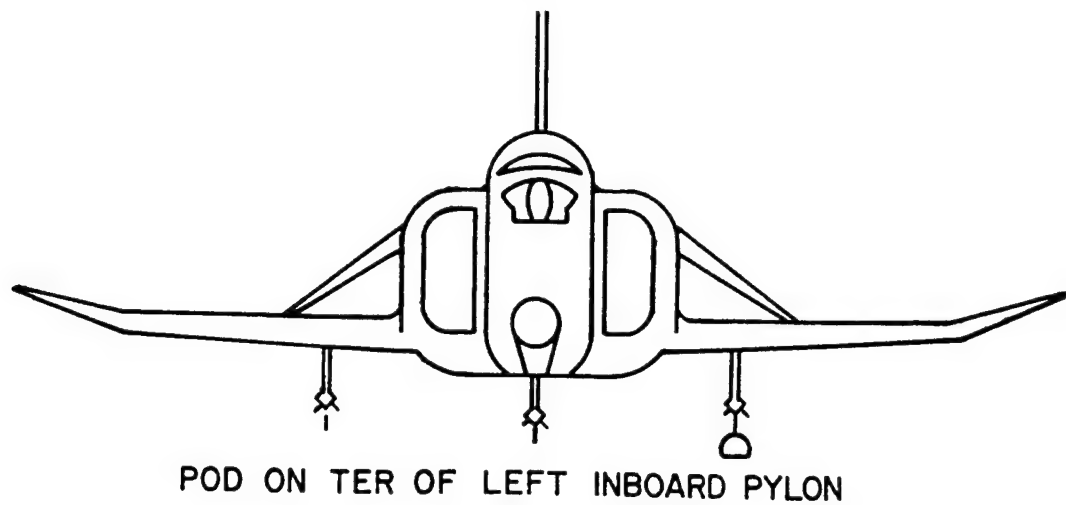
SIDE VIEW



BOTTOM VIEW

MODIFIED POD

FIGURE 2 STANDARD AND MODIFIED SUU-41 DISPENSER POD

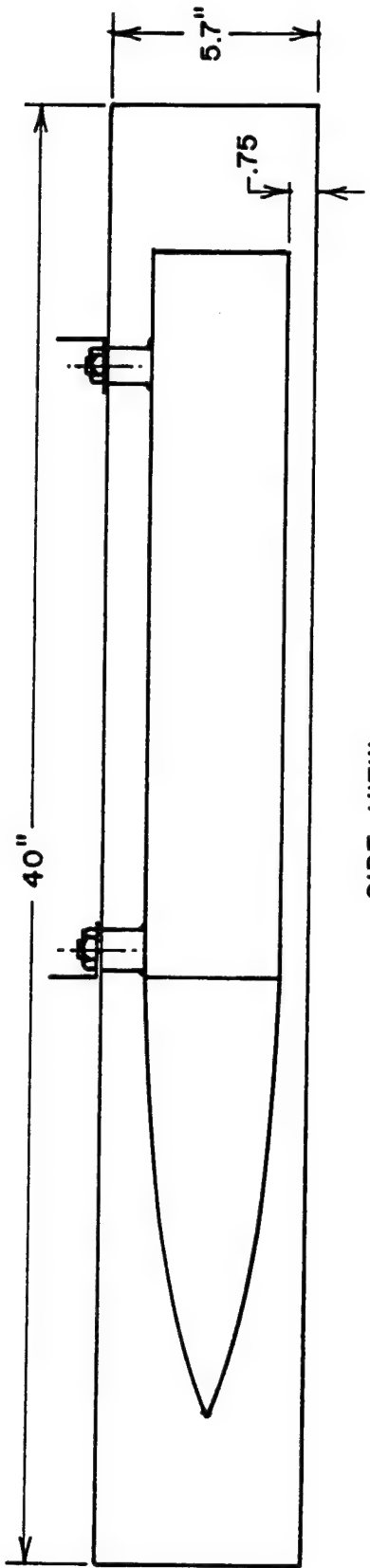


MODIFIED SUU-41 POD

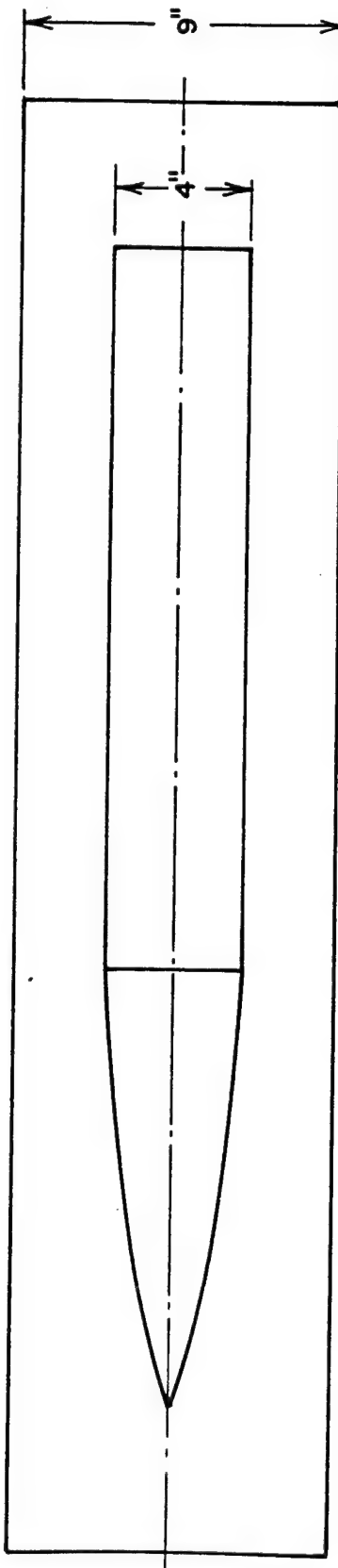
FIGURE 3 MODIFIED SUU-41 POD MOUNTED ON RF-4C AIRCRAFT



FIGURE 4 MODIFIED SUU-41 POD WITH
5.7 INCH DEEP CAVITY



SIDE VIEW



BOTTOM VIEW

FIGURE 5 STORE CONTAINING CAVITY CONFIGURATION

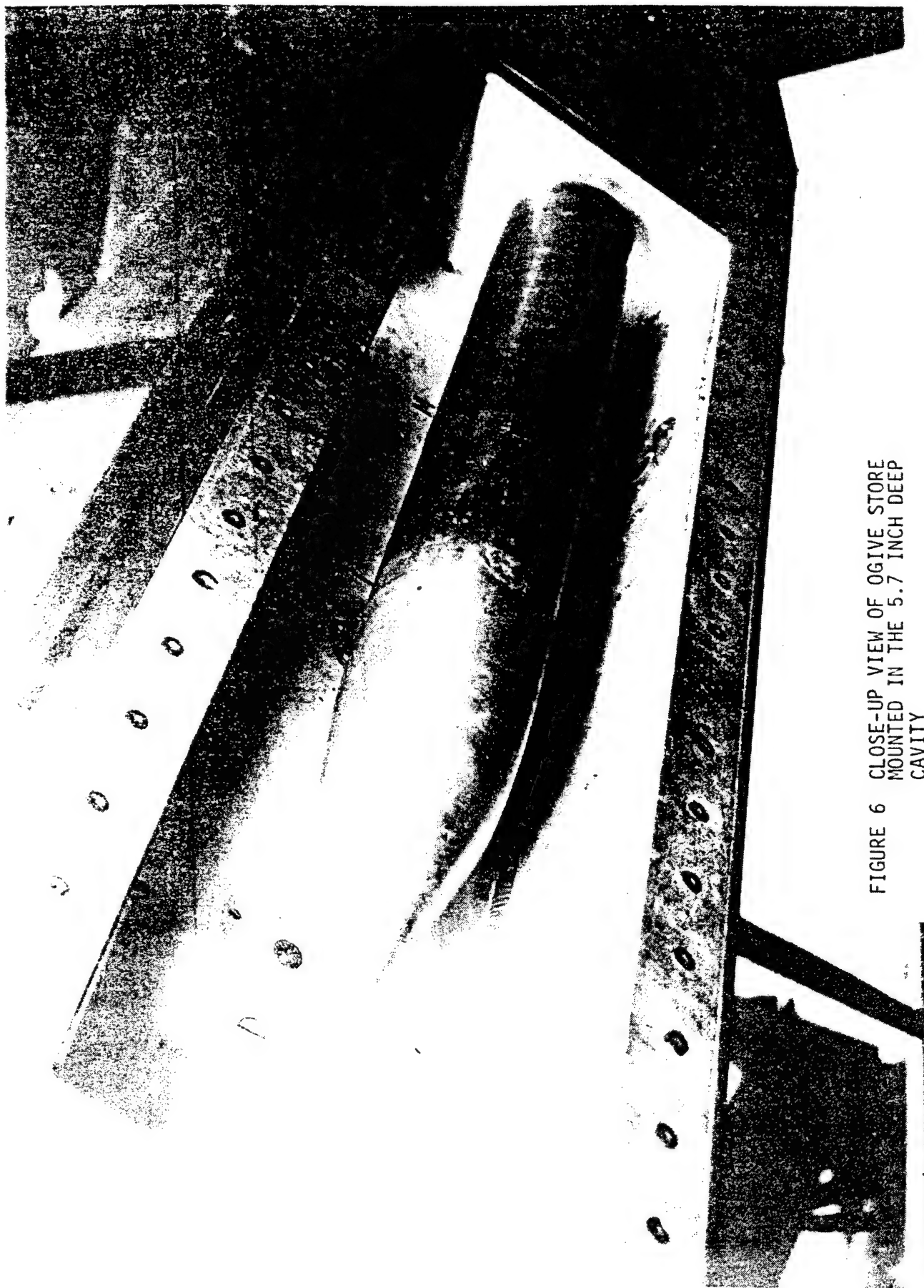
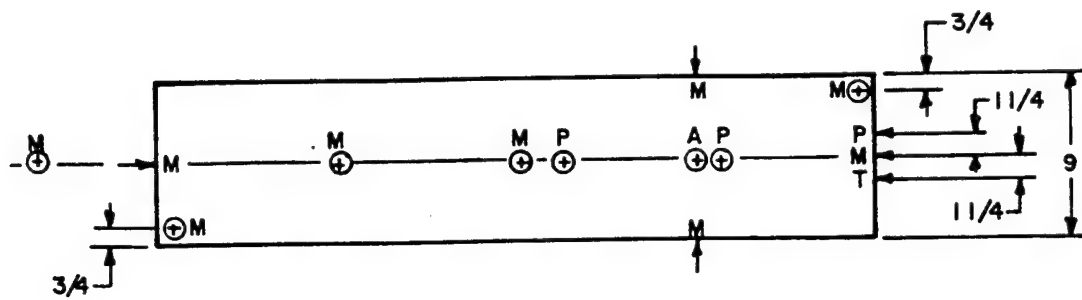


FIGURE 6 CLOSE-UP VIEW OF OGIVE STORE
MOUNTED IN THE 5.7 INCH DEEP
CAVITY



M - MICROPHONE
 T - THERMOCOUPLE
 A - ACCELEROMETER
 P - STATIC PRESSURE TAP

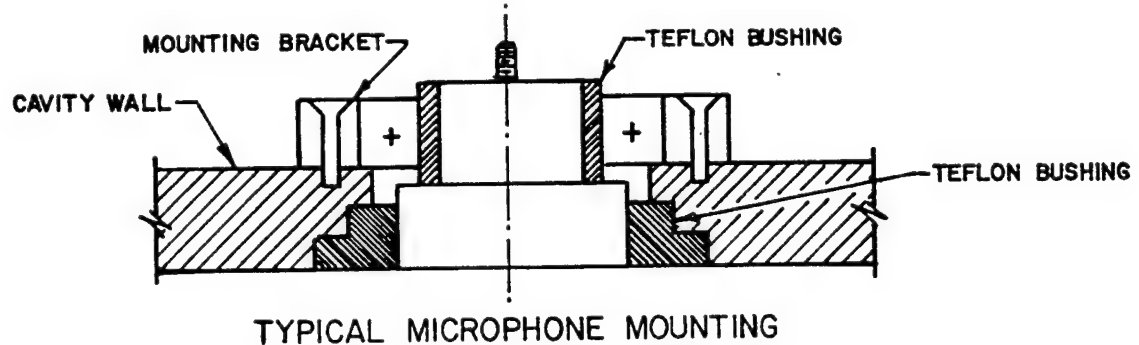
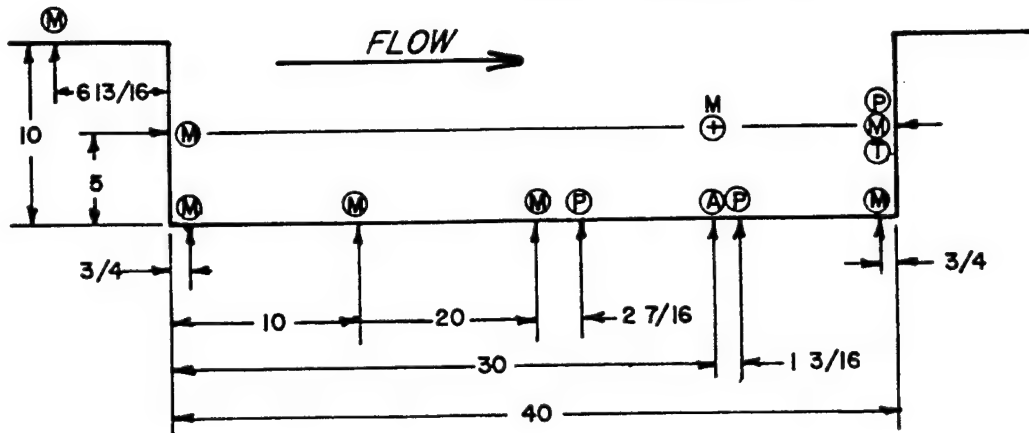


FIGURE 7 OPEN CAVITY INSTRUMENTATION LOCATION

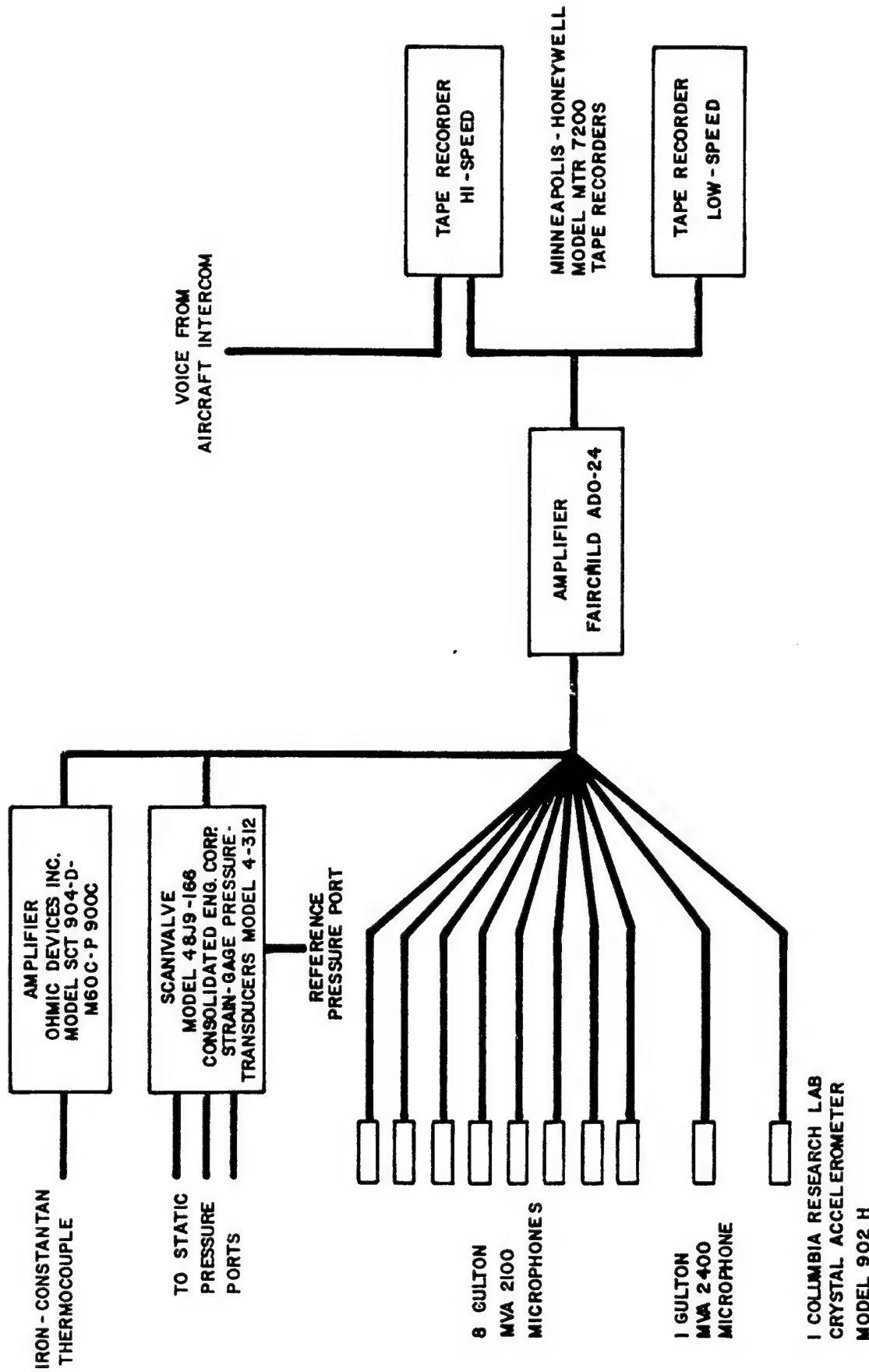


FIGURE 8 BLOCK DIAGRAM OF DATA ACQUISITION INSTRUMENTATION

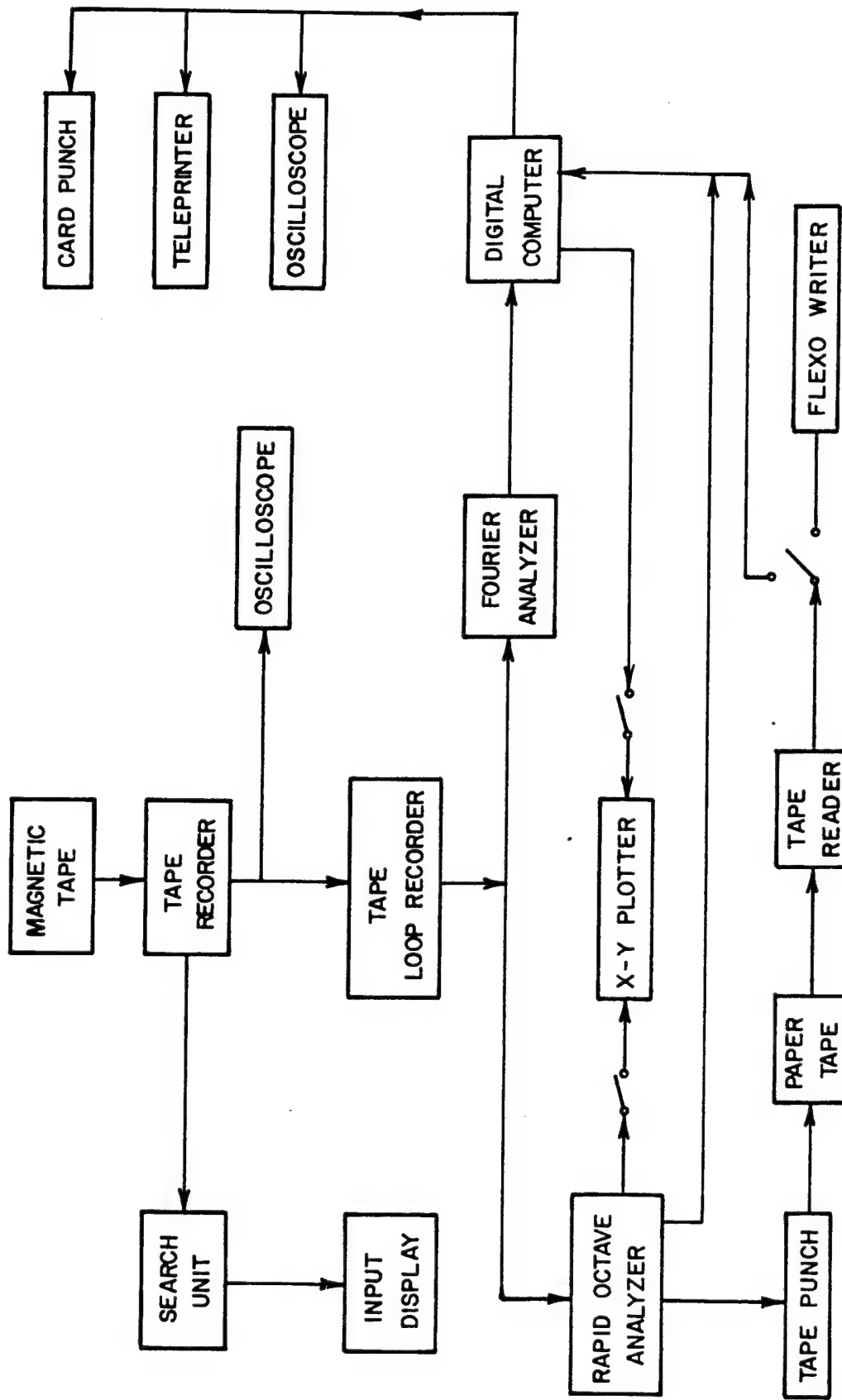


FIGURE 9 DATA REDUCTION SYSTEM

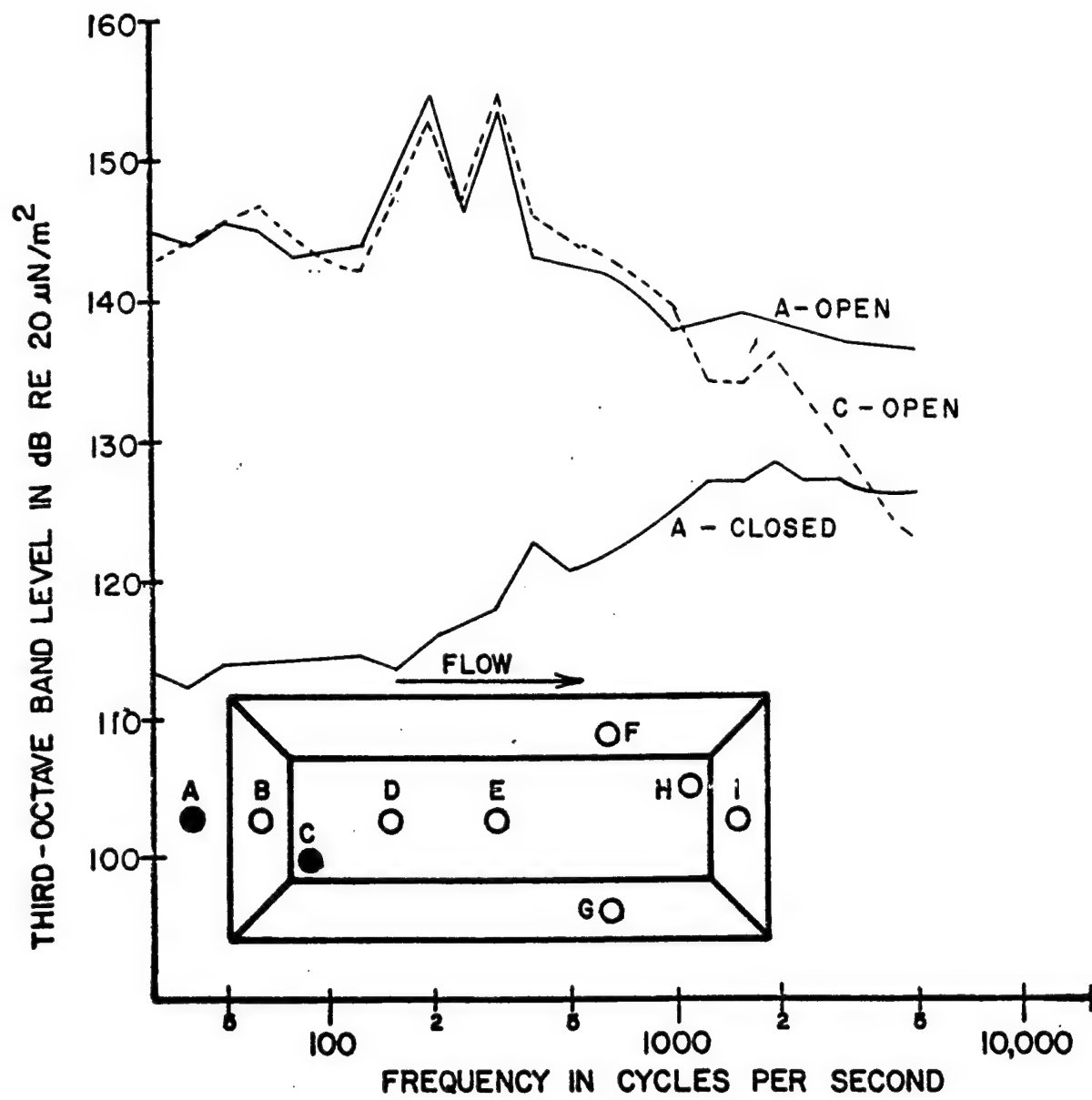


FIGURE 10 ONE-THIRD OCTAVE BAND SPECTRA FOR OPEN AND CLOSED
 $L/D = 5$ CONFIGURATION AT 3,000 FOOT ALTITUDE AND MACH 0.82

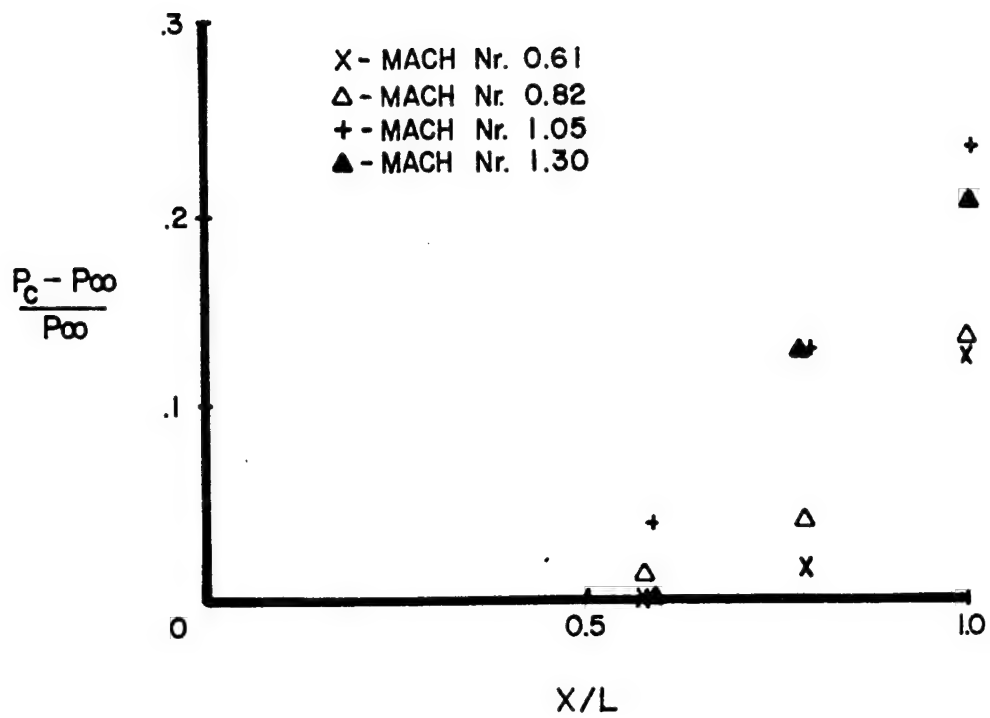


FIGURE 11 LONGITUDINAL VARIATION OF STATIC PRESSURE
FOR $L/D = 5$ AND $P_{\infty} = 6.76$ psia

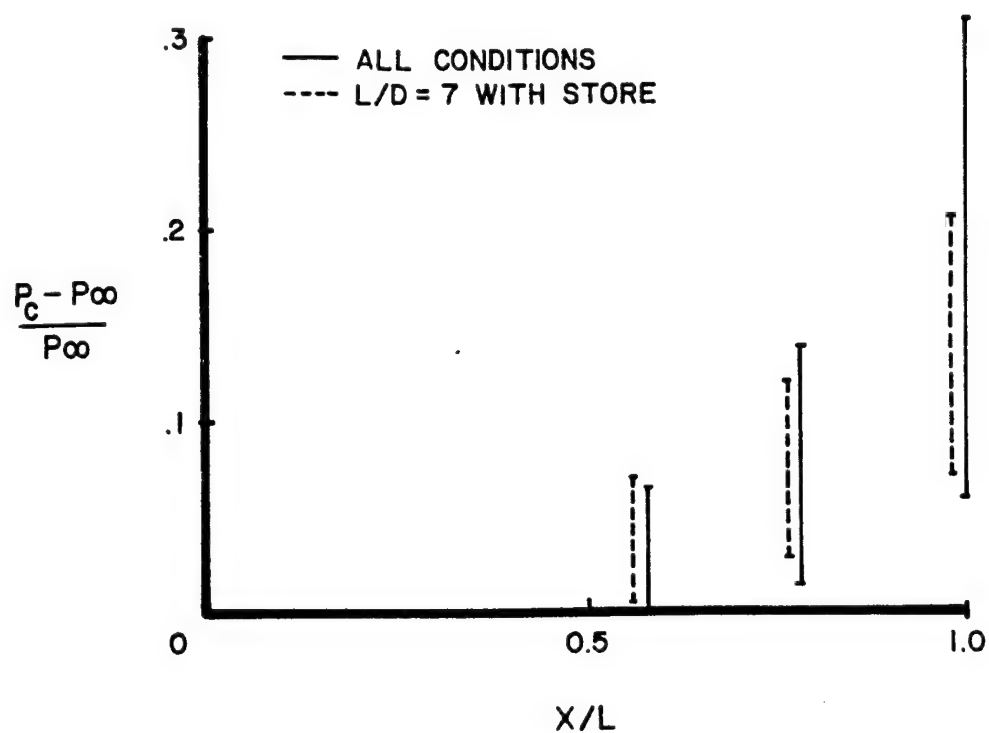
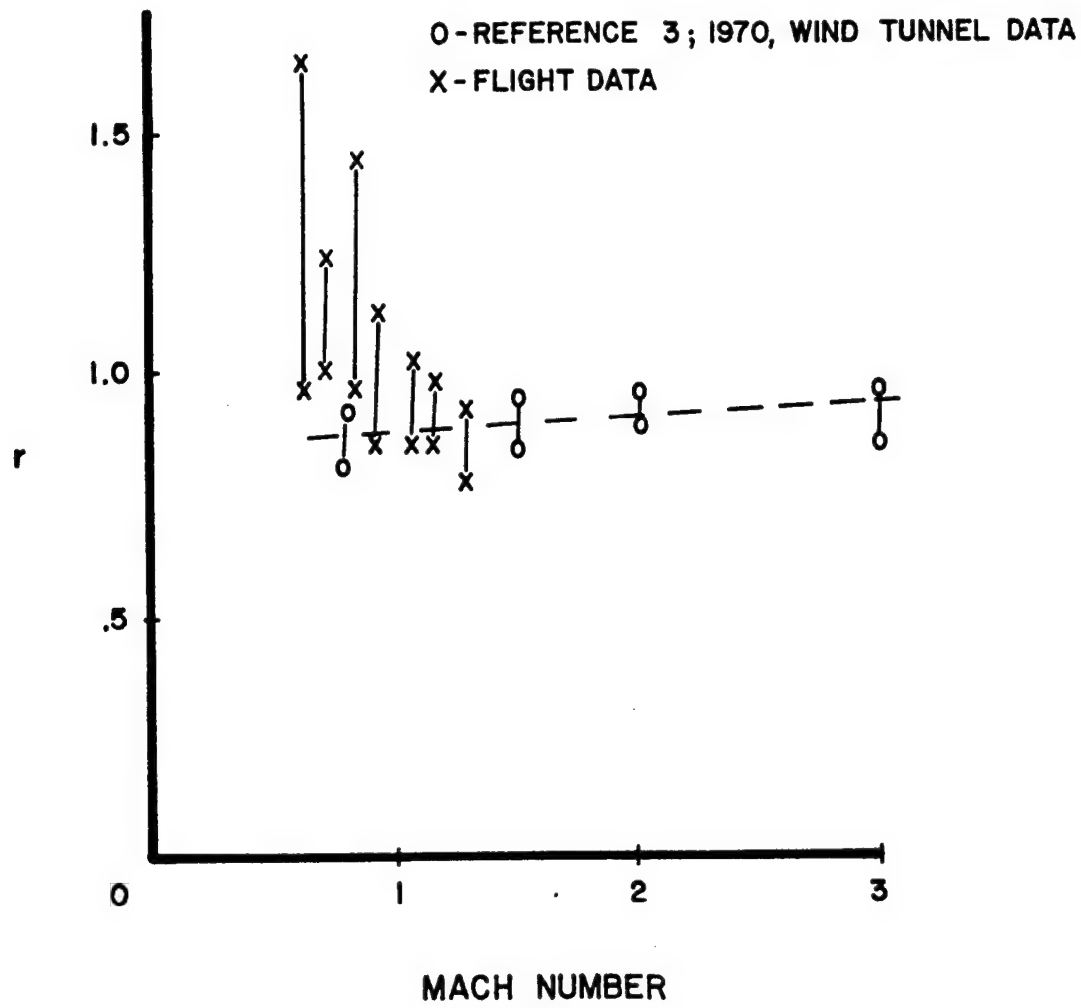


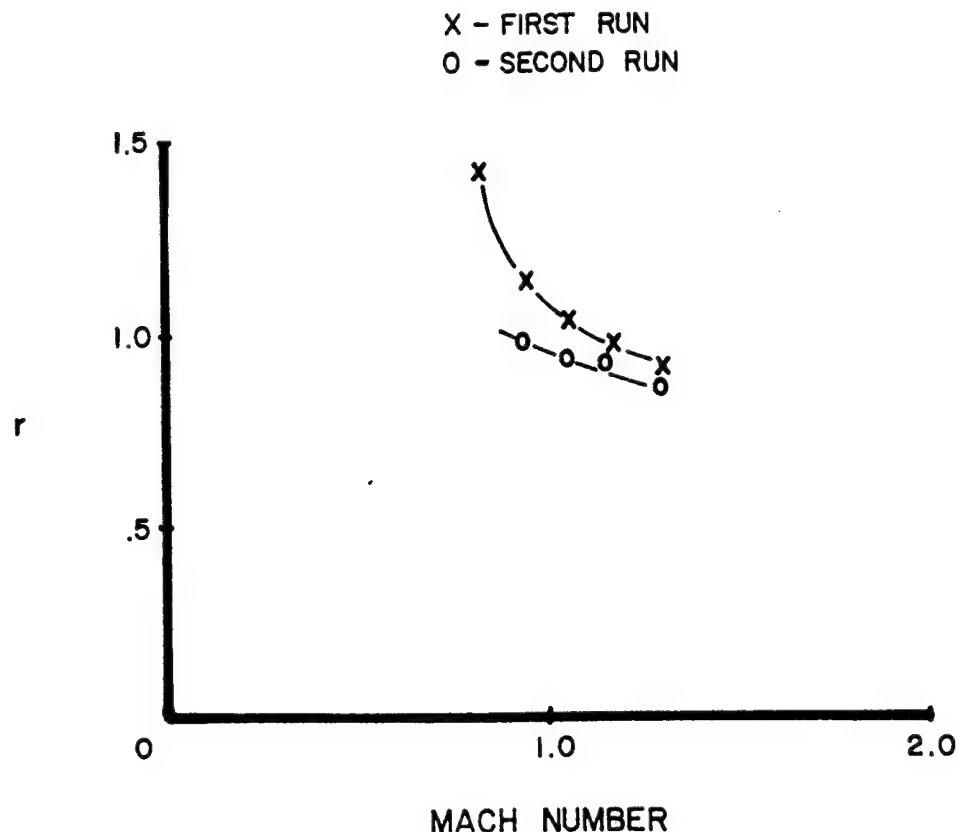
FIGURE 12 TOTAL SPREAD OF ALL THE NORMALIZED STATIC PRESSURE DATA



$$r = \frac{T_c - T_{\infty}}{T_0 - T_{\infty}}$$

T_c - CAVITY TEMPERATURE
 T_0 - FREE STREAM STAGNATION TEMPERATURE
 T_{∞} - FREE STREAM STATIC TEMPERATURE

FIGURE 13 COMPARISON OF CURRENT RECOVERY FACTORS FOR L/D = 7
 CAVITY WITH OGIVE STORE TO WIND TUNNEL RESULTS
 FROM REFERENCE 3



$$r = \frac{T_c - T_\infty}{T_0 - T_\infty}$$

T_c - CAVITY TEMPERATURE
 T_0 - FREE STREAM STAGNATION TEMPERATURE
 T_∞ - FREE STREAM STATIC TEMPERATURE

FIGURE 14 THERMAL RECOVERY FACTORS AS A FUNCTION OF MACH NUMBER FOR $L/D = 7$ WITH OGIVE STORE AT AN ALTITUDE OF 20,000 FEET

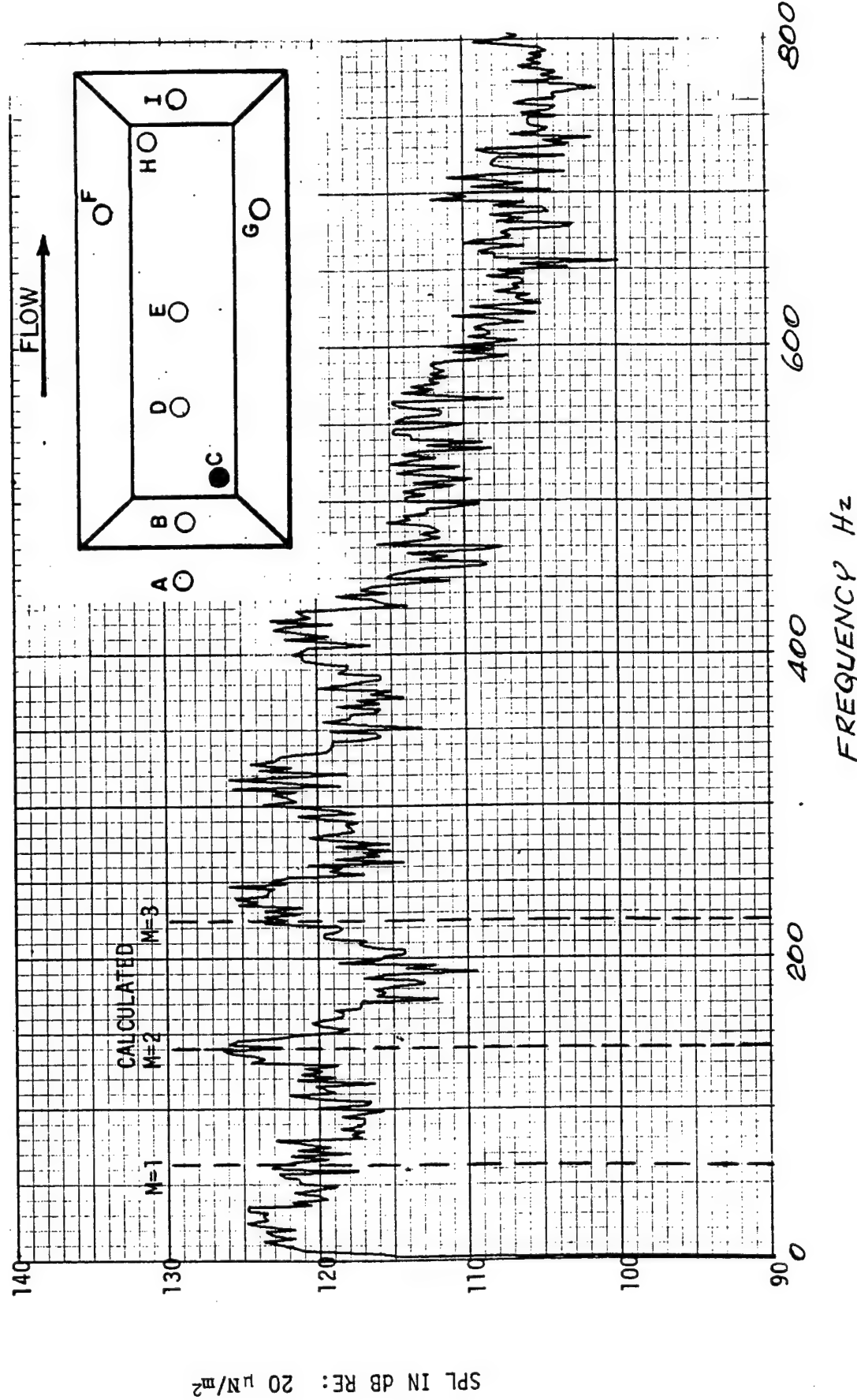


FIGURE 15 NARROWBAND (2 Hz) SPECTRUM FROM MICROPHONE C FOR AN ALTITUDE OF 20,000 FEET AT MACH 0.61 FOR L/D = 5

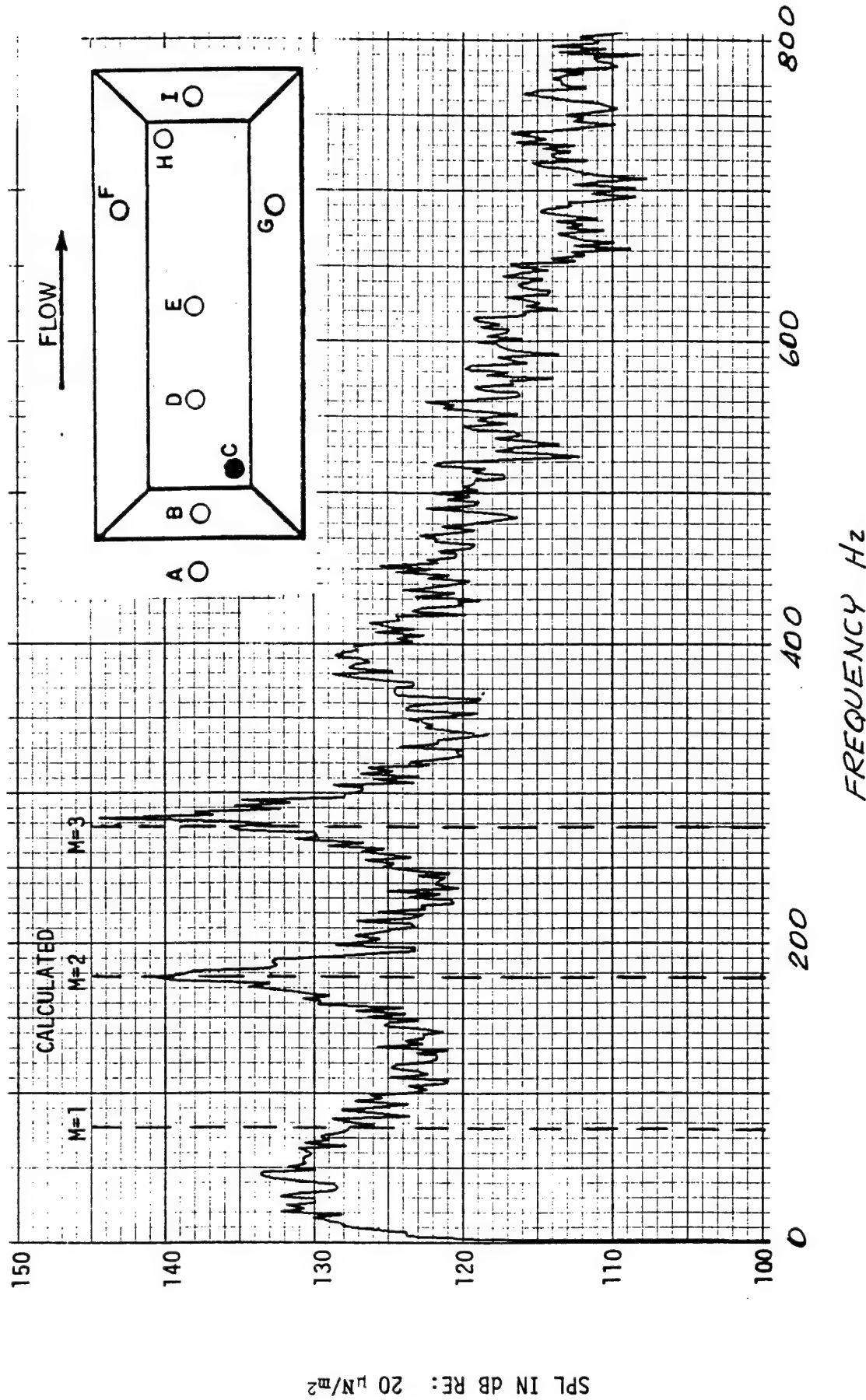


FIGURE 16 NARROWBAND (20 Hz) SPECTRUM FROM MICROPHONE C FOR AN ALTITUDE OF 20,000 FEET AT MACH 0.82 FOR L/D=5

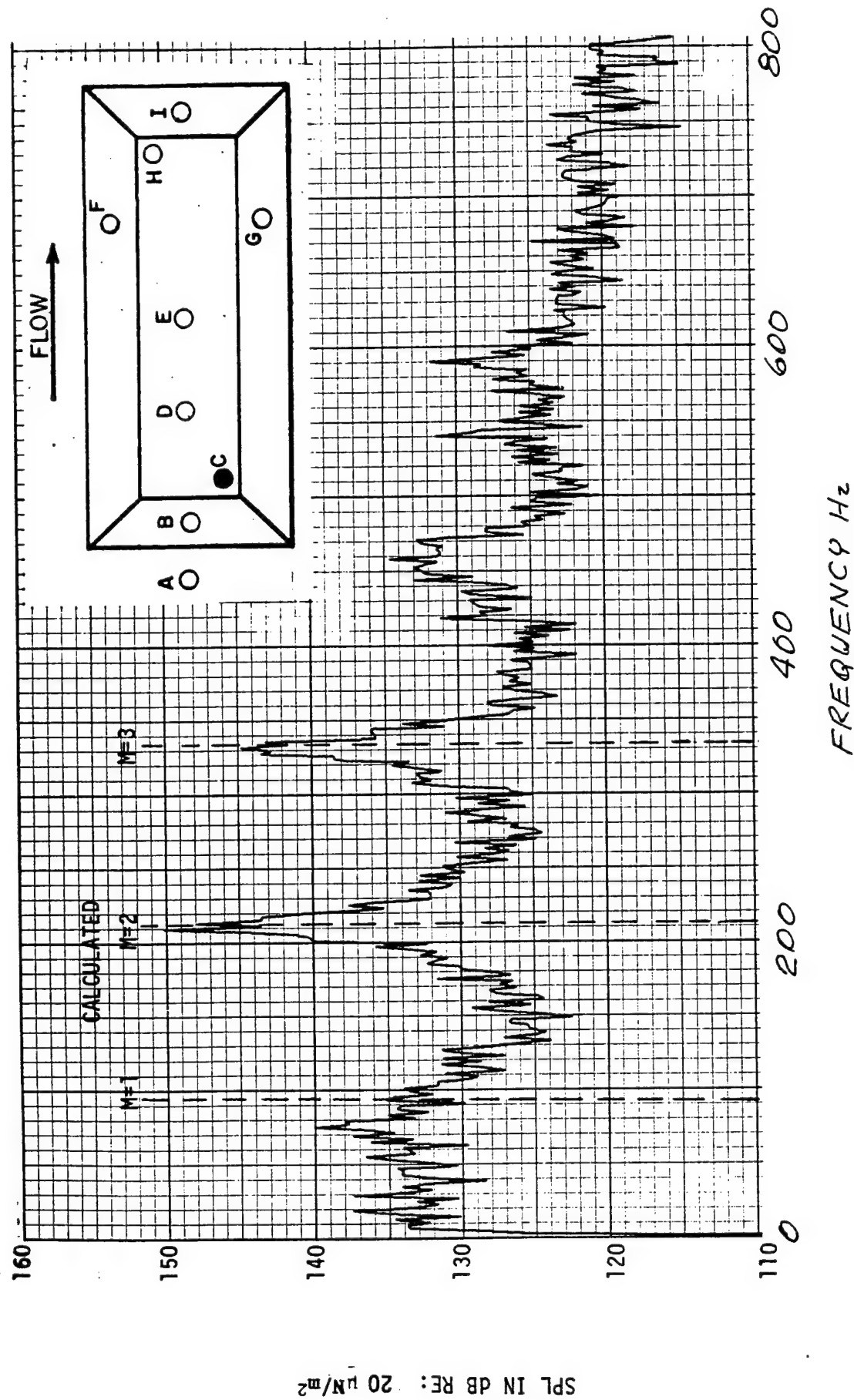


FIGURE 17 NARROWBAND (2 Hz) SPECTRUM FROM MICROPHONE C FOR AN ALTITUDE OF 20,000 FEET AT MACH 1.05 FOR $L/D = 5$

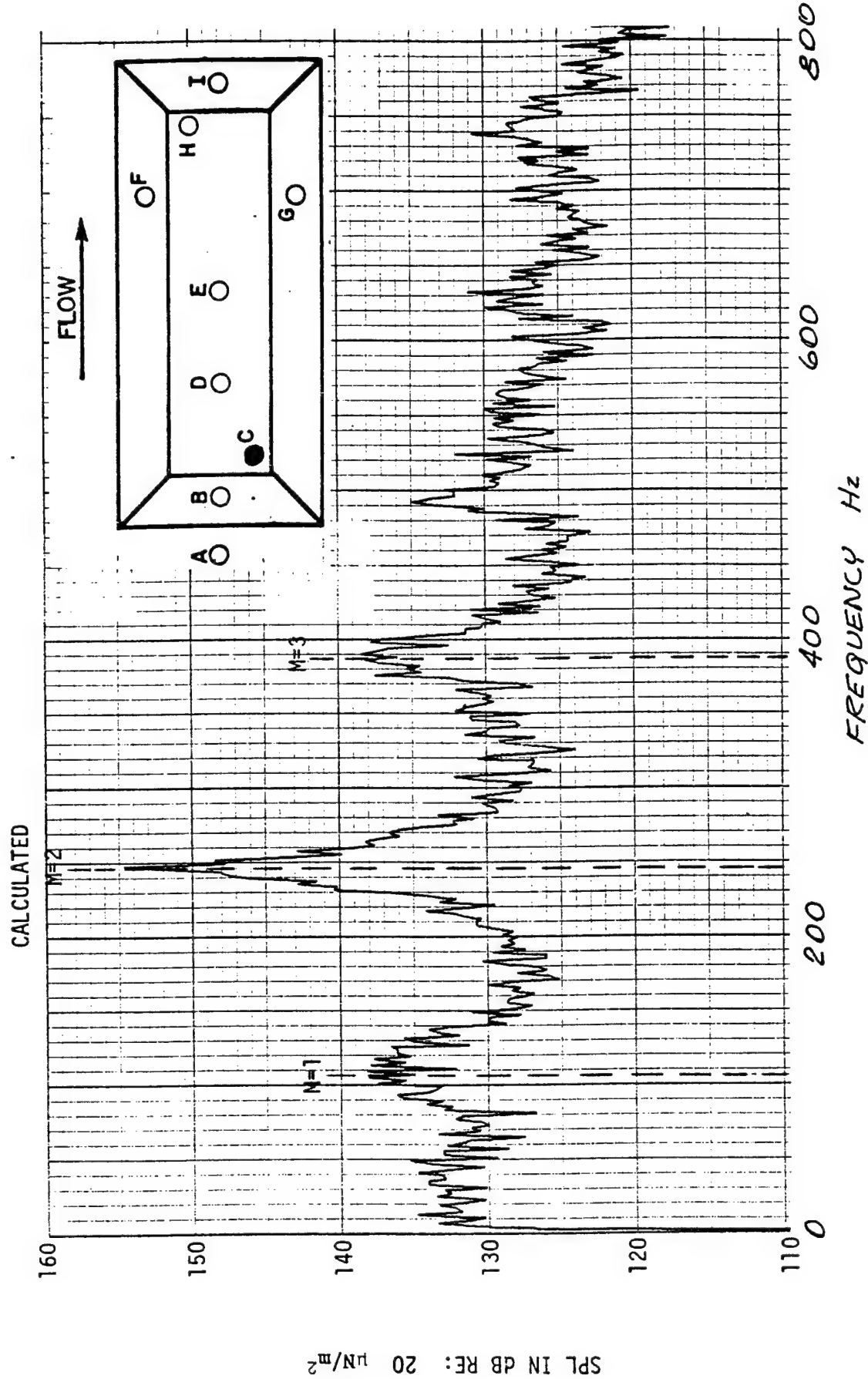


FIGURE 18 NARROWBAND (2 Hz) SPECTRUM FROM MICROPHONE C FOR AN ALTITUDE OF 20,000 FEET AT MACH 1.30 FOR $L/D = 5$

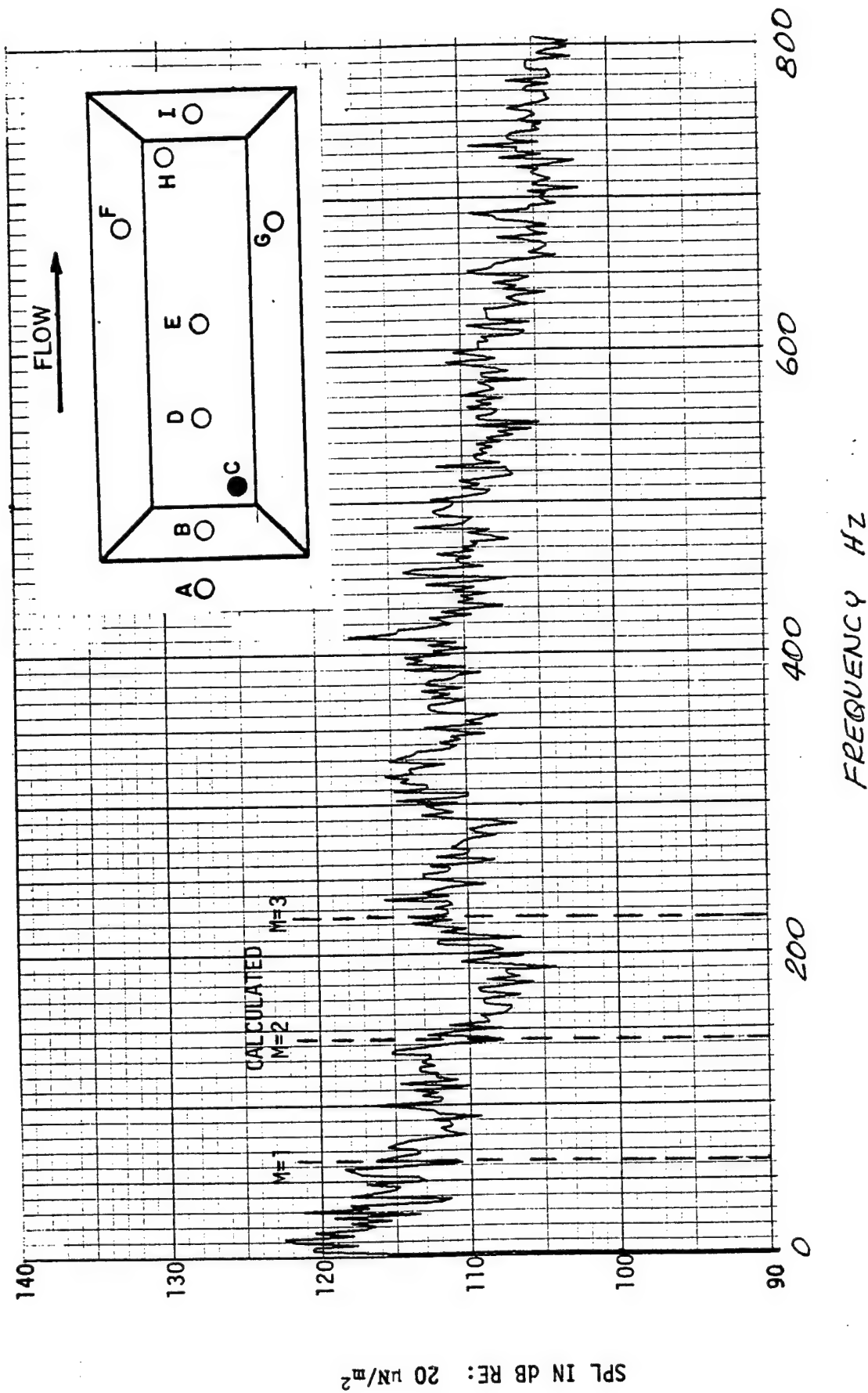


FIGURE 19 NARROWBAND (2 Hz) SPECTRUM FROM MICROPHONE C FOR AN ALTITUDE 20,000 AT MACH 0.61 FOR $L/D = 7$

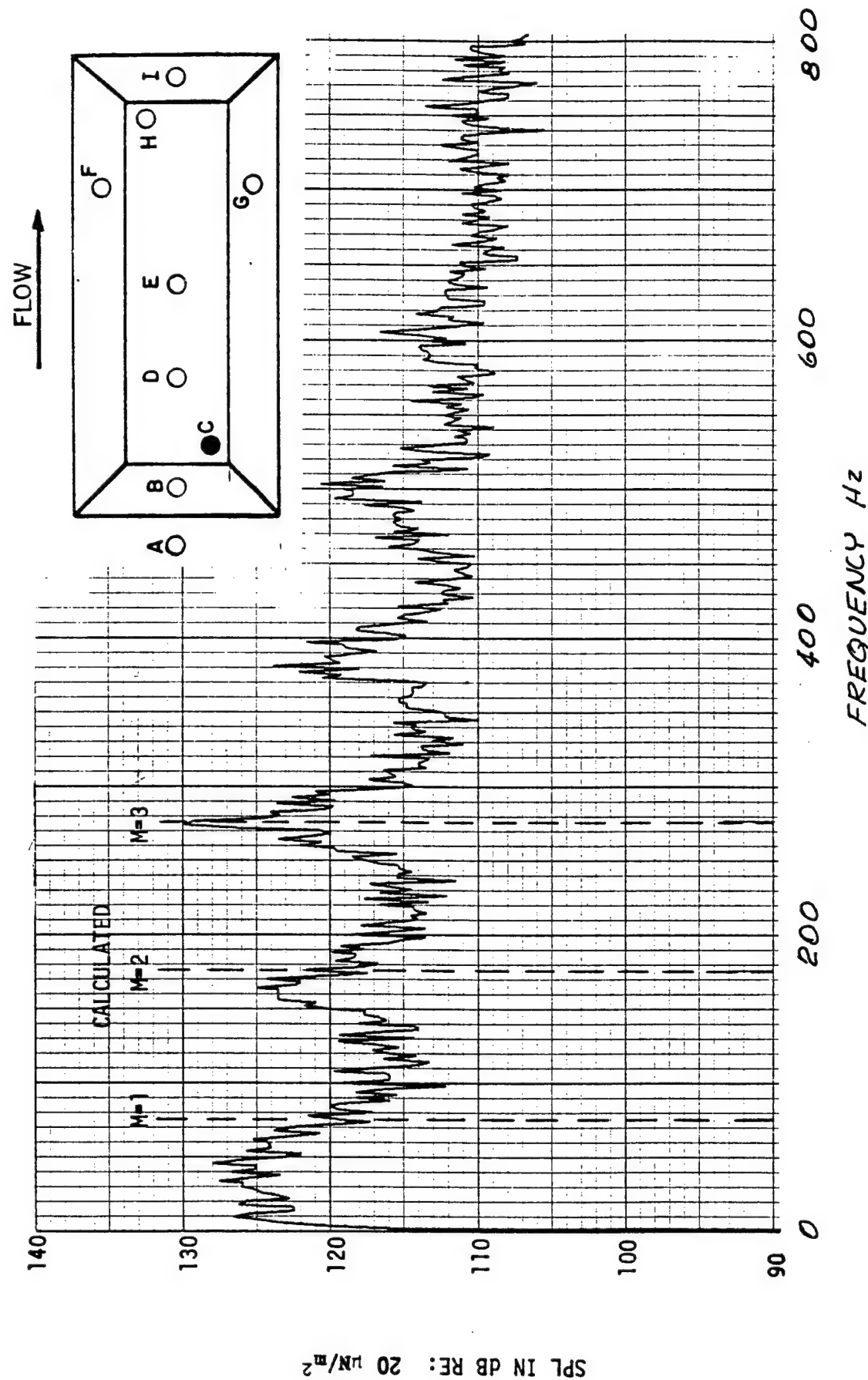


FIGURE 20 NARROWBAND (2 Hz) SPECTRUM FROM MICROPHONE C FOR AN ALTITUDE OF 20,000 FEET AT MACH 0.82 FOR L/D = 7

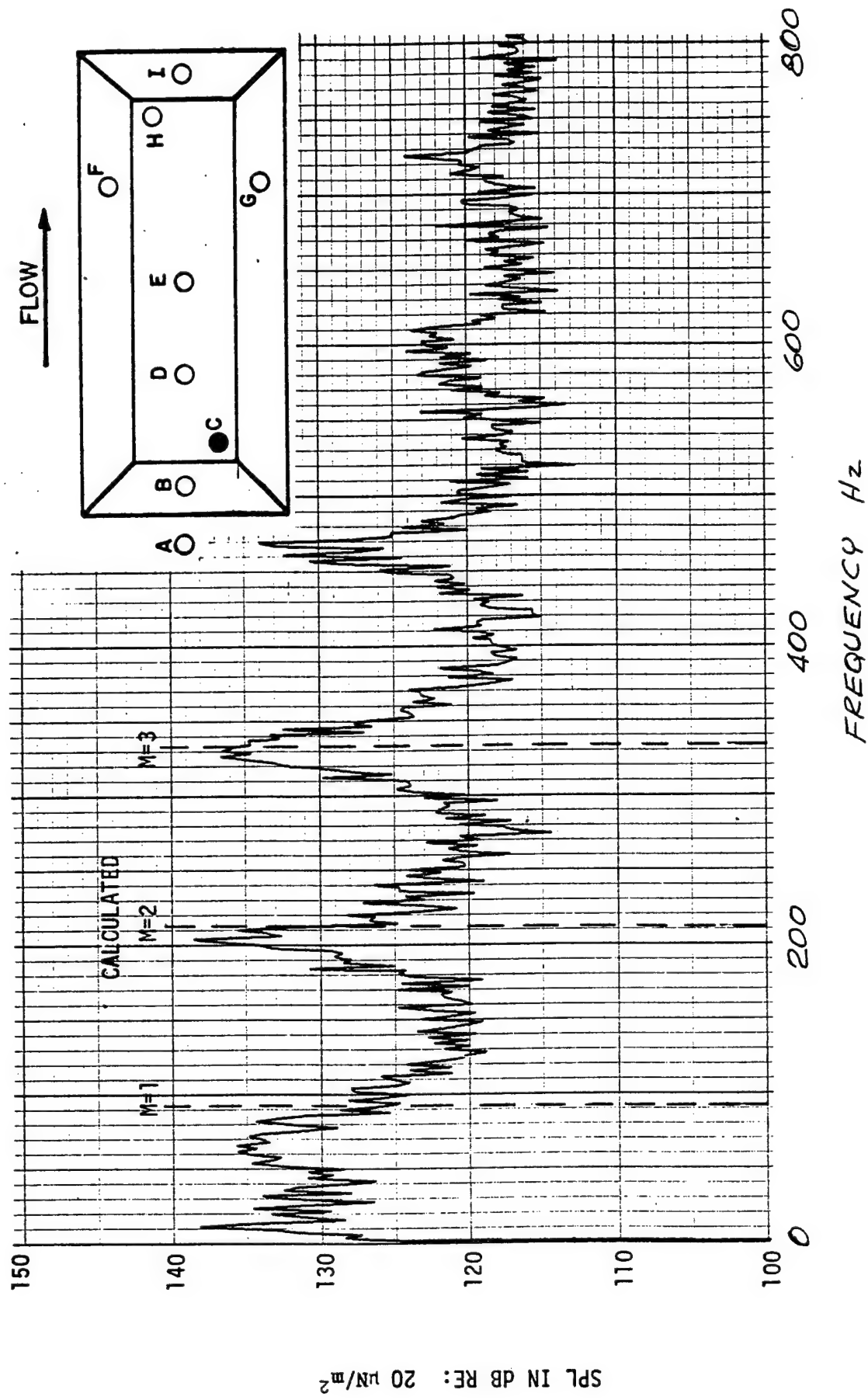


FIGURE 21 NARROWBAND (2 Hz) SPECTRUM FROM MICROPHONE C FOR AN ALTITUDE OF 20,000 FEET AT MACH 1.05 FOR L/D = 7

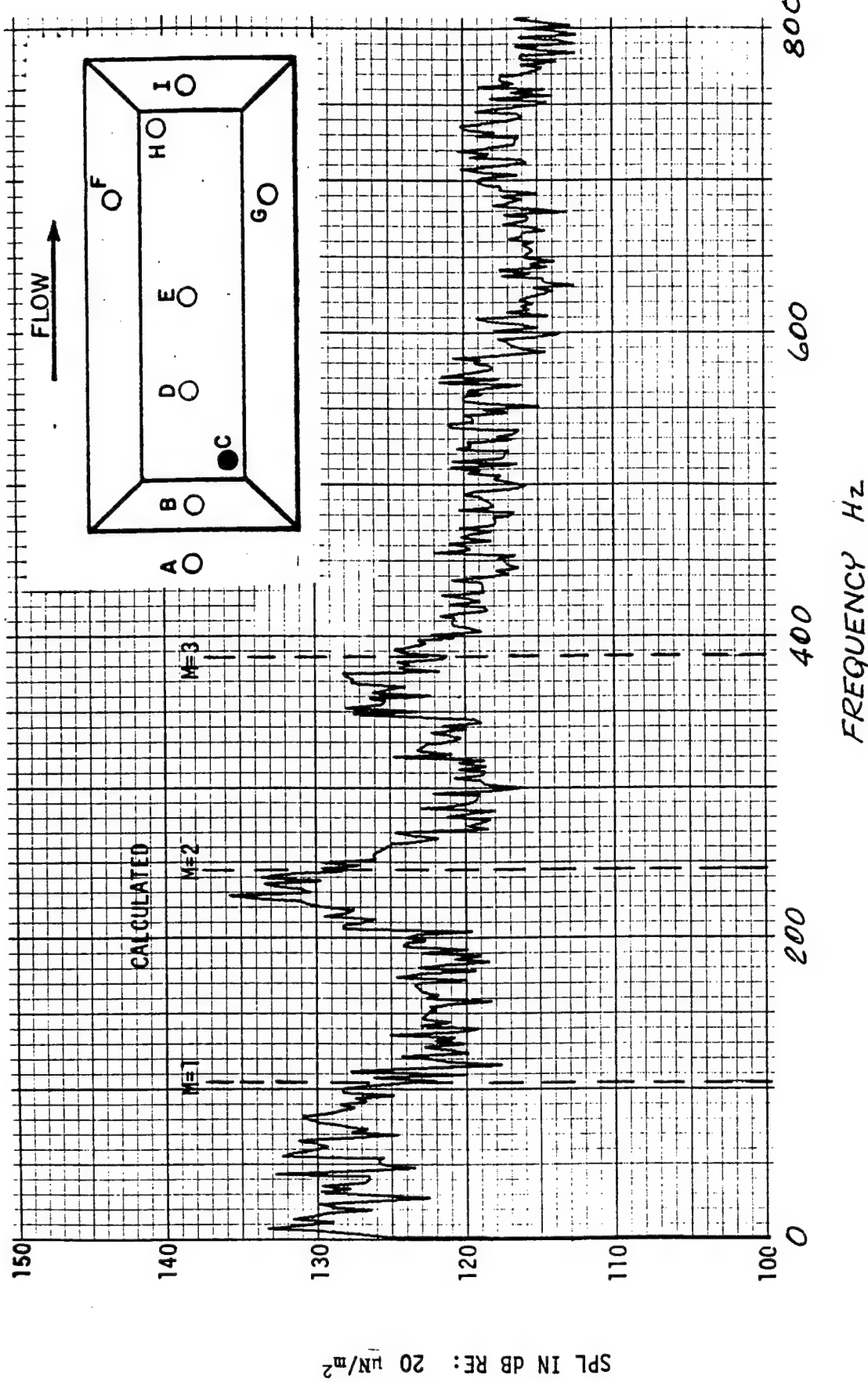


FIGURE 22 NARROWBAND (2 Hz) SPECTRUM FROM MICROPHONE C FOR AN ALTITUDE OF 20,000 FEET AT MACH 1.30 FOR L/D = 7

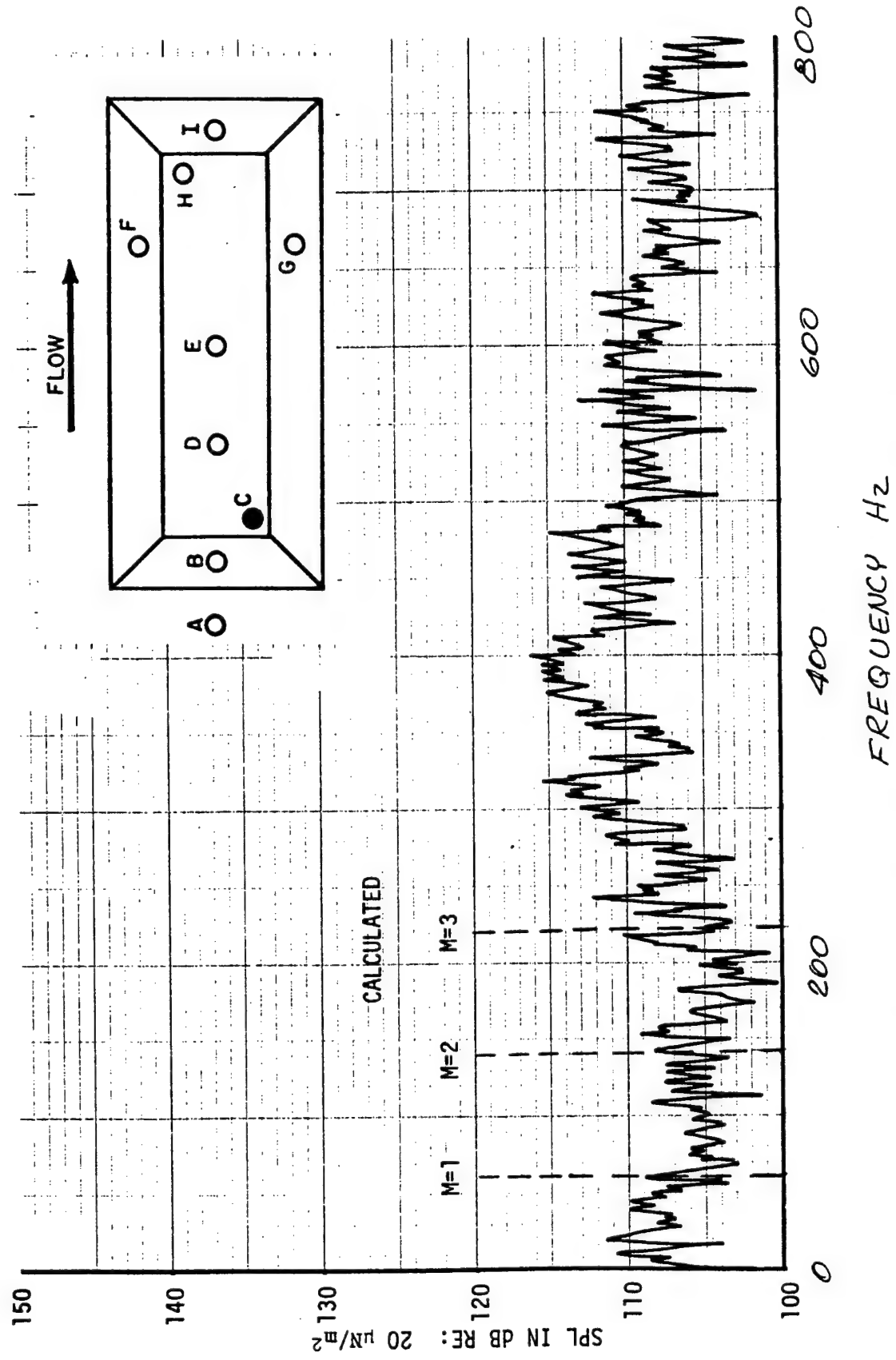


FIGURE 23 NARROWBAND (2 Hz) SPECTRUM FROM MICROPHONE C FOR AN ALTITUDE OF 20,000 FEET AT MACH 0.61 FOR L/D = 7 WITH STORE

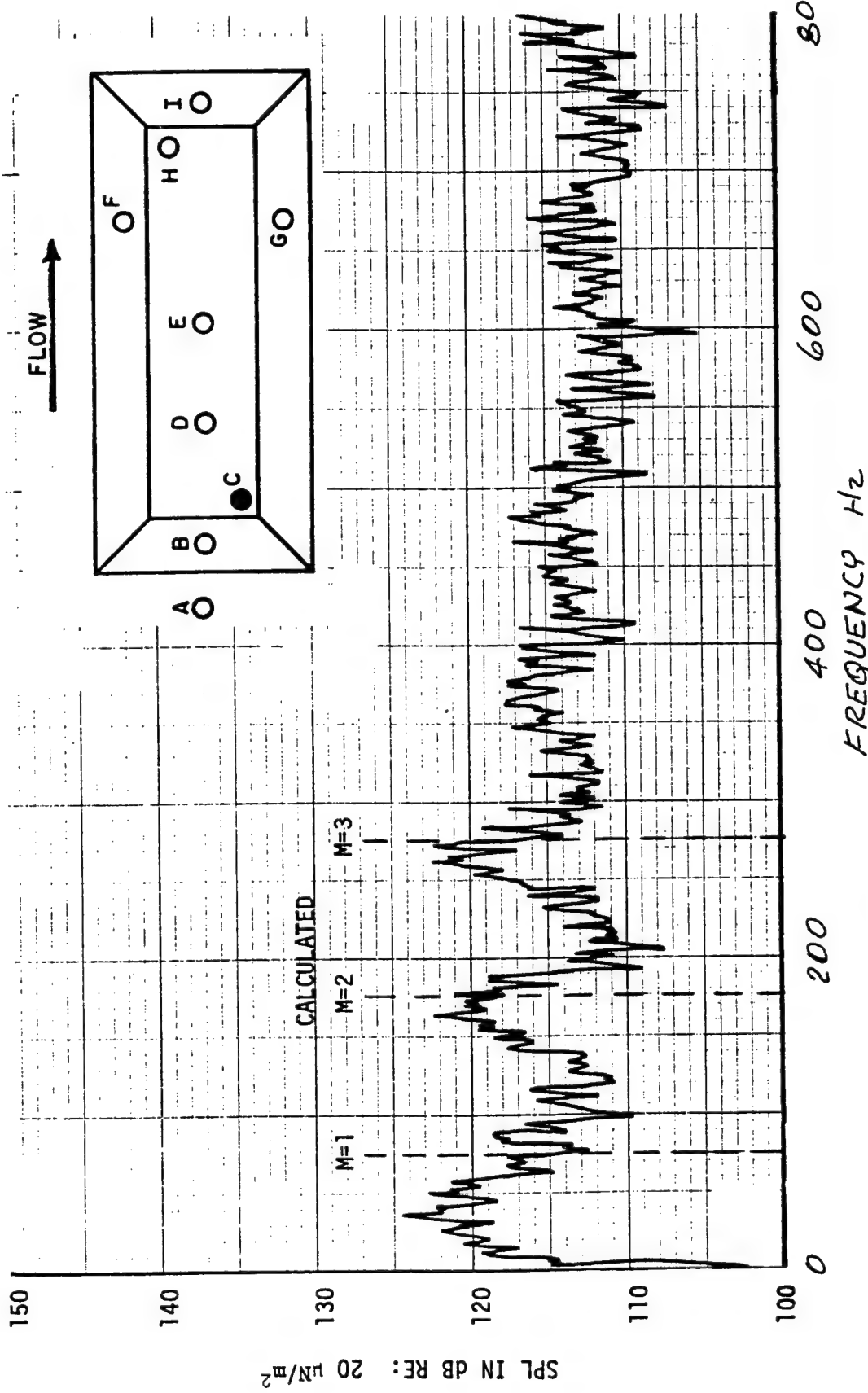


FIGURE 24 NARROWBAND (2 Hz) SPECTRUM FROM MICROPHONE C FOR AN ALTITUDE OF 20,000 FEET AT MACH 0.82 FOR L/D = 7 WITH STORE

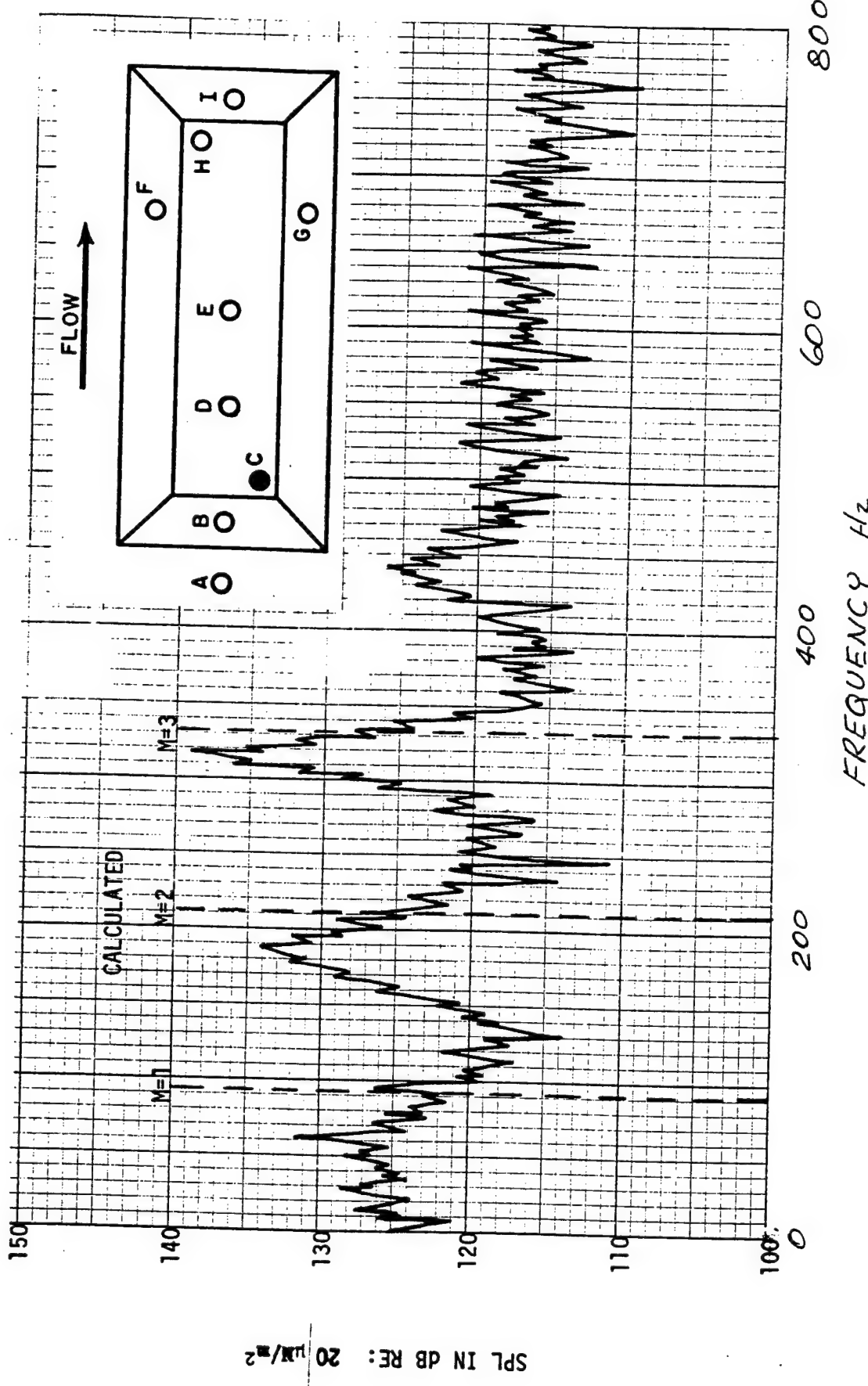


FIGURE 25 NARROWBAND (2 Hz) SPECTRUM FROM MICROPHONE C FOR AN ALTITUDE OF 20,000 FEET AT MACH 1.05 FOR $L/D = 7$ WITH STORE

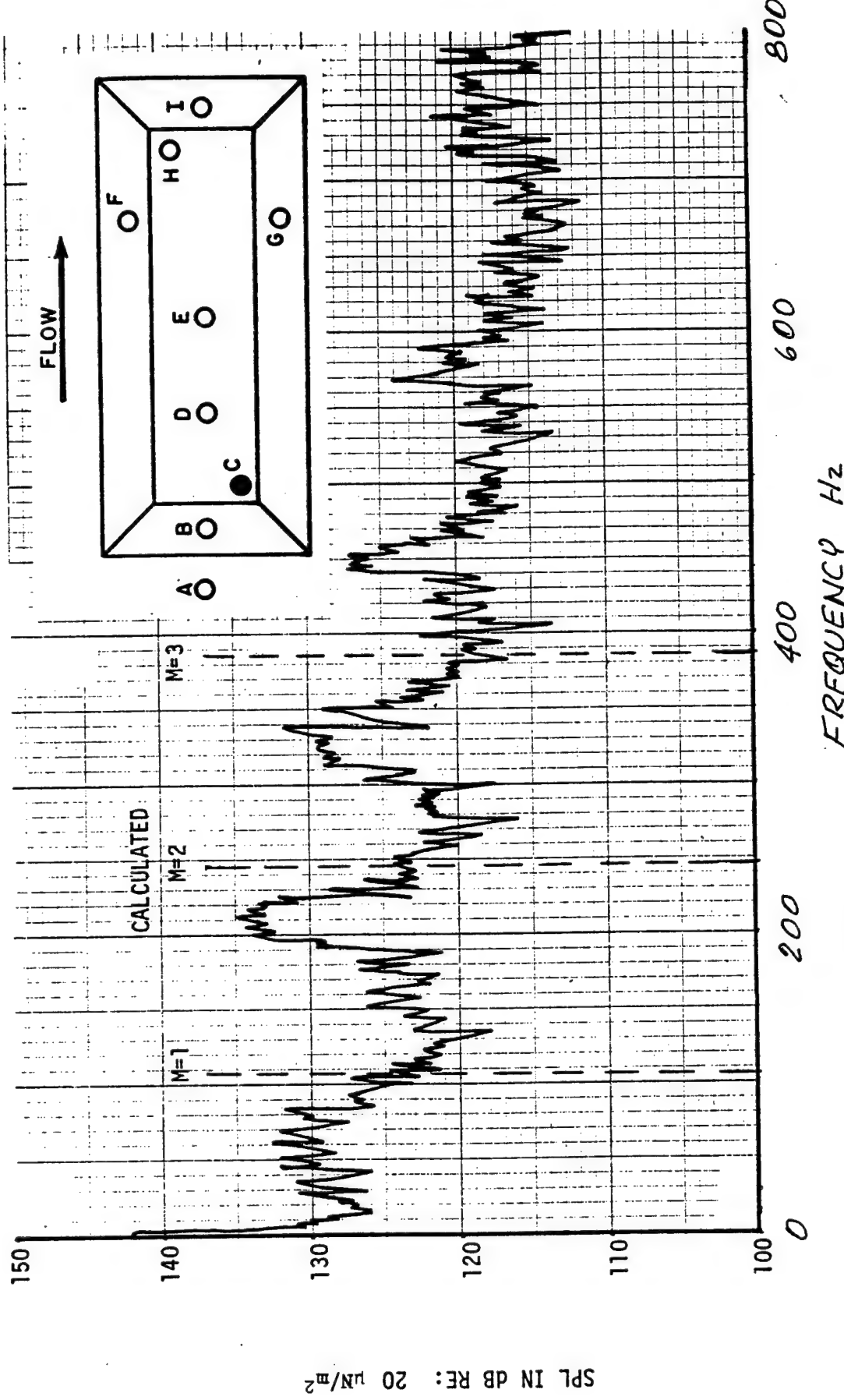


FIGURE 26 NARROWBAND (2 Hz) SPECTRUM FROM MICROPHONE C FOR AN ALTITUDE OF 20,000 FEET AT MACH 1.30 FOR $L/D = 7$ WITH STORE

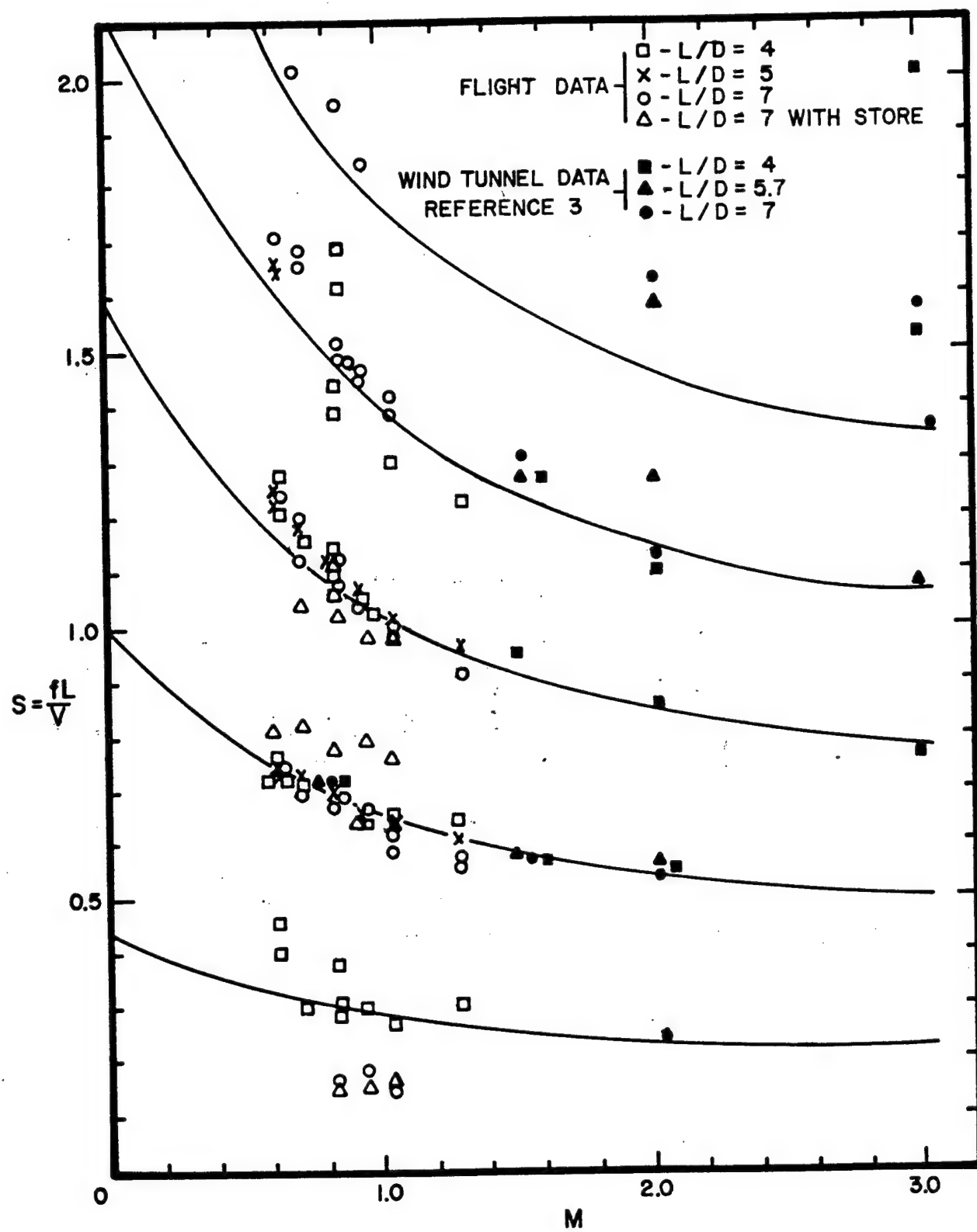
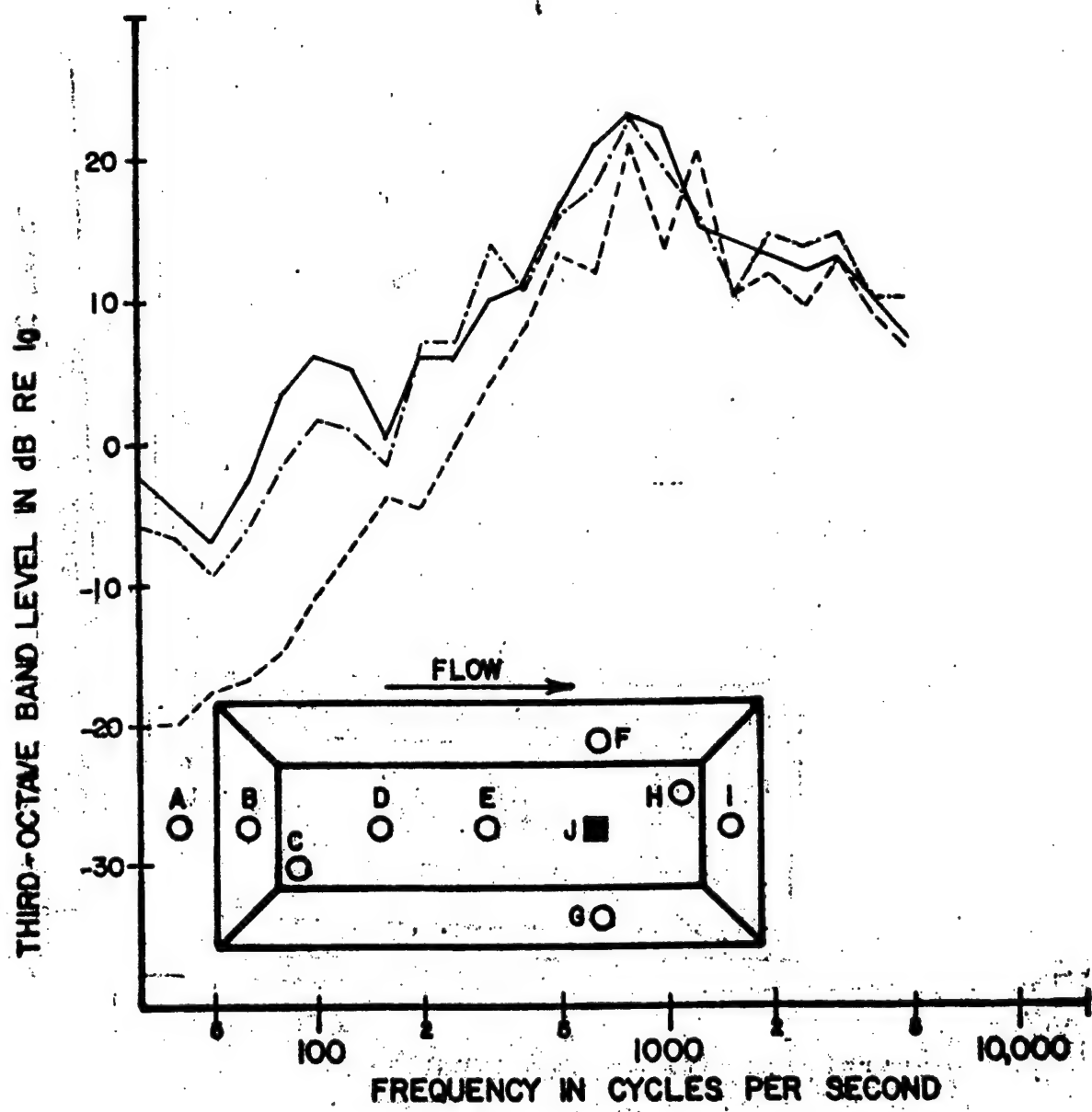


FIGURE 27 NONDIMENSIONAL RESONANT FREQUENCIES AS A FUNCTION OF MACH NUMBER



----- L/D = 5 | WITHOUT
 ----- L/D = 7 |
 ----- L/D = 7 WITH STORE

FIGURE 28 ACCELERATION SPECTRA FROM ACCELEROMETER J AT AN ALTITUDE OF 3,000 FEET AND MACH NUMBER OF 0.82

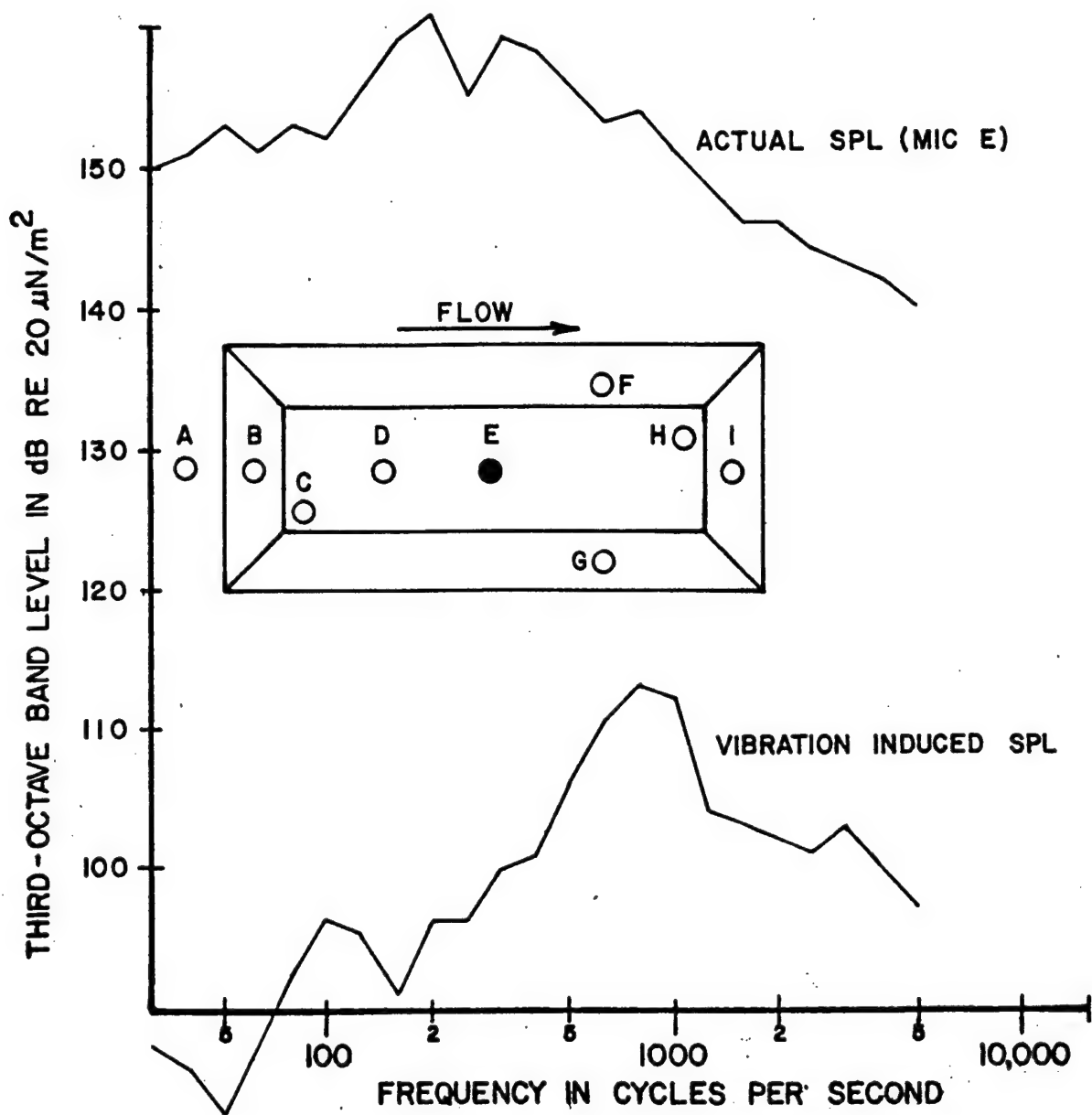


FIGURE 29 COMPARISON OF ACTUAL AND VIBRATION INDUCED SPL FOR THE L/D = 7 CONFIGURATION AT A MACH NUMBER OF 0.82 AND ALTITUDE OF 3,000 FEET

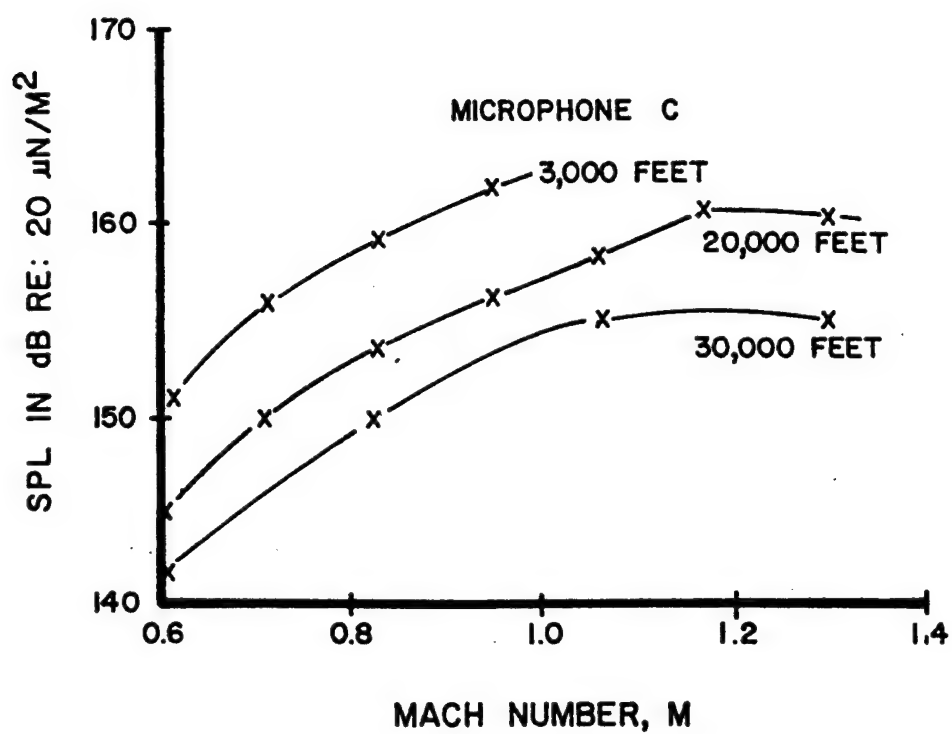
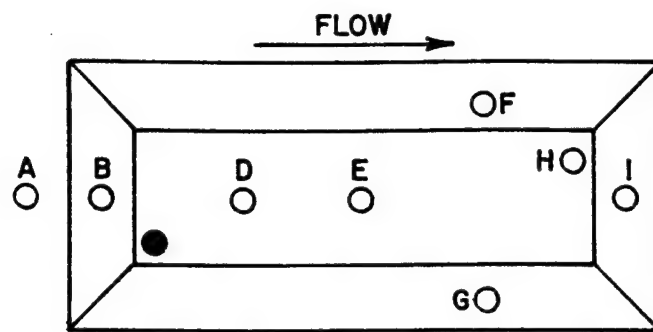


FIGURE 30 OVERALL TIME HISTORIES FROM THE MODIFIED SUU-41 POD FOR L/D = 5

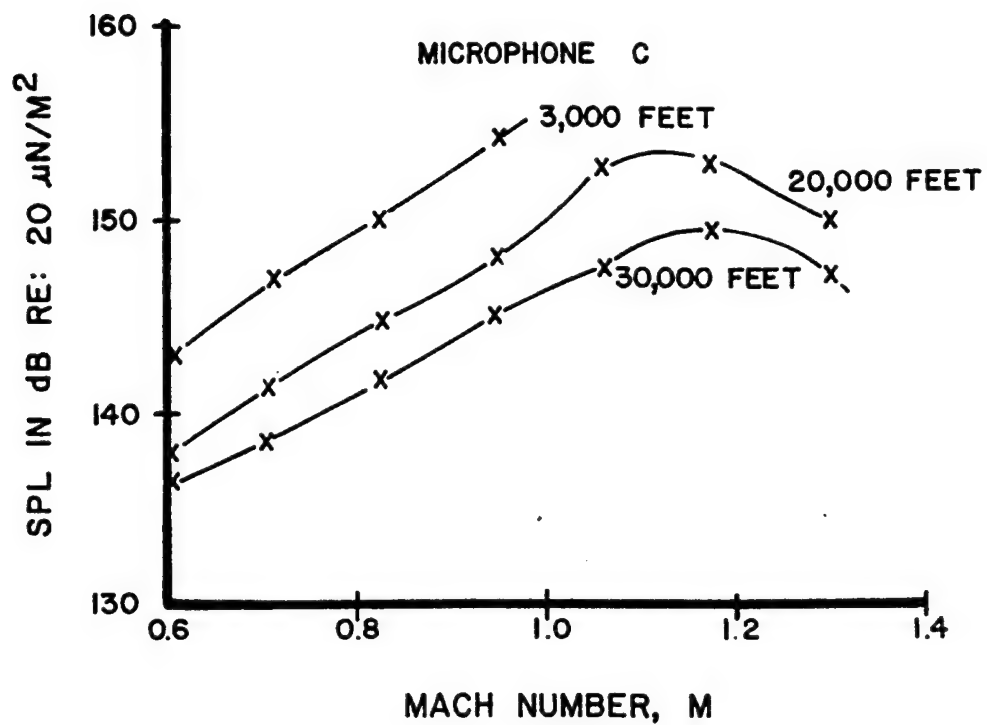
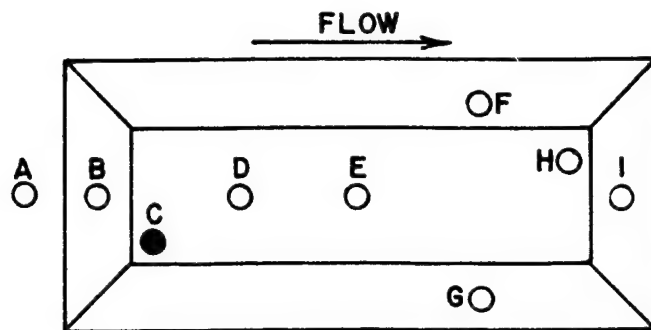


FIGURE 31 OVERALL TIME HISTORIES FROM THE MODIFIED SUU-41 POD FOR $L/D = 7$

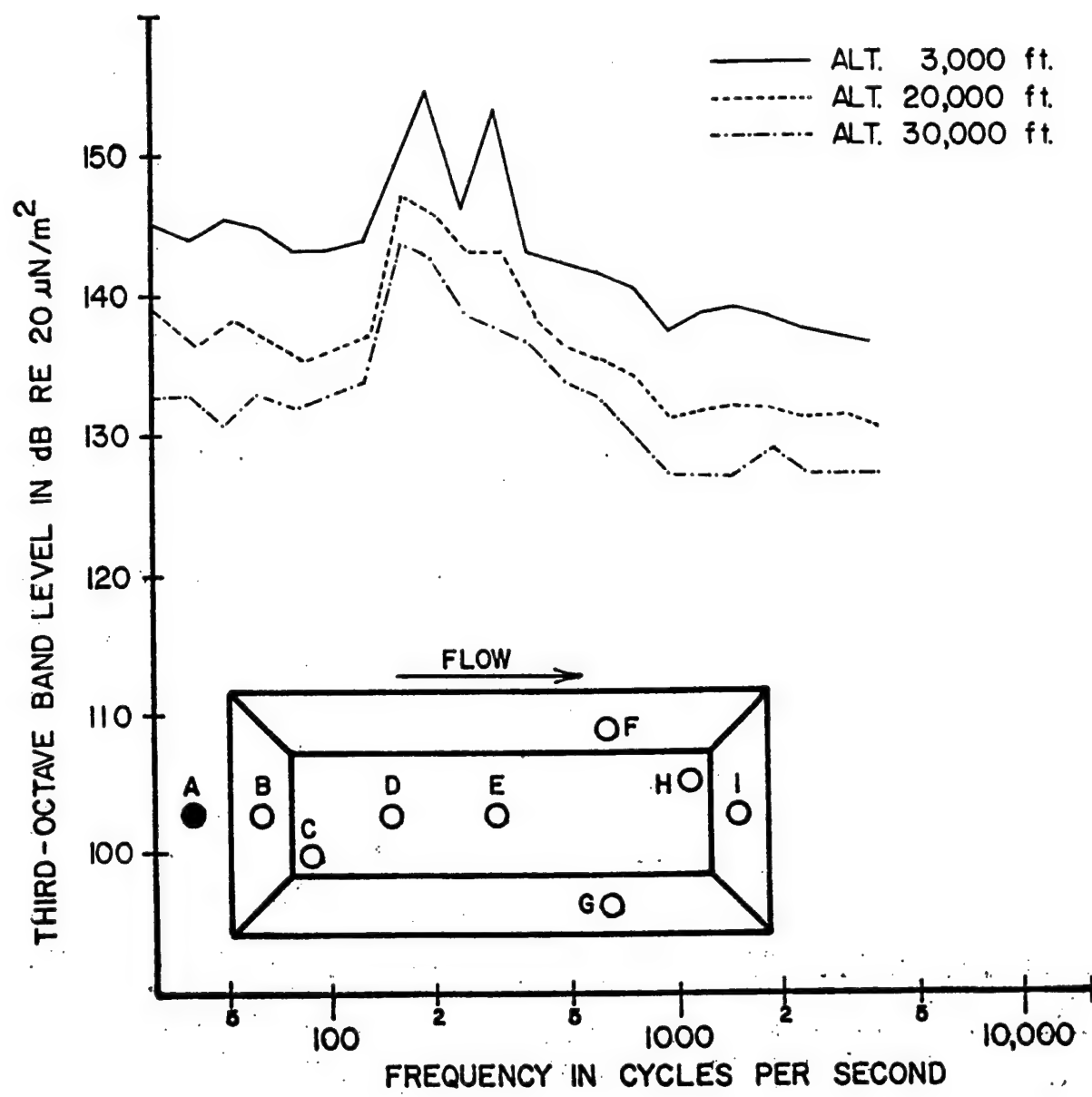


FIGURE 32 ONE-THIRD OCTAVE BAND SPECTRA FROM MICROPHONE A
 FOR A MACH NUMBER OF 0.82 AND L/D RATIO OF 5

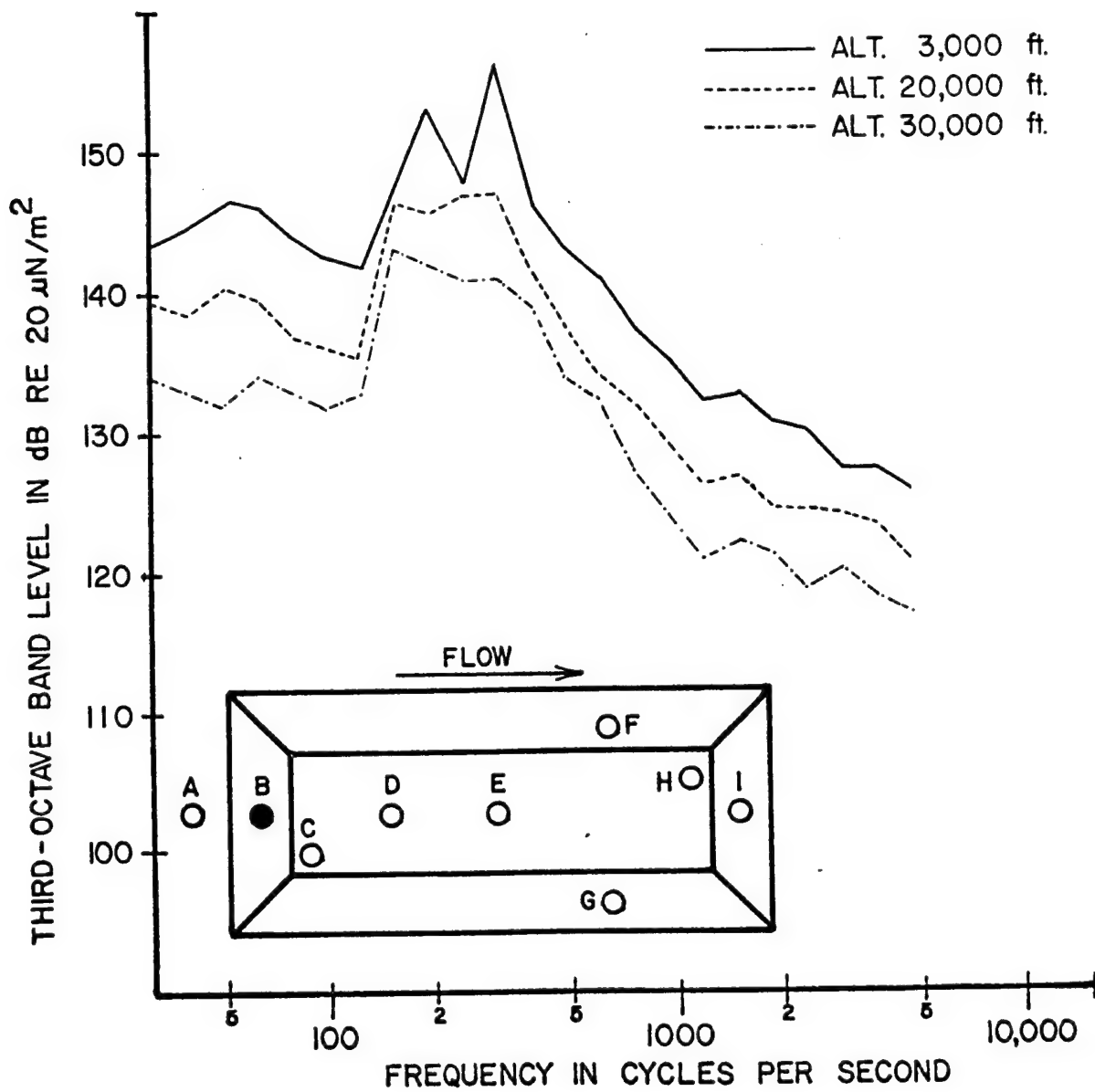


FIGURE 33 ONE-THIRD OCTAVE BAND SPECTRA FROM MICROPHONE B FOR A MACH NUMBER OF 0.82 AND L/D RATIO OF 5

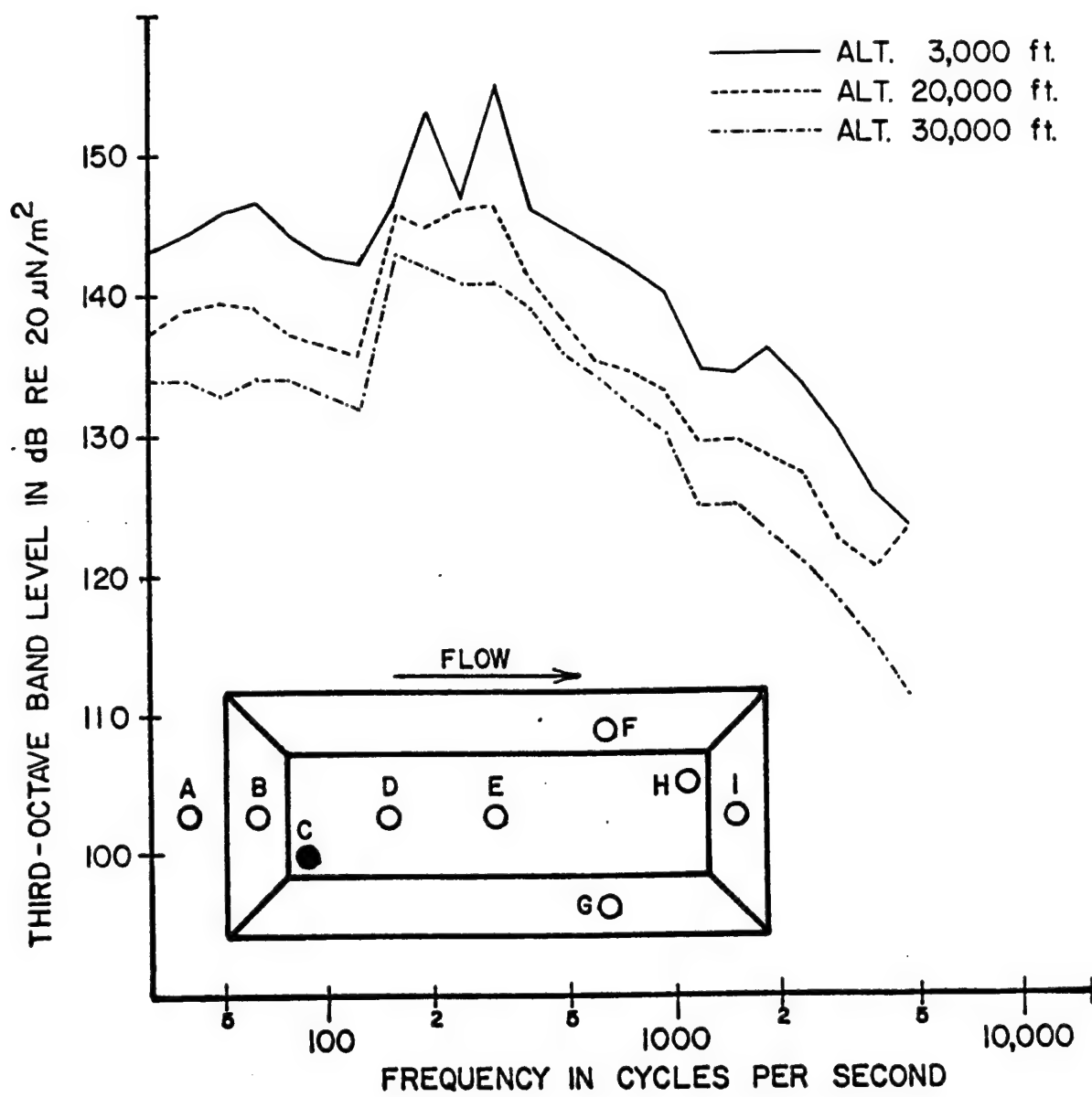


FIGURE 34 ONE-THIRD OCTAVE BAND SPECTRA FROM MICROPHONE C
 FOR A MACH NUMBER OF 0.82 AND L/D RATIO OF 5

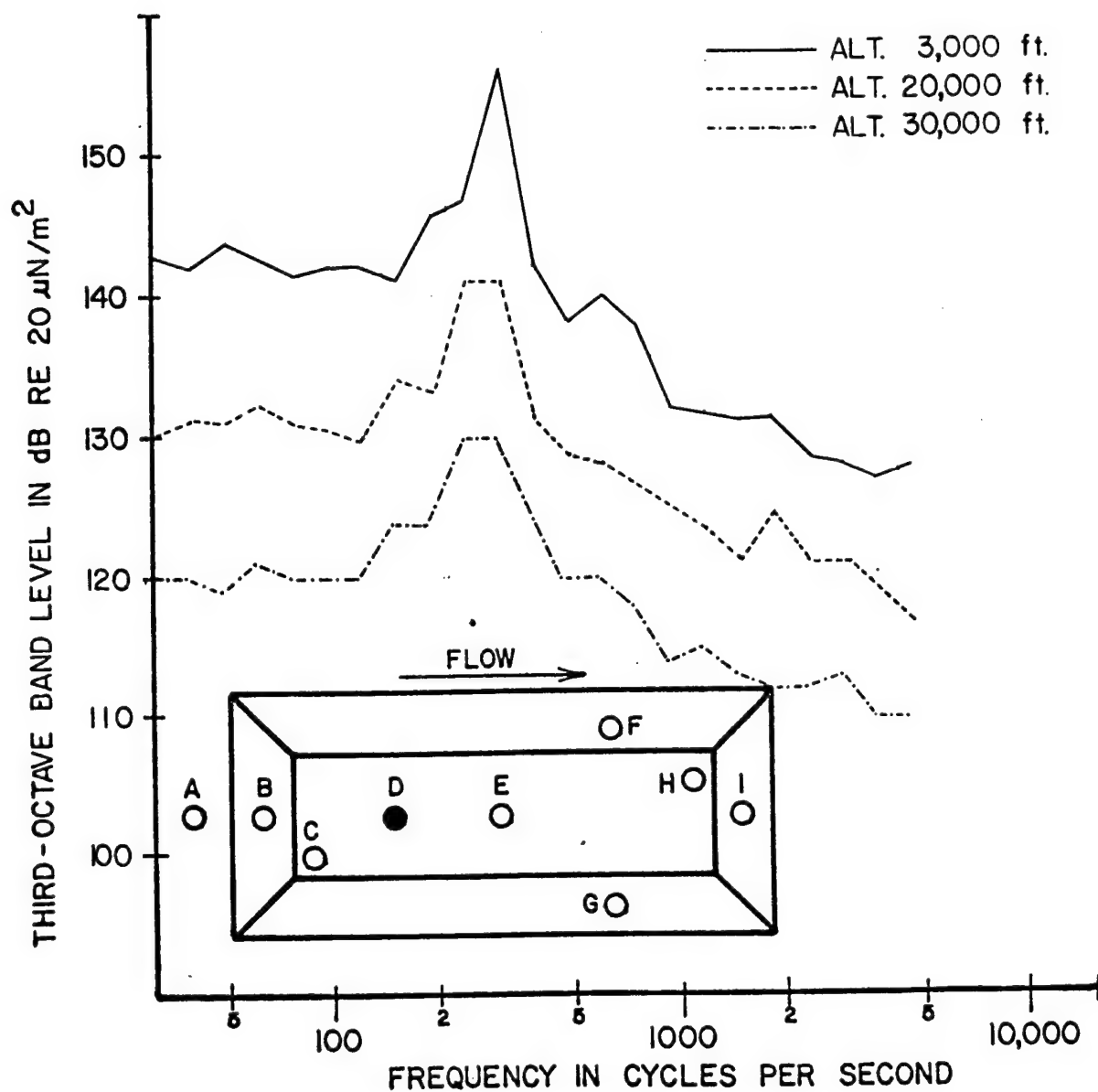


FIGURE 35 ONE-THIRD OCTAVE BAND SPECTRA FROM MICROPHONE D FOR A MACH NUMBER OF 0.82 AND L/D RATIO OF 5

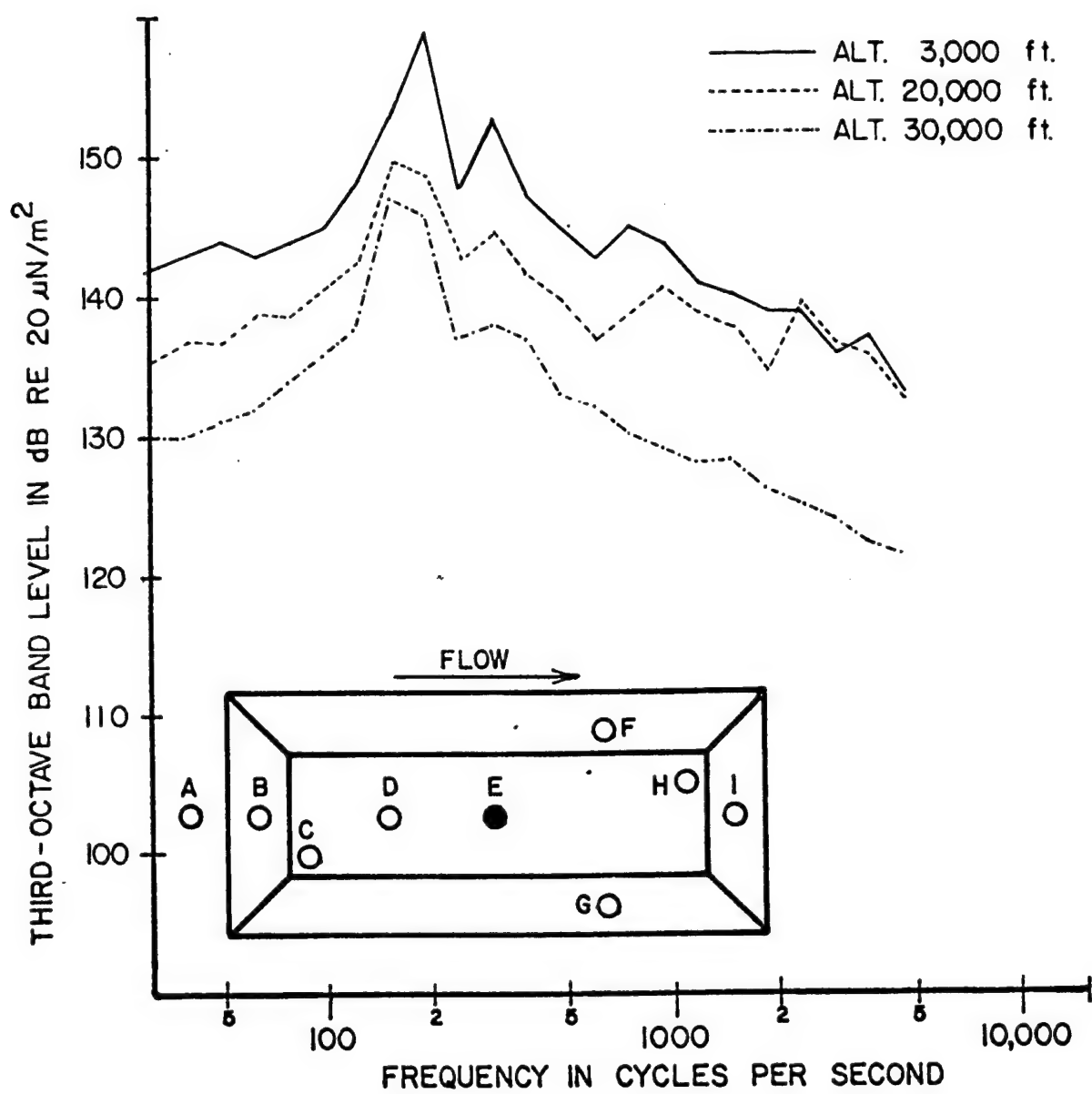


FIGURE 36 ONE-THIRD OCTAVE BAND SPECTRA FROM MICROPHONE E
FOR A MACH NUMBER OF 0.82 AND L/D RATIO OF 5

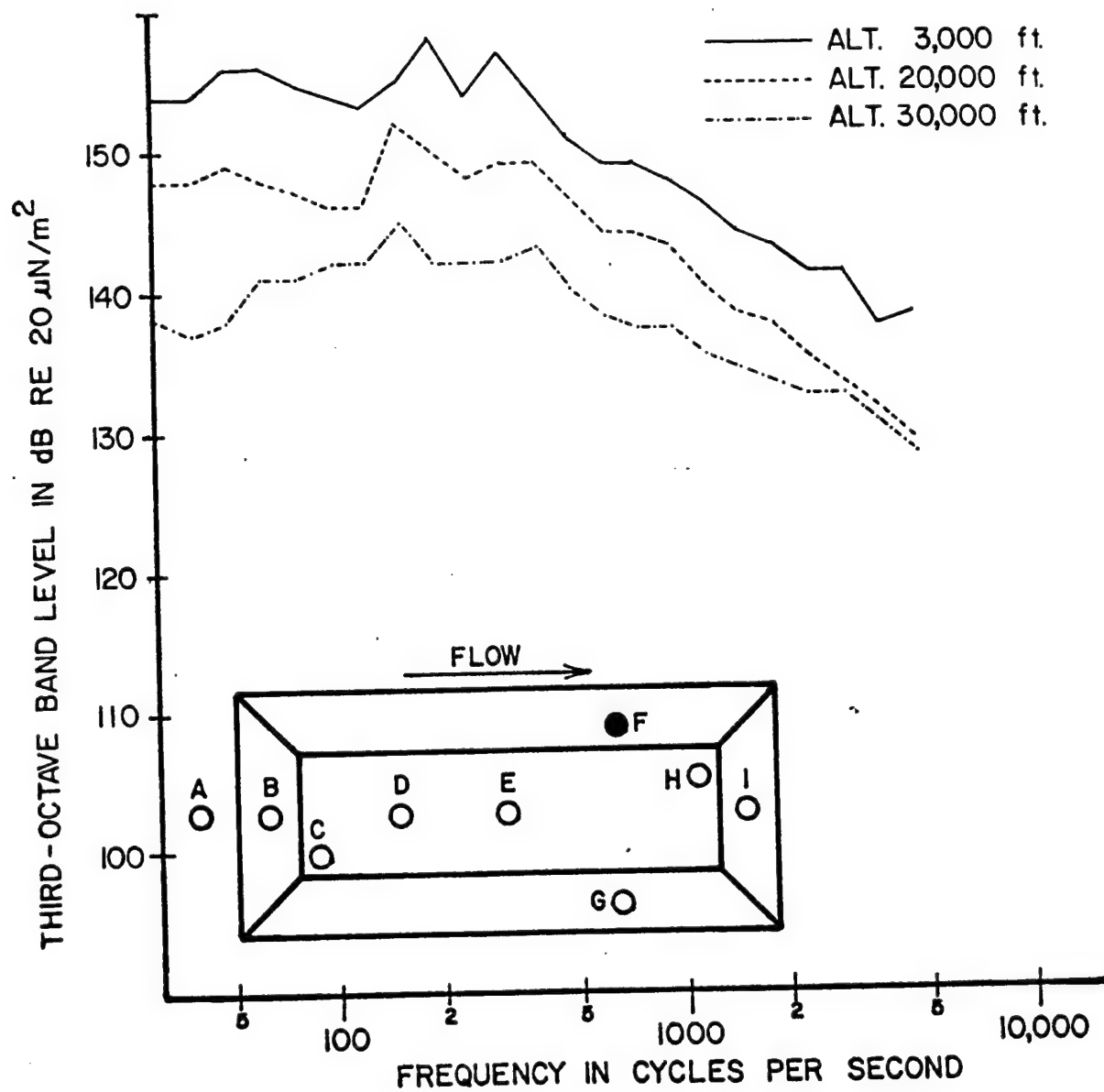


FIGURE 37 ONE-THIRD OCTAVE BAND SPECTRA FROM MICROPHONE F FOR A MACH NUMBER OF 0.82 AND L/D RATIO OF 5

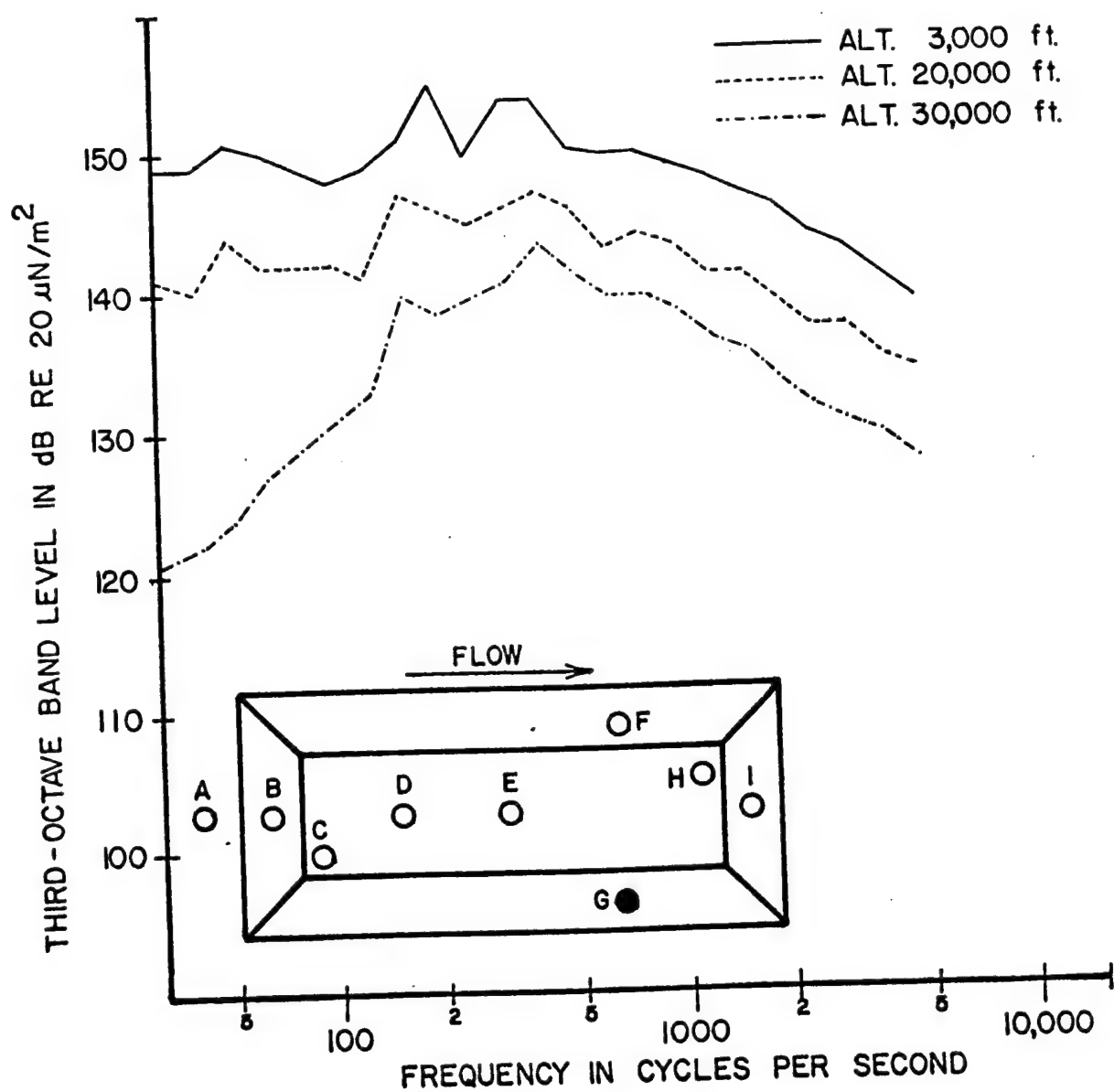


FIGURE 38 ONE-THIRD OCTAVE BAND SPECTRA FROM MICROPHONE G
FOR A MACH NUMBER OF 0.82 AND L/D RATIO OF 5

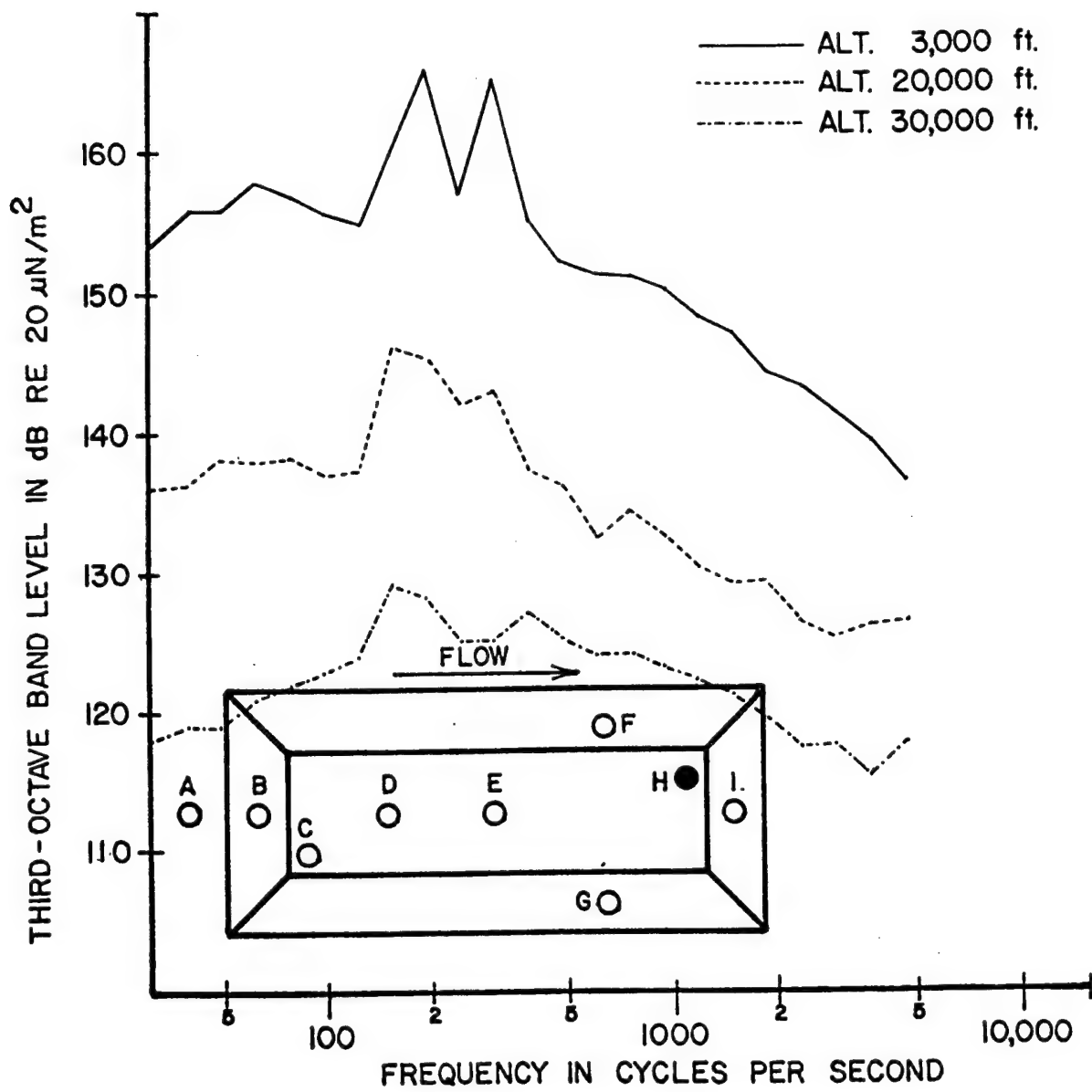


FIGURE 39 ONE-THIRD OCTAVE BAND SPECTRA FROM MICROPHONE H
FOR A MACH NUMBER OF 0.82 AND L/D RATIO OF 5

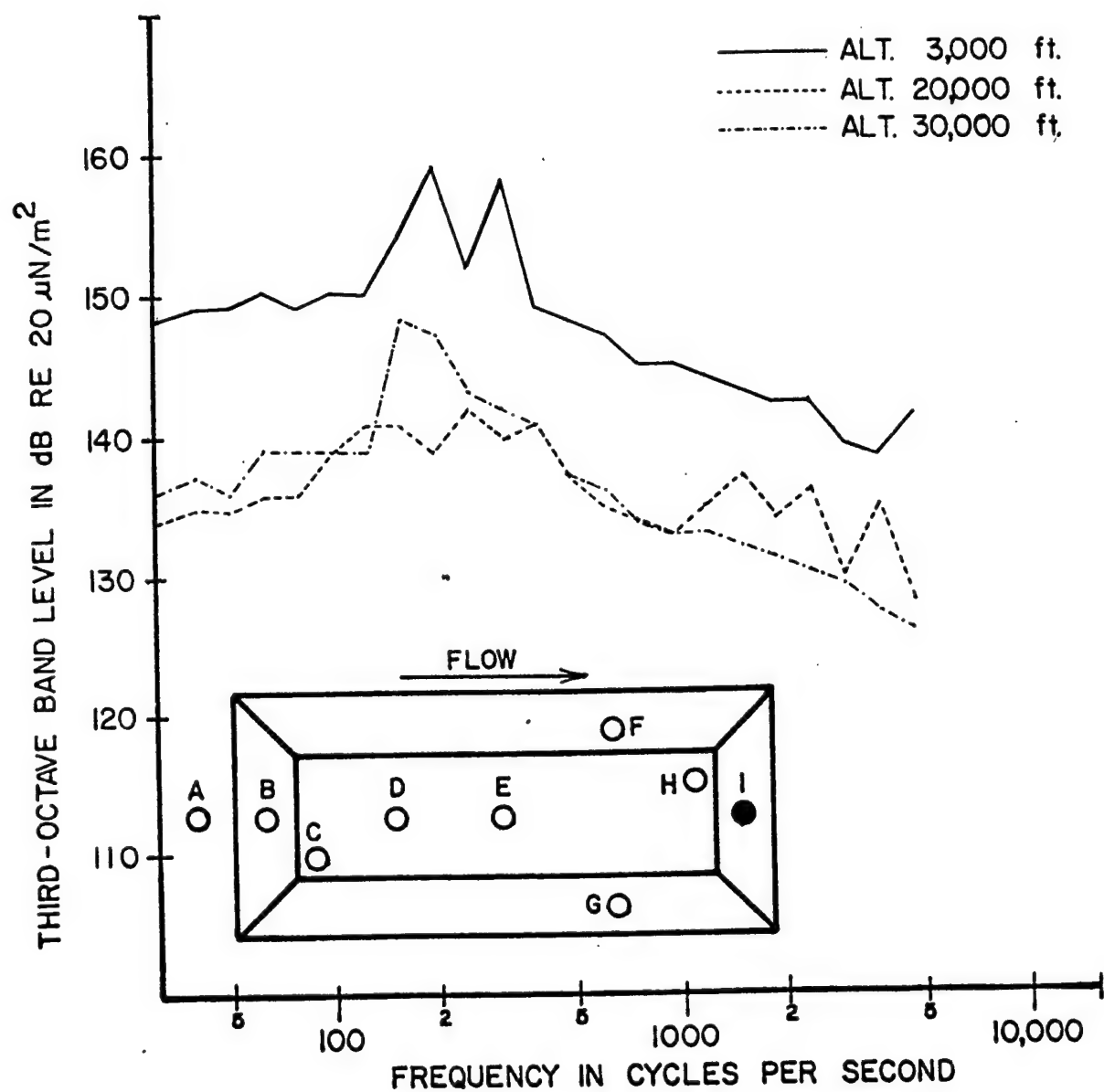


FIGURE 40 ONE-THIRD OCTAVE BAND SPECTRA FROM MICROPHONE I
FOR A MACH NUMBER OF 0.82 AND L/D RATIO OF 5

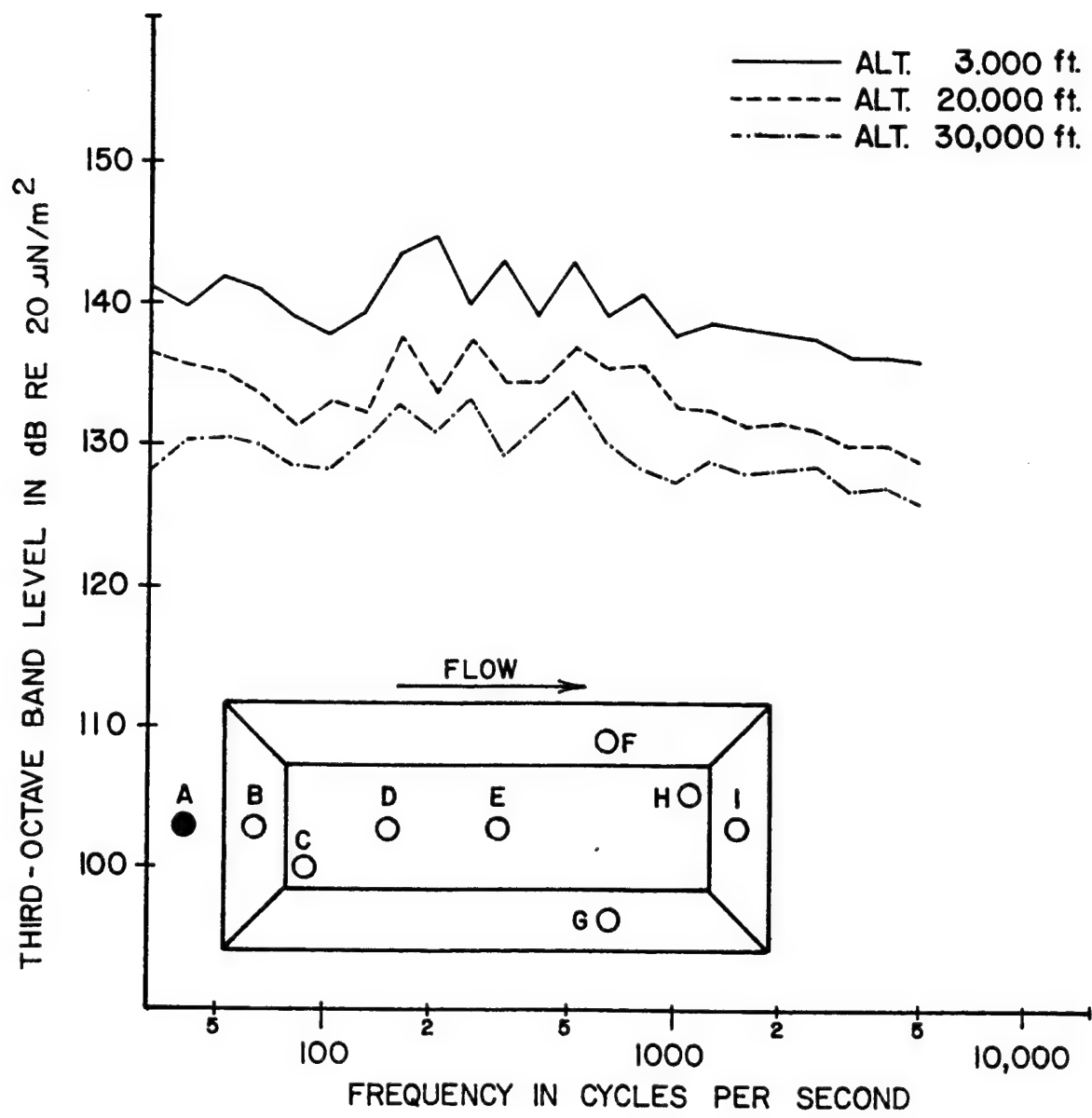


FIGURE 41 ONE-THIRD OCTAVE BAND SPECTRA FROM MICROPHONE A FOR A MACH NUMBER OF 0.82 AND L/D RATIO OF 7

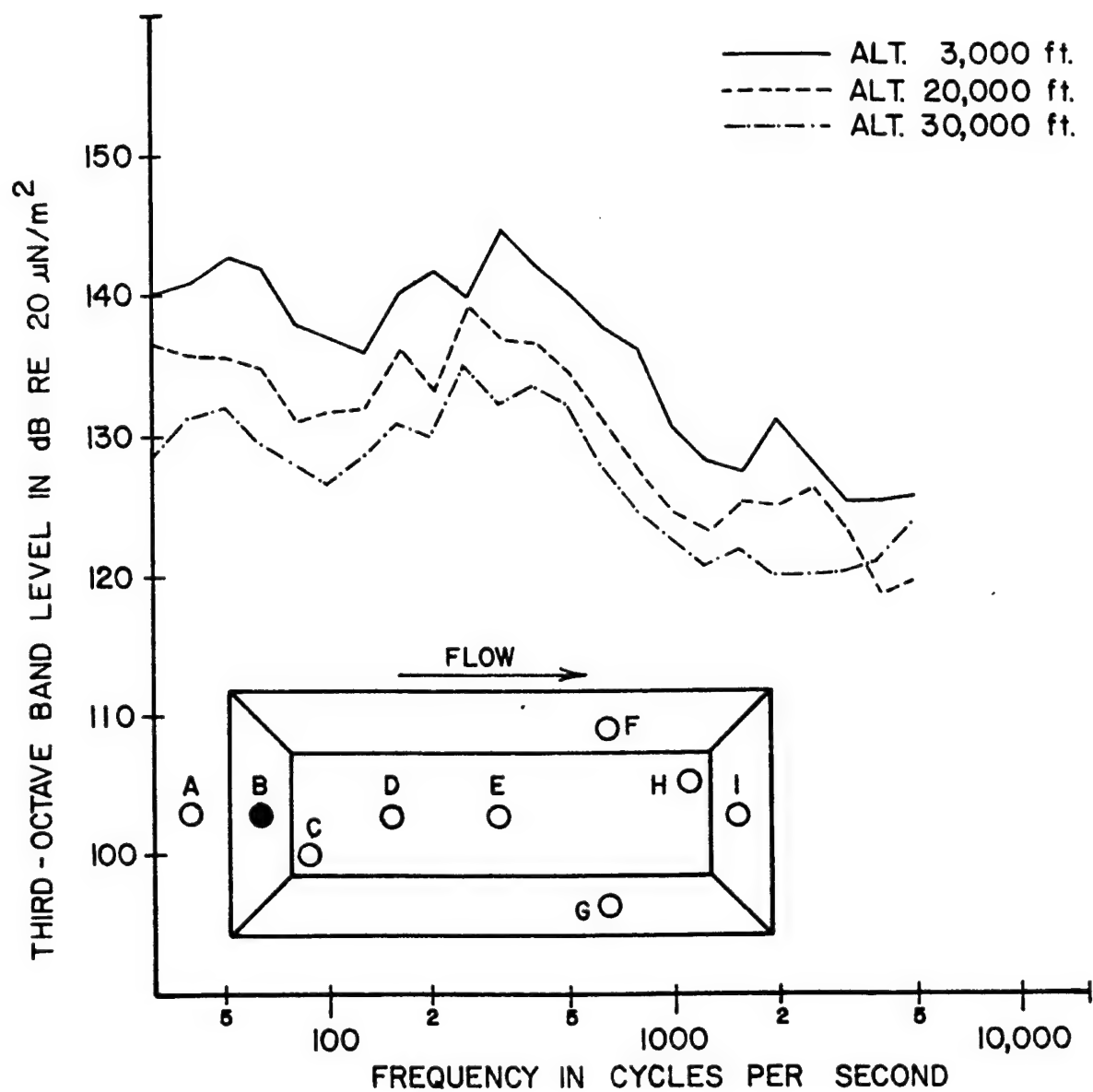


FIGURE 42 ONE-THIRD OCTAVE BAND SPECTRA FROM MICROPHONE B
FOR A MACH NUMBER OF 0.82 AND L/D RATIO OF 7

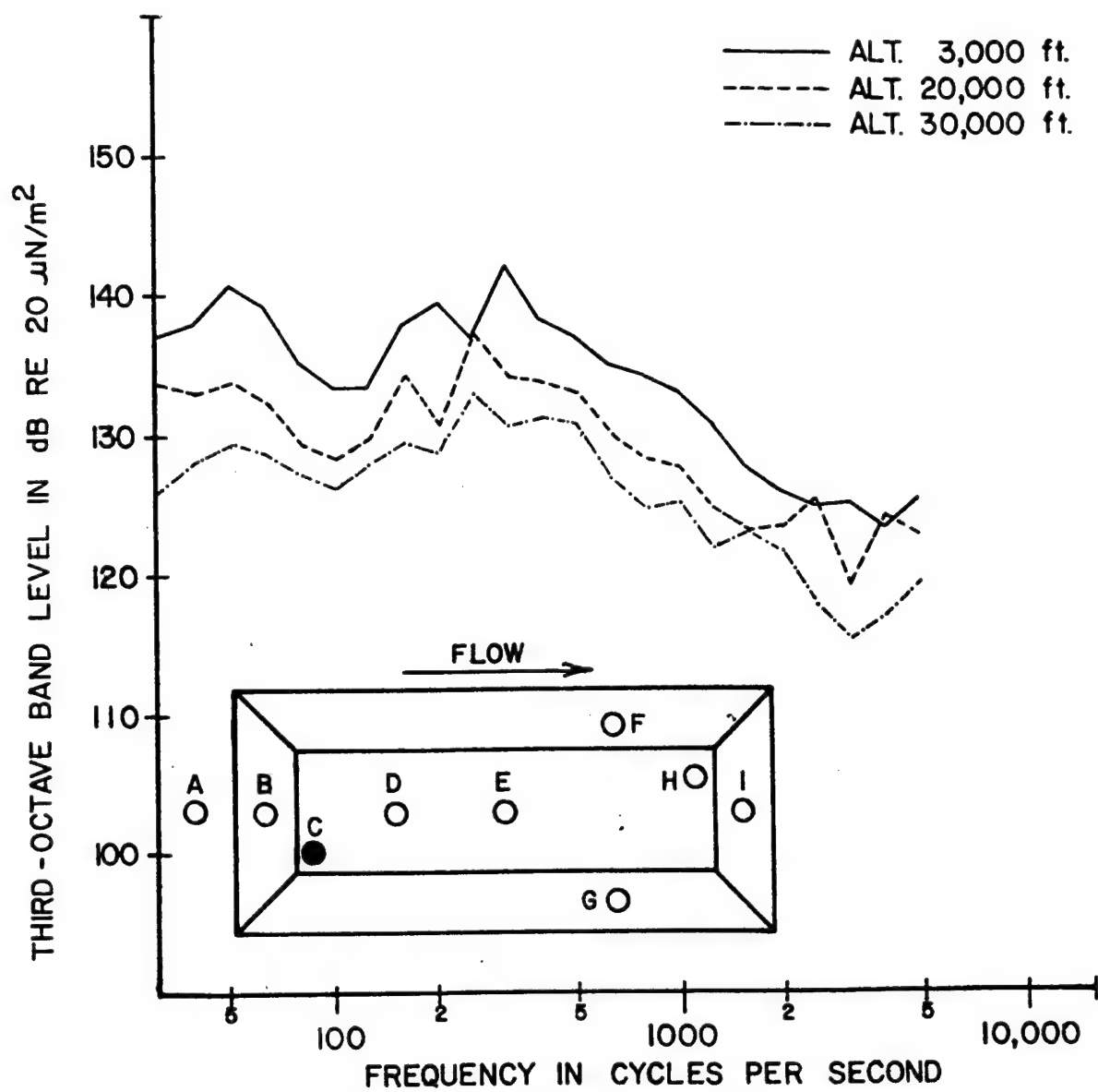


FIGURE 43 ONE-THIRD OCTAVE BAND SPECTRA FROM MICROPHONE C FOR A MACH NUMBER OF 0.82 AND L/D RATIO OF 7

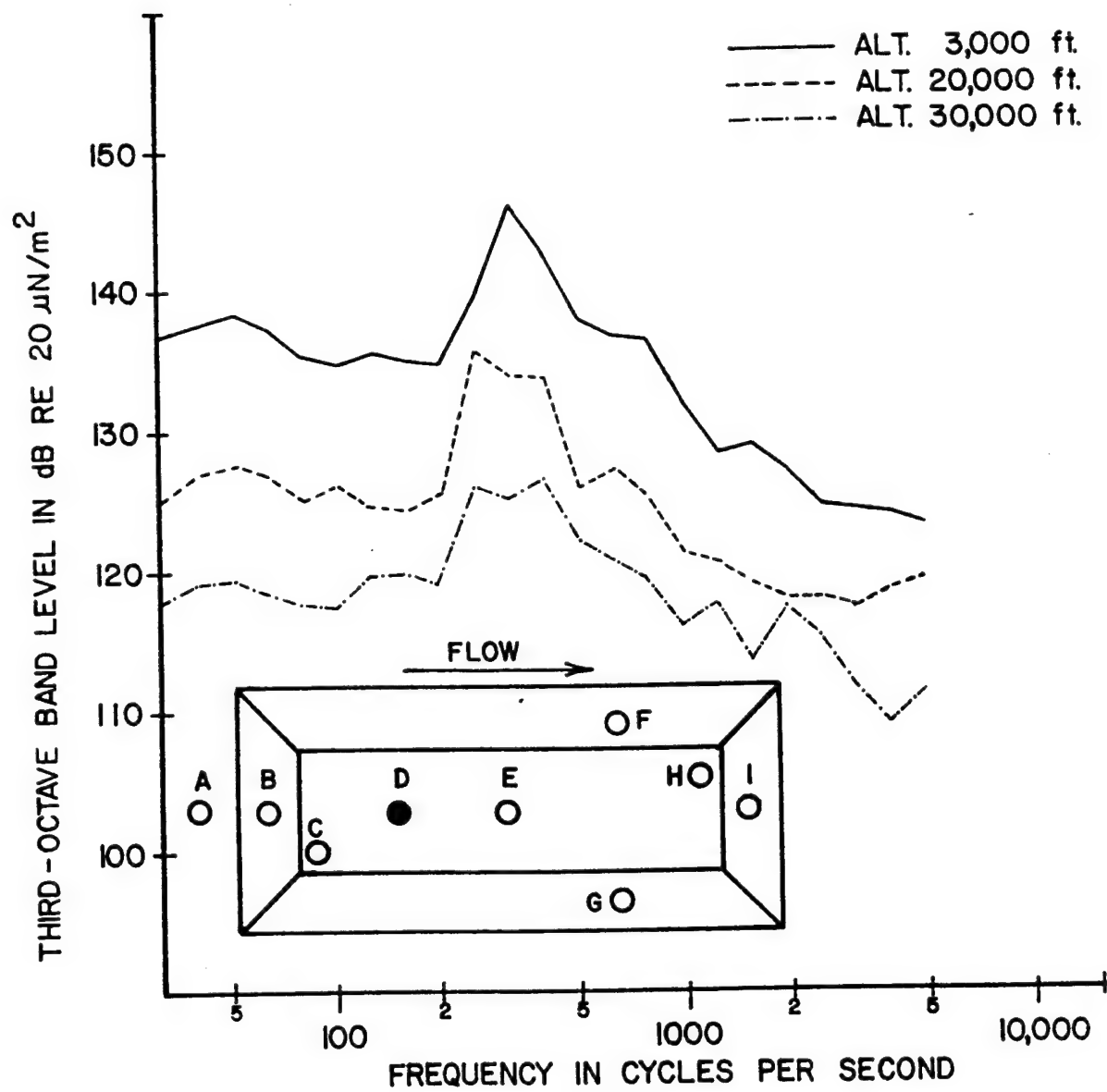


FIGURE 44 ONE-THIRD OCTAVE BAND SPECTRA FROM MICROPHONE D FOR A MACH NUMBER OF 0.82 AND L/D RATIO OF 7

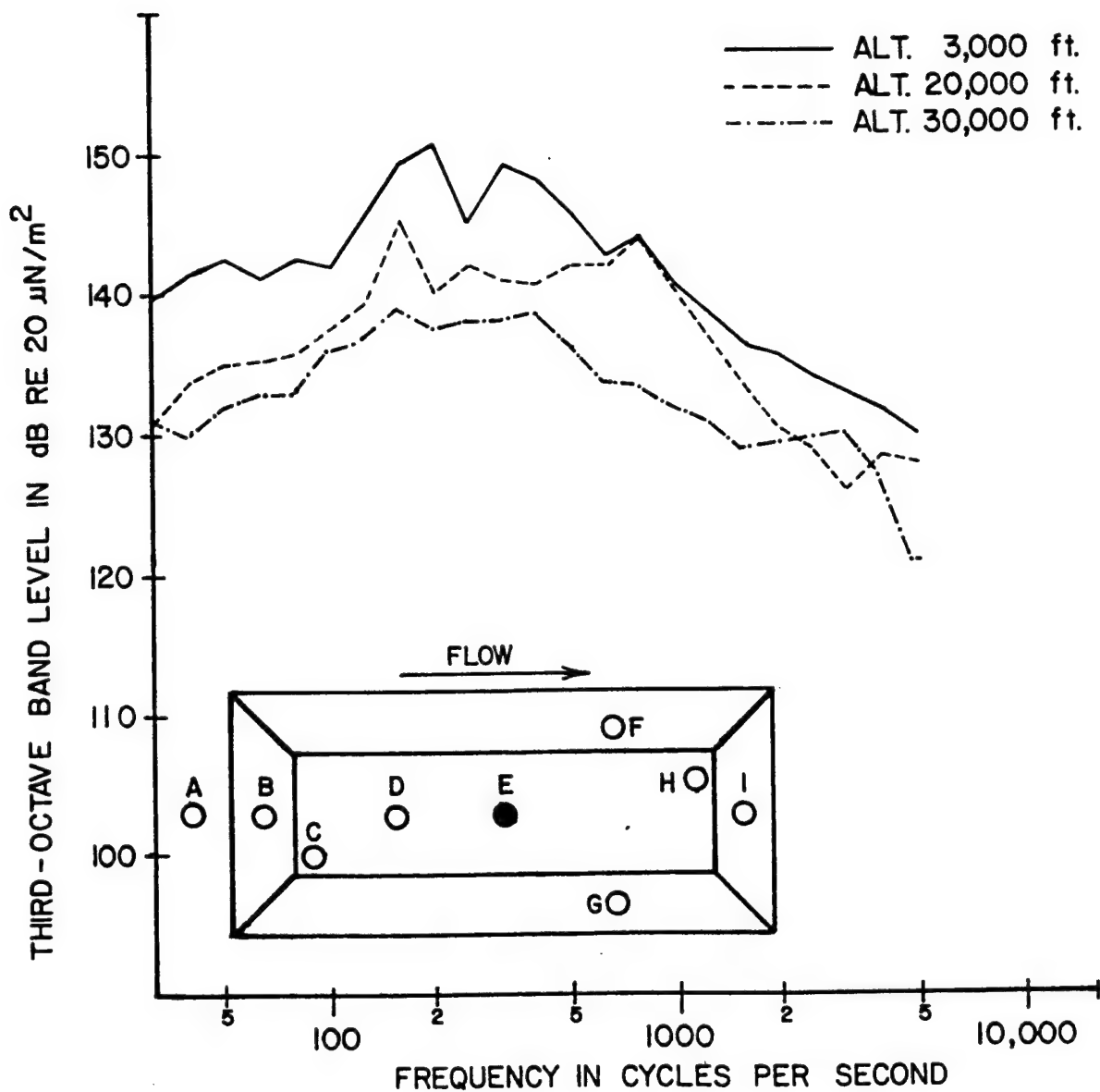


FIGURE 45 ONE-THIRD OCTAVE BAND SPECTRA FROM MICROPHONE E
FOR A MACH NUMBER OF 0.82 AND L/D RATIO OF 7

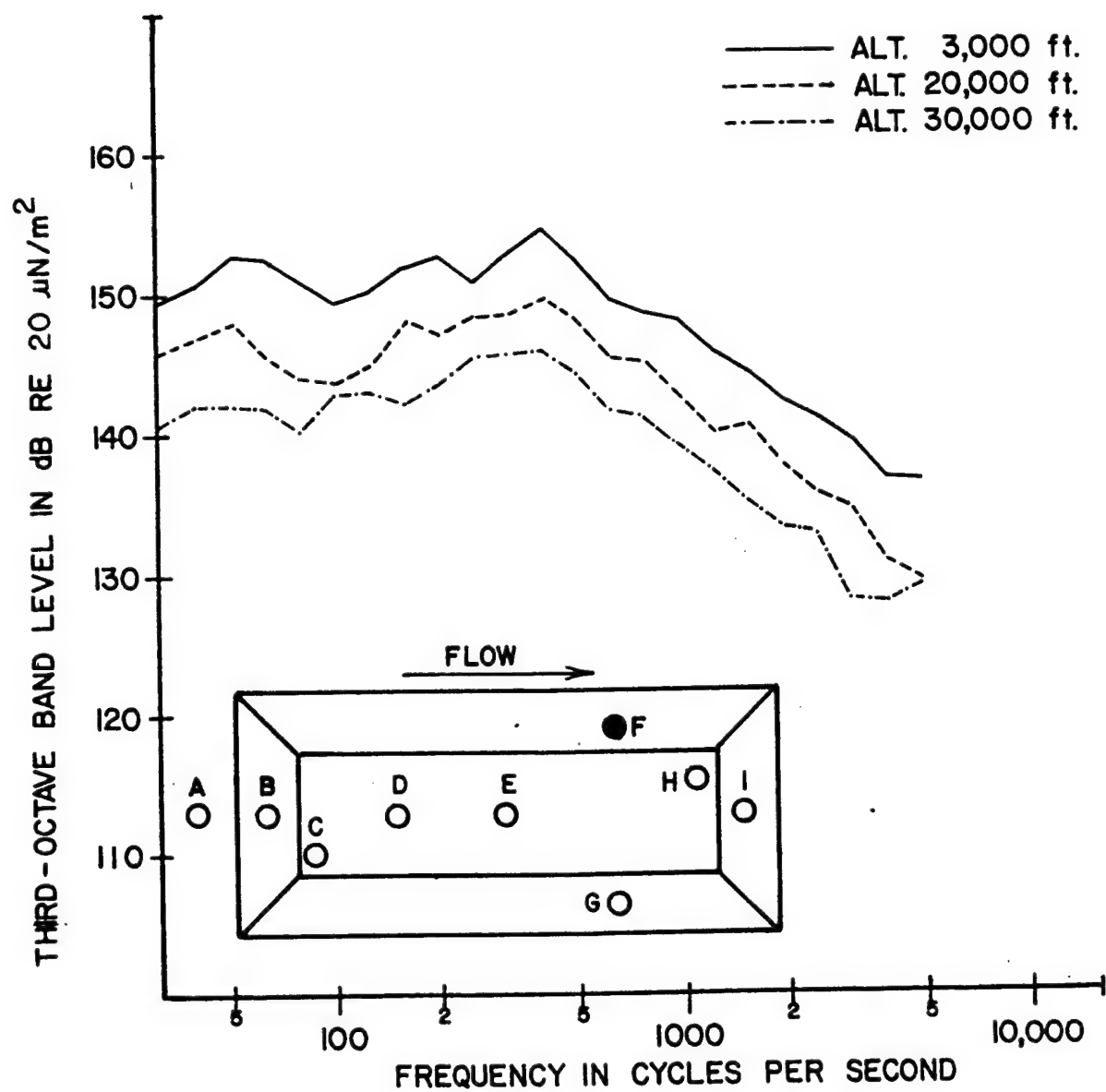


FIGURE 46 ONE-THIRD OCTAVE BAND SPECTRA FROM MICROPHONE F
 FOR A MACH NUMBER OF 0.82 AND L/D RATIO OF 7

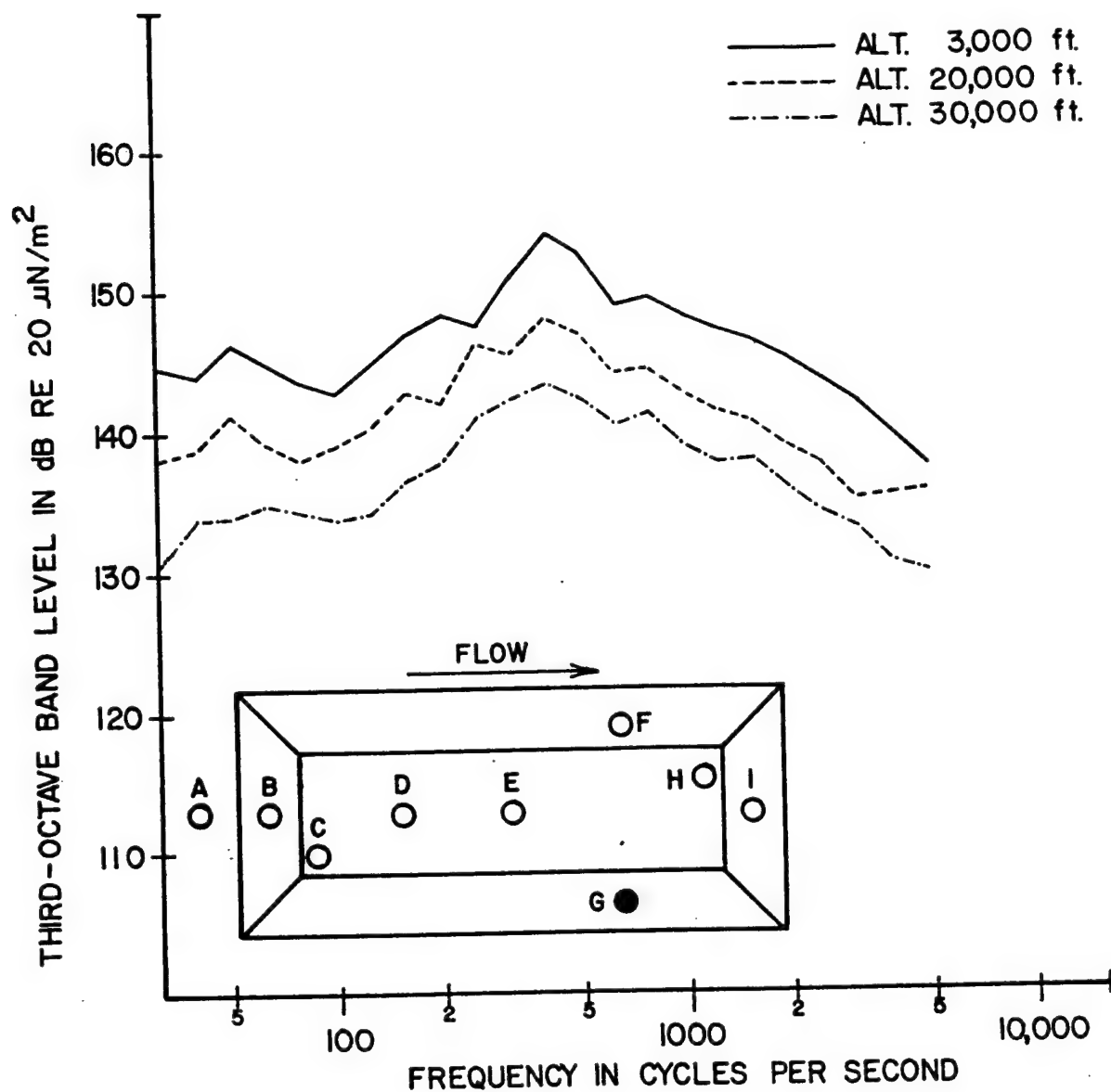


FIGURE 47 ONE-THIRD OCTAVE BAND SPECTRA FROM MICROPHONE G FOR A MACH NUMBER OF 0.82 AND L/D RATIO OF 7

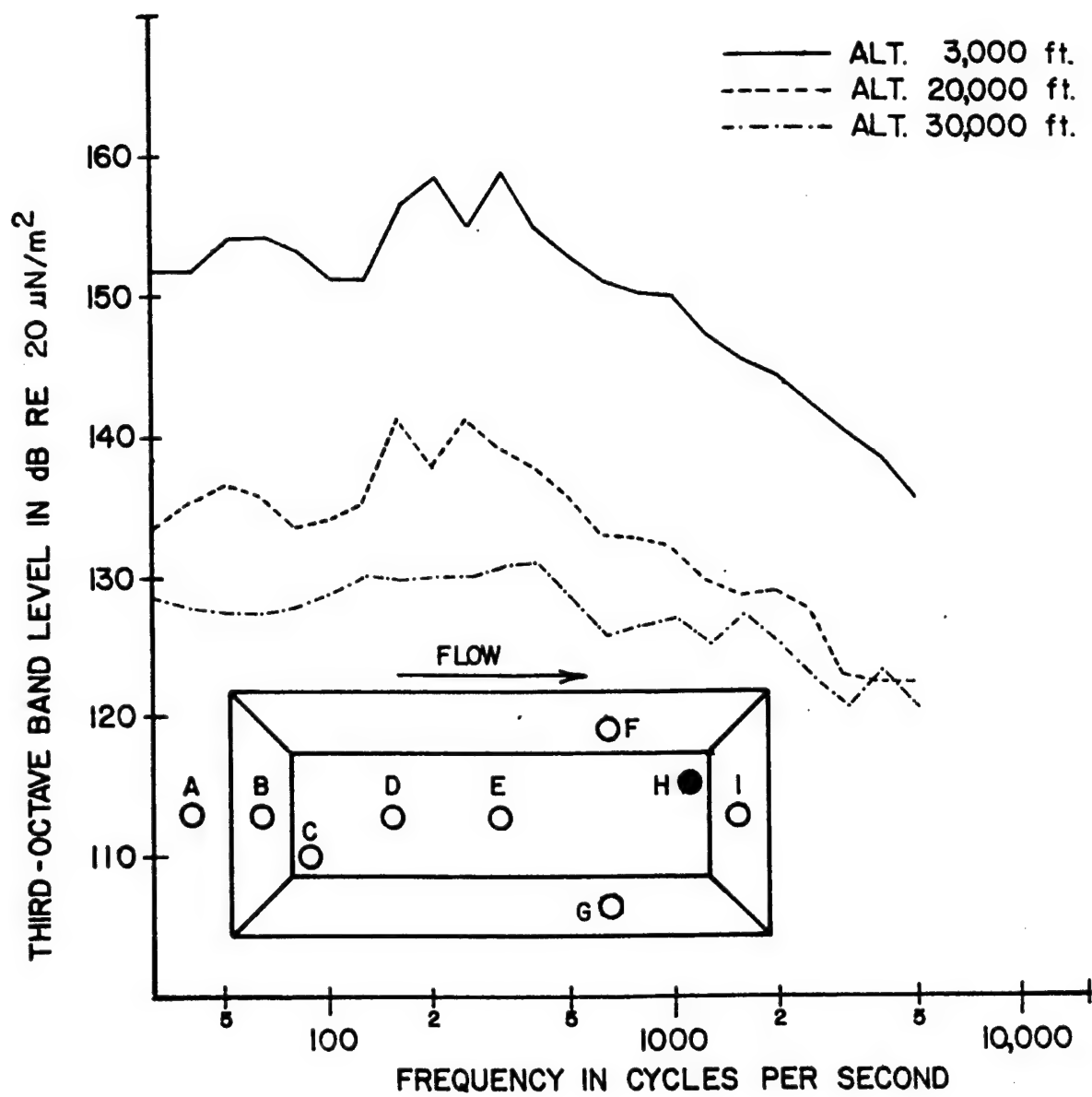


FIGURE 48 ONE-THIRD OCTAVE BAND SPECTRA FROM MICROPHONE H
FOR A MACH NUMBER OF 0.82 AND L/D RATIO OF 7

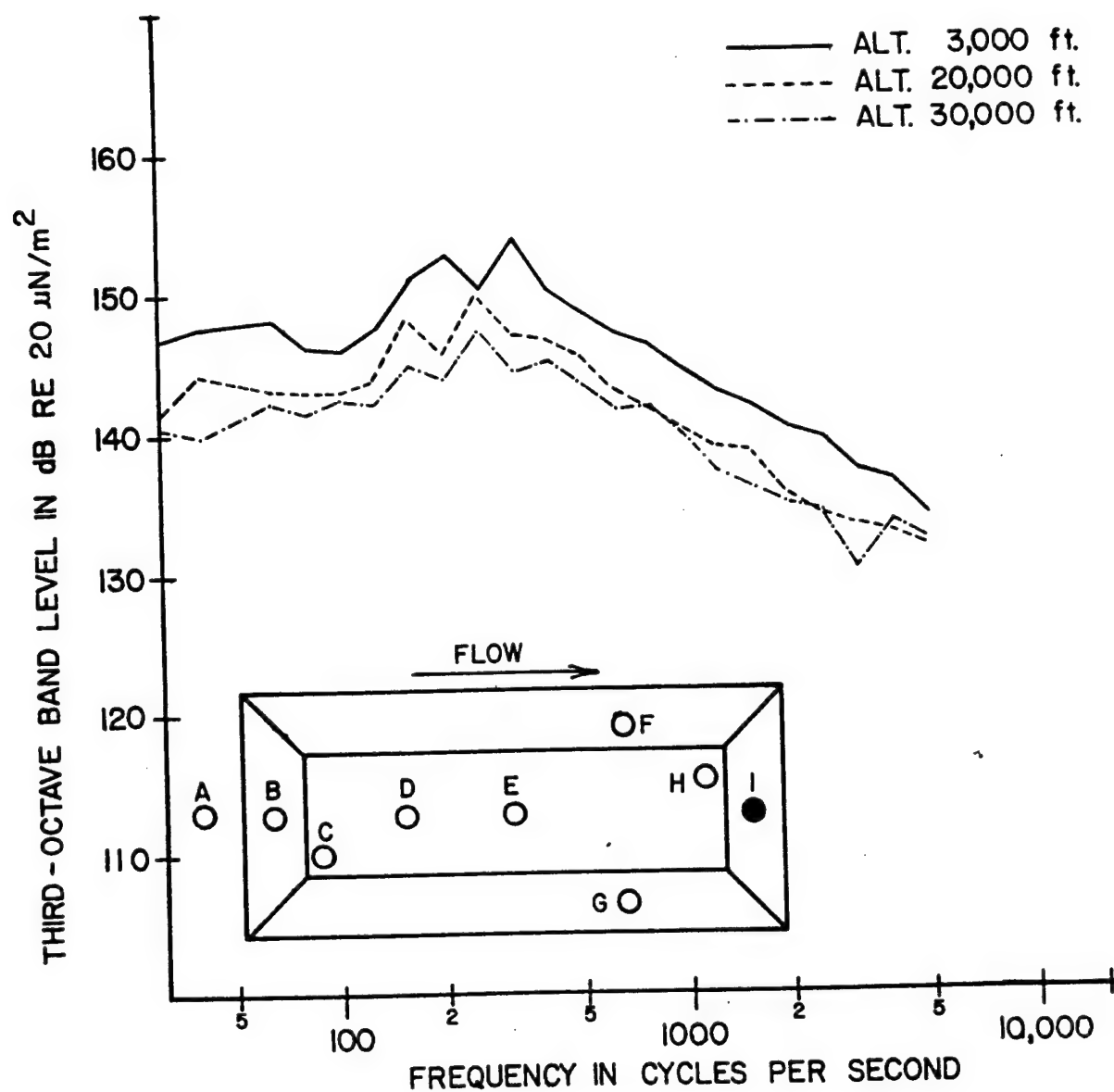


FIGURE 49 ONE-THIRD OCTAVE BAND SPECTRA FROM MICROPHONE I
 FOR A MACH NUMBER OF 0.82 AND L/D RATIO OF 7

MACH Nr. 0.82
x - 3,000 FEET
o - 20,000 FEET
□ - 30,000 FEET

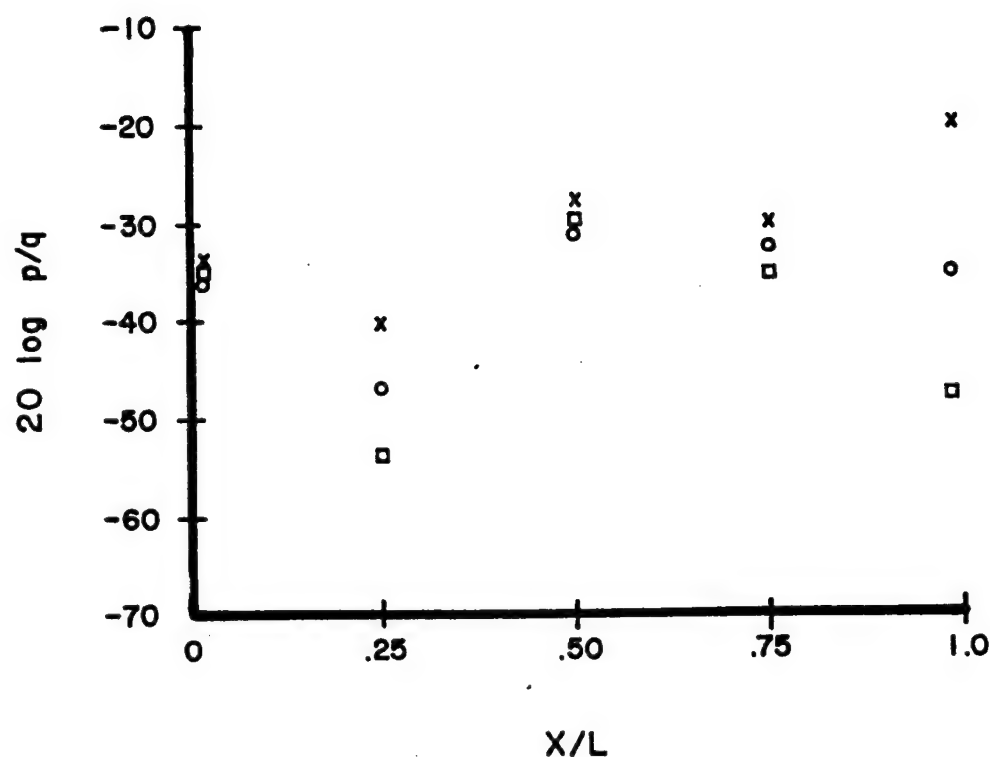


FIGURE 50 LONGITUDINAL VARIATION OF THE MODE 2 RESONANT FREQUENCY ONE-THIRD OCTAVE BAND PEAK FOR L/D = 5

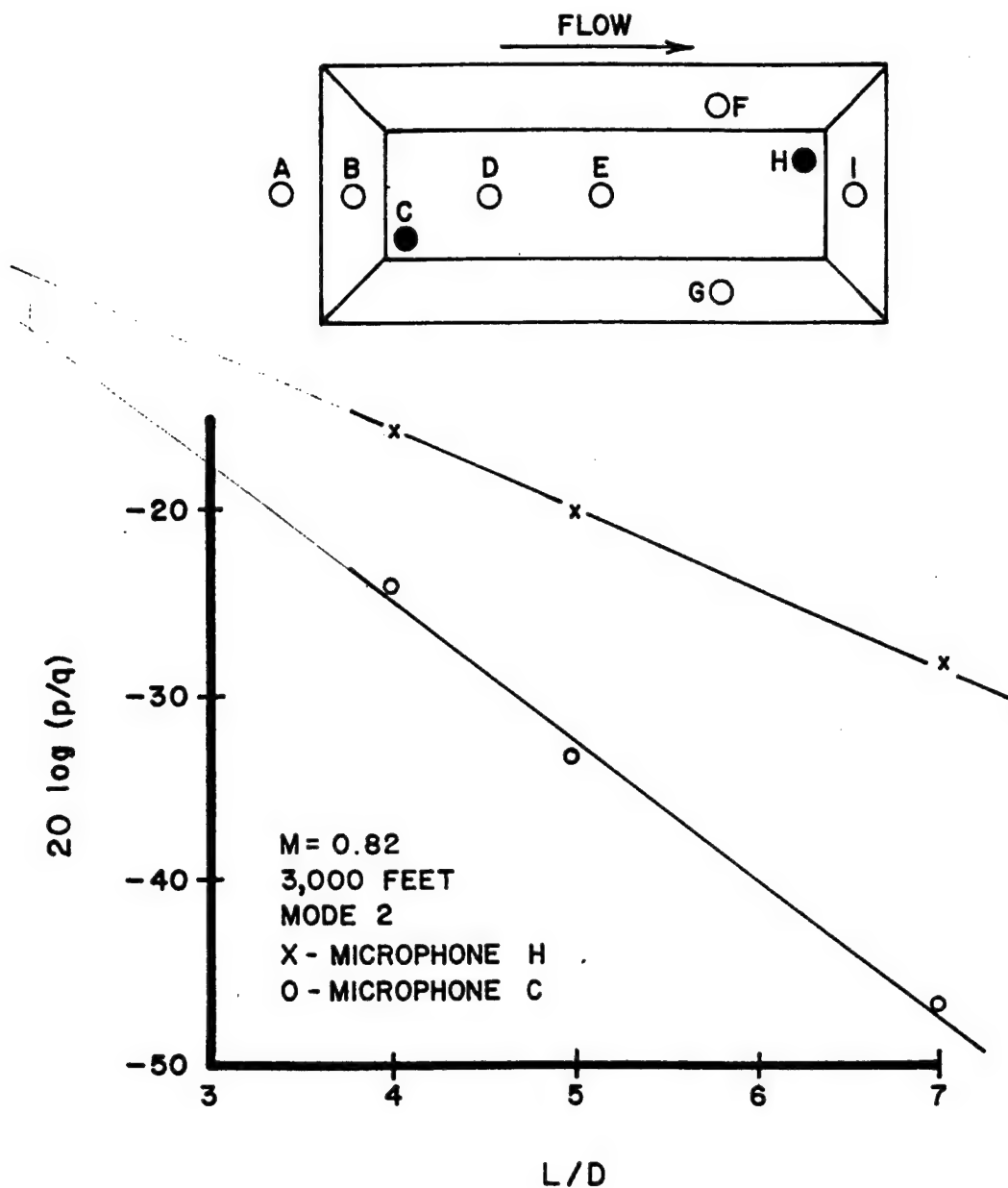


FIGURE 51 ONE-THIRD OCTAVE BAND PEAKS FROM MICROPHONES C AND H FOR 3,000 FEET ALTITUDE AND MACH = 0.82 DEPICTING L/D EFFECT

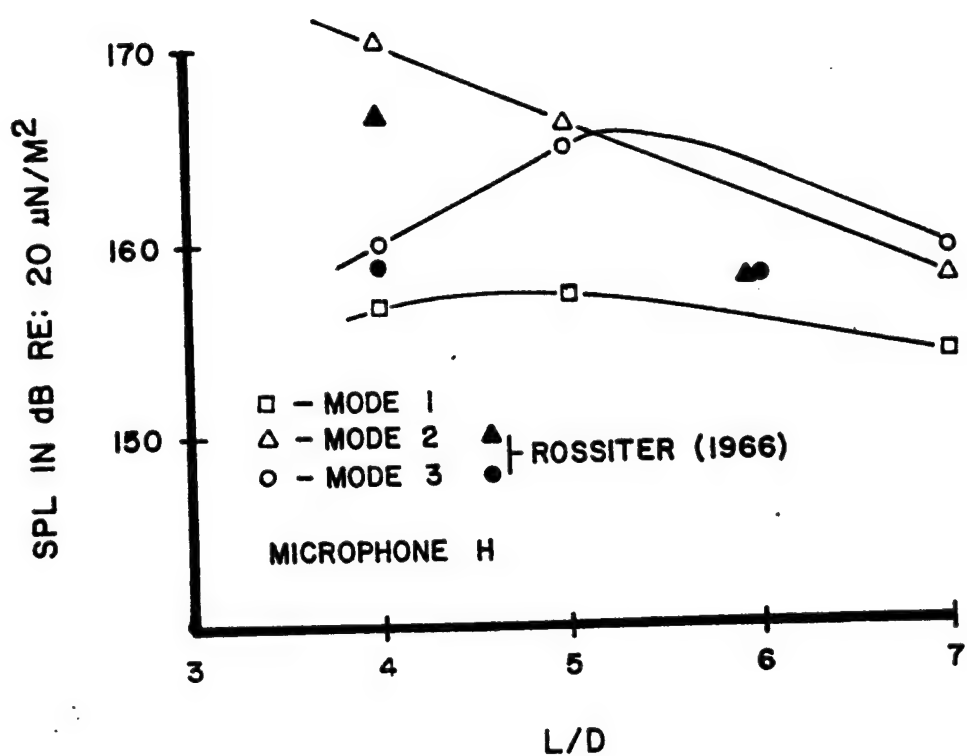
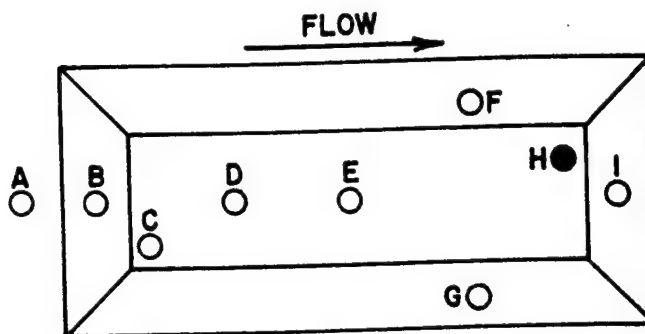


FIGURE 52 MAXIMUM ONE-THIRD OCTAVE BAND LEVEL AS A FUNCTION OF L/D FOR 3,000 FOOT ALTITUDE AND MACH 0.82

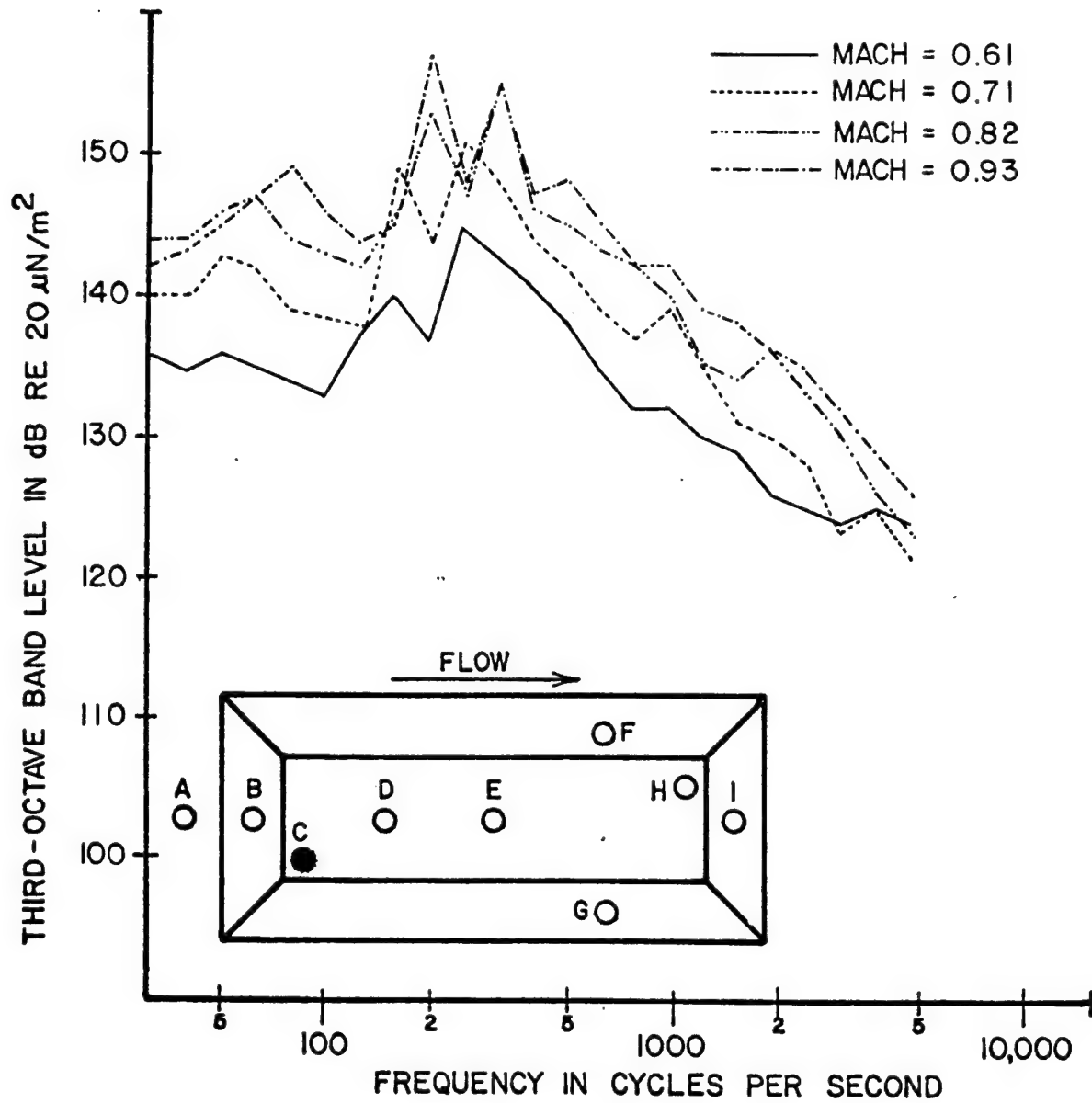


FIGURE 53 ONE-THIRD OCTAVE BAND SPECTRA FROM MICROPHONE C
AT AN ALTITUDE OF 3,000 FEET FOR $L/D = 5$

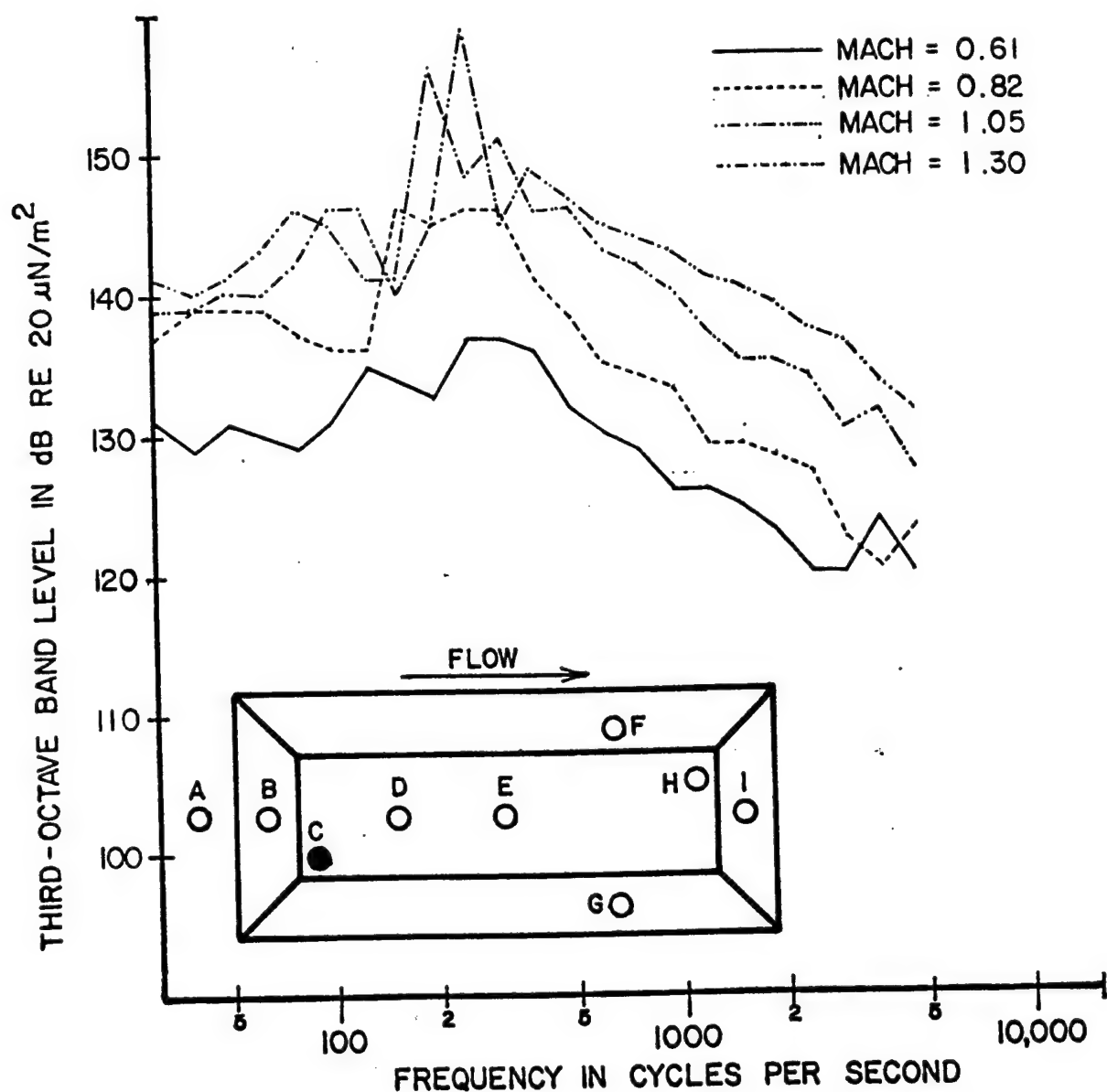


FIGURE 54 ONE-THIRD OCTAVE BAND SPECTRA FROM MICROPHONE C
AT AN ALTITUDE OF 20,000 FEET FOR L/D = 5

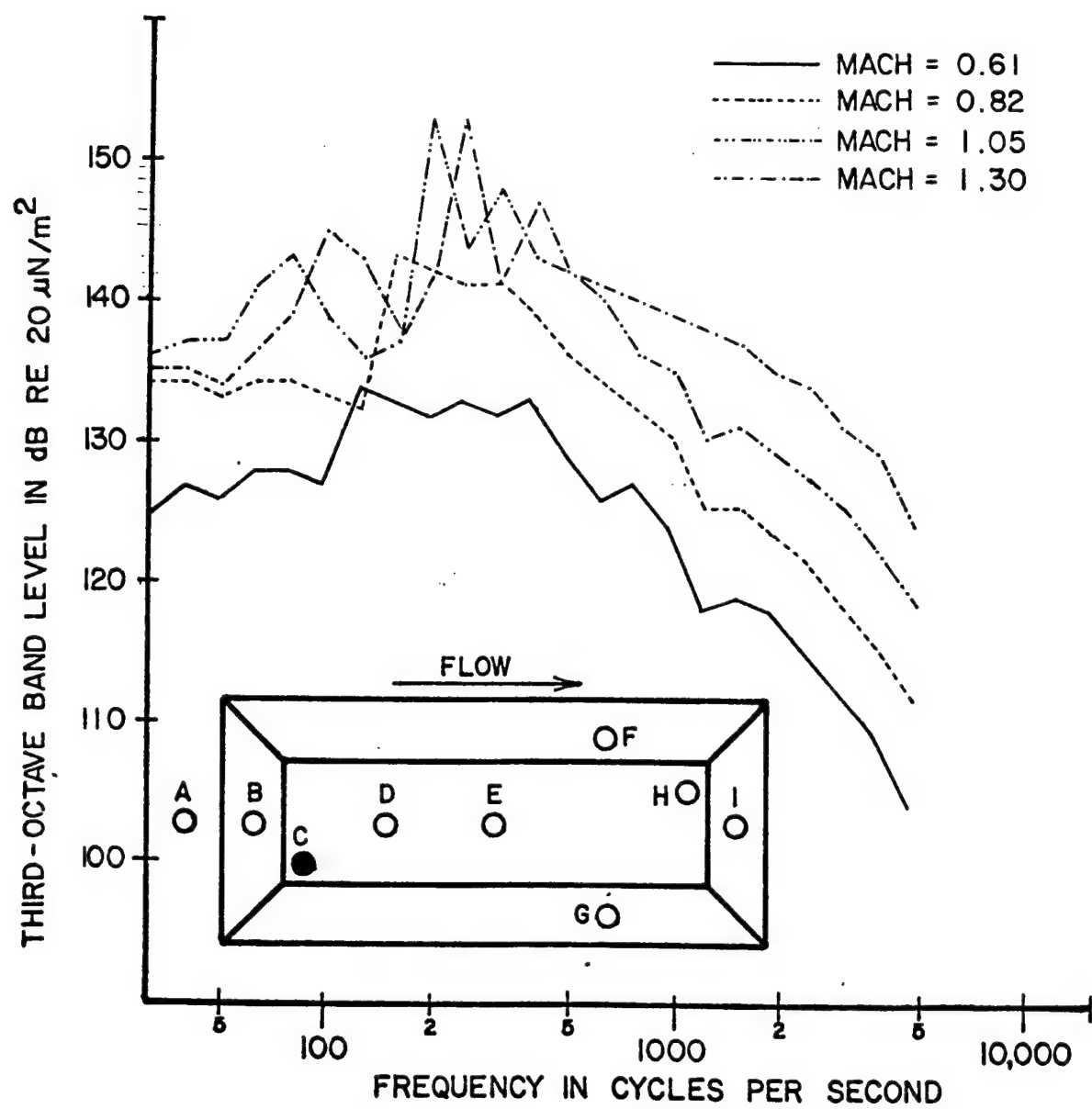


FIGURE 55 ONE-THIRD OCTAVE BAND SPECTRA FROM MICROPHONE C AT AN ALTITUDE OF 30,000 FEET FOR $L/D = 5$

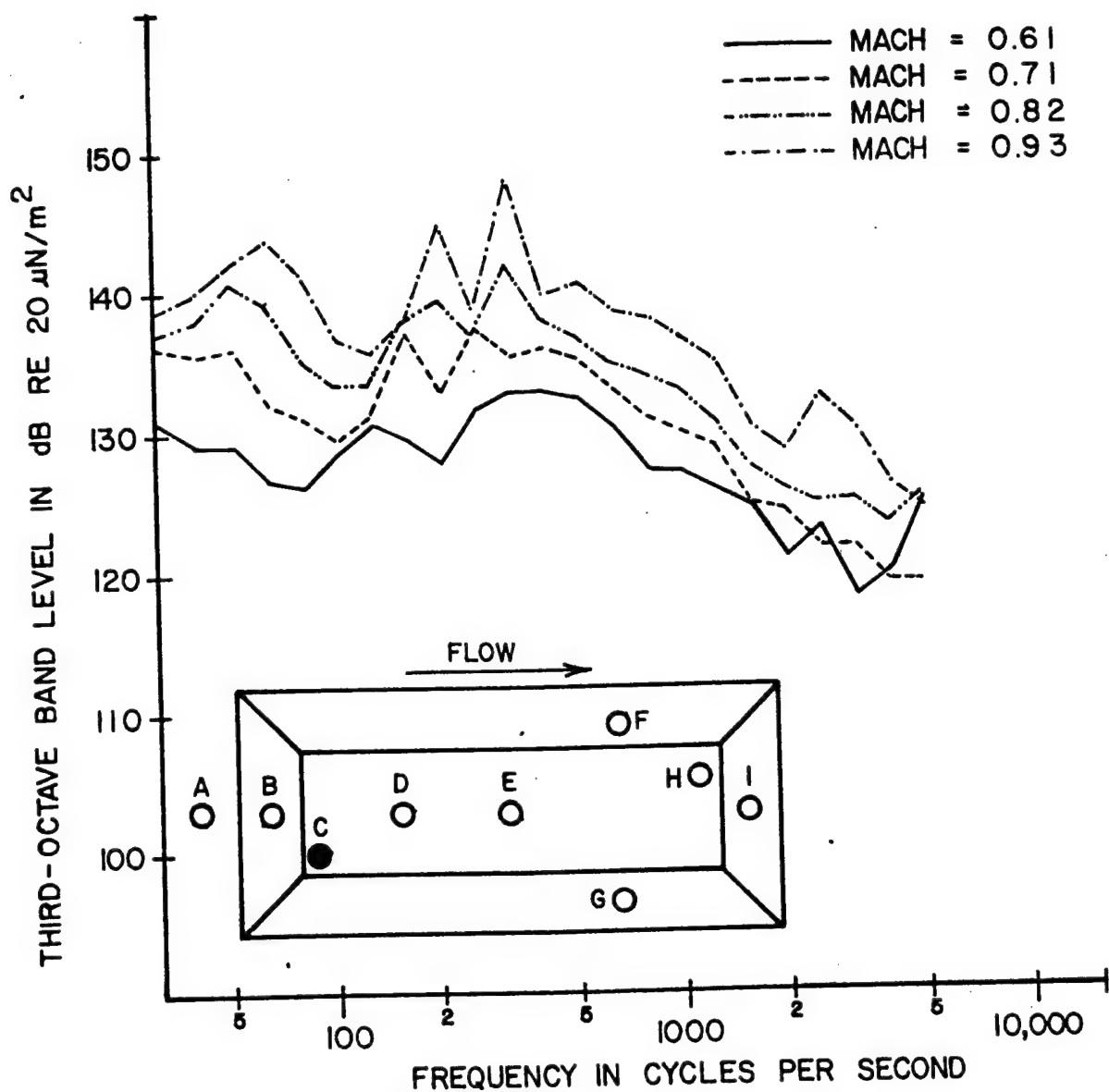


FIGURE 56 ONE-THIRD OCTAVE BAND SPECTRA FROM MICROPHONE C
AT AN ALTITUDE OF 3,000 FEET FOR $L/D = 7$

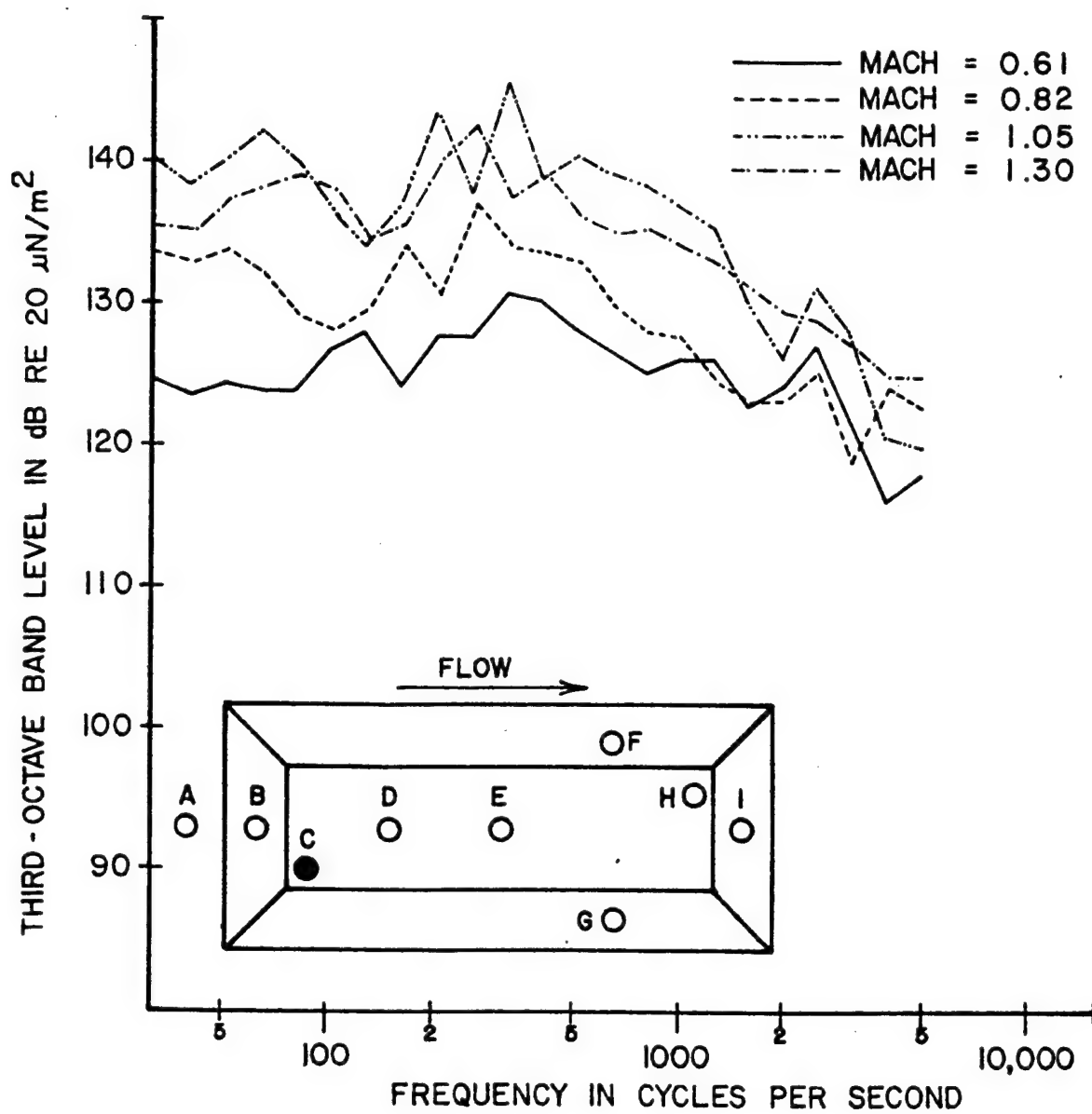


FIGURE 57 ONE-THIRD OCTAVE BAND SPECTRA FROM MICROPHONE C
AT AN ALTITUDE OF 20,000 FEET FOR $L/D = 7$

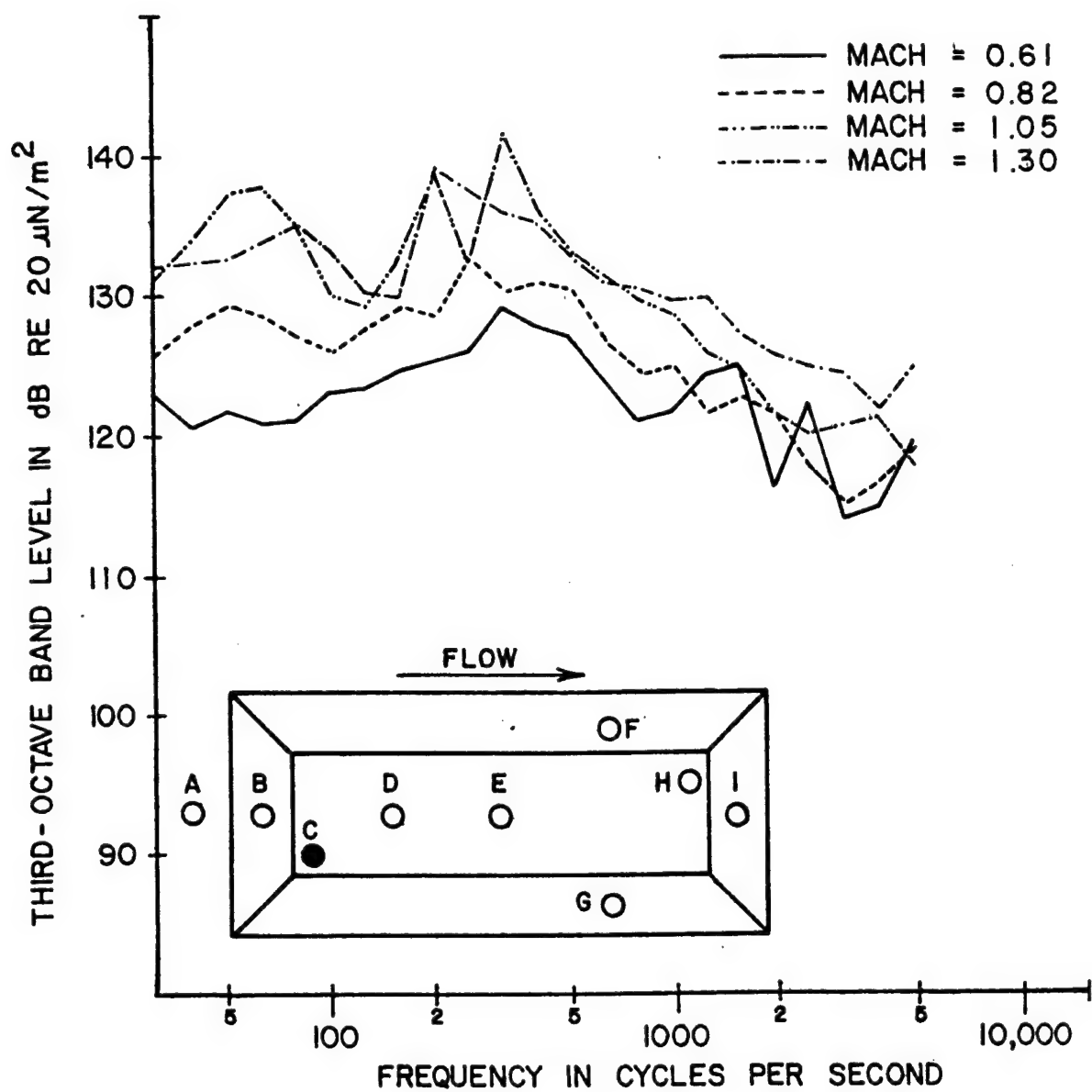


FIGURE 58 ONE-THIRD OCTAVE BAND SPECTRA FROM MICROPHONE C
AT AN ALTITUDE OF 30,000 FEET FOR $L/D = 7$

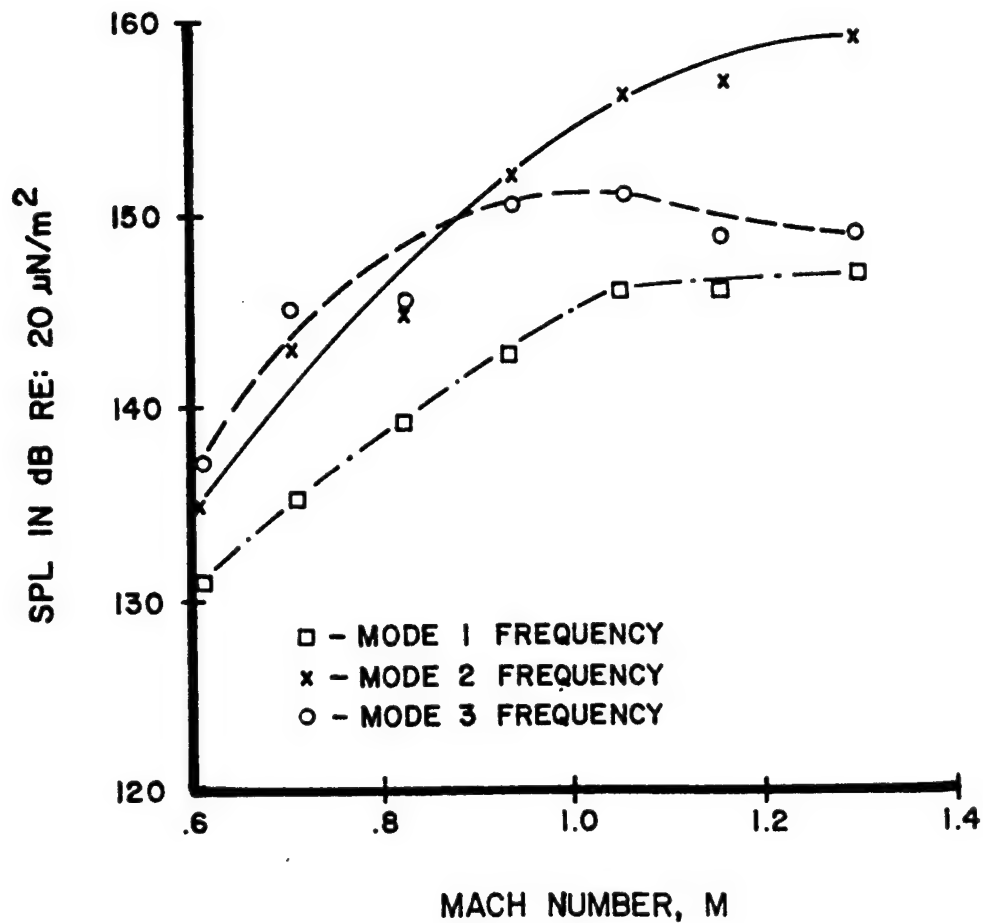


FIGURE 59 ONE-THIRD OCTAVE BAND SPECTRA DEPICTING MACH NUMBER EFFECT FROM MICROPHONE C FOR $L/D = 5$ AND 20,000 FOOT ALTITUDE

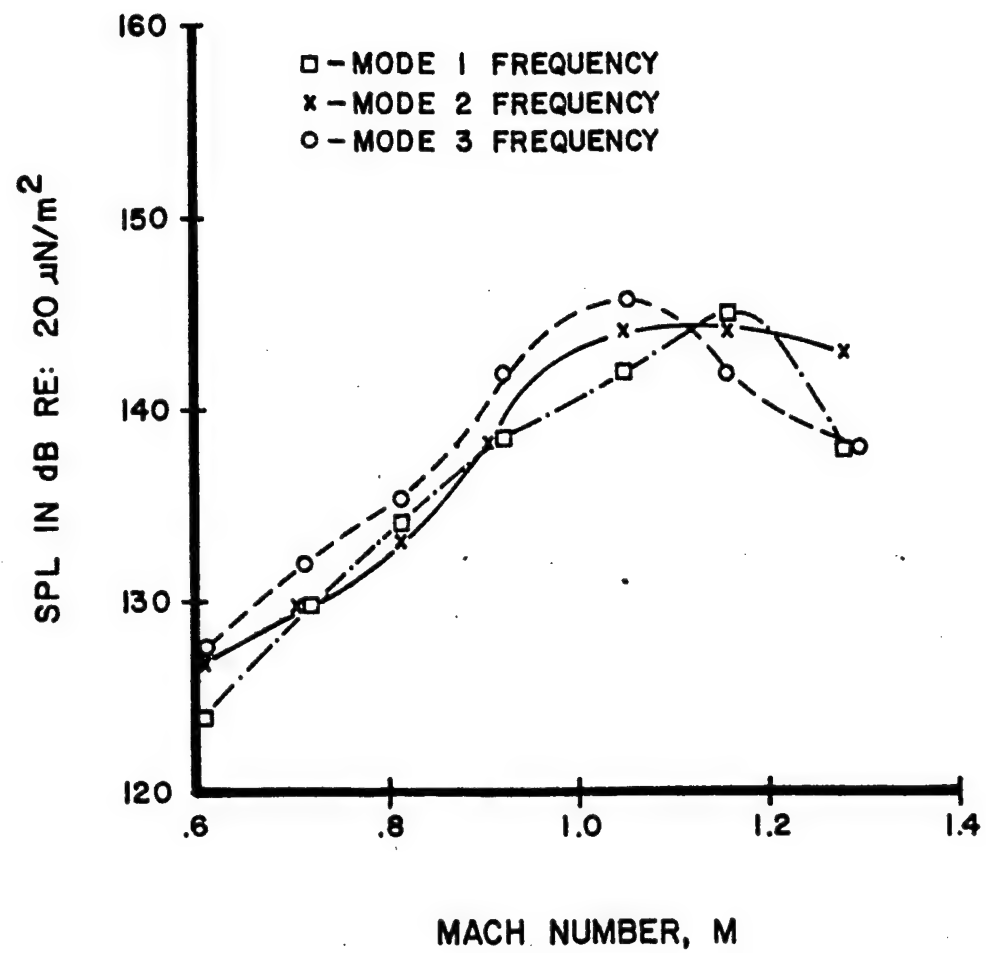


FIGURE 60 ONE-THIRD OCTAVE BAND SPECTRA DEPICTING MACH NUMBER EFFECT FROM MICROPHONE C FOR $L/D = 7$ AND 20,000 FOOT ALTITUDE

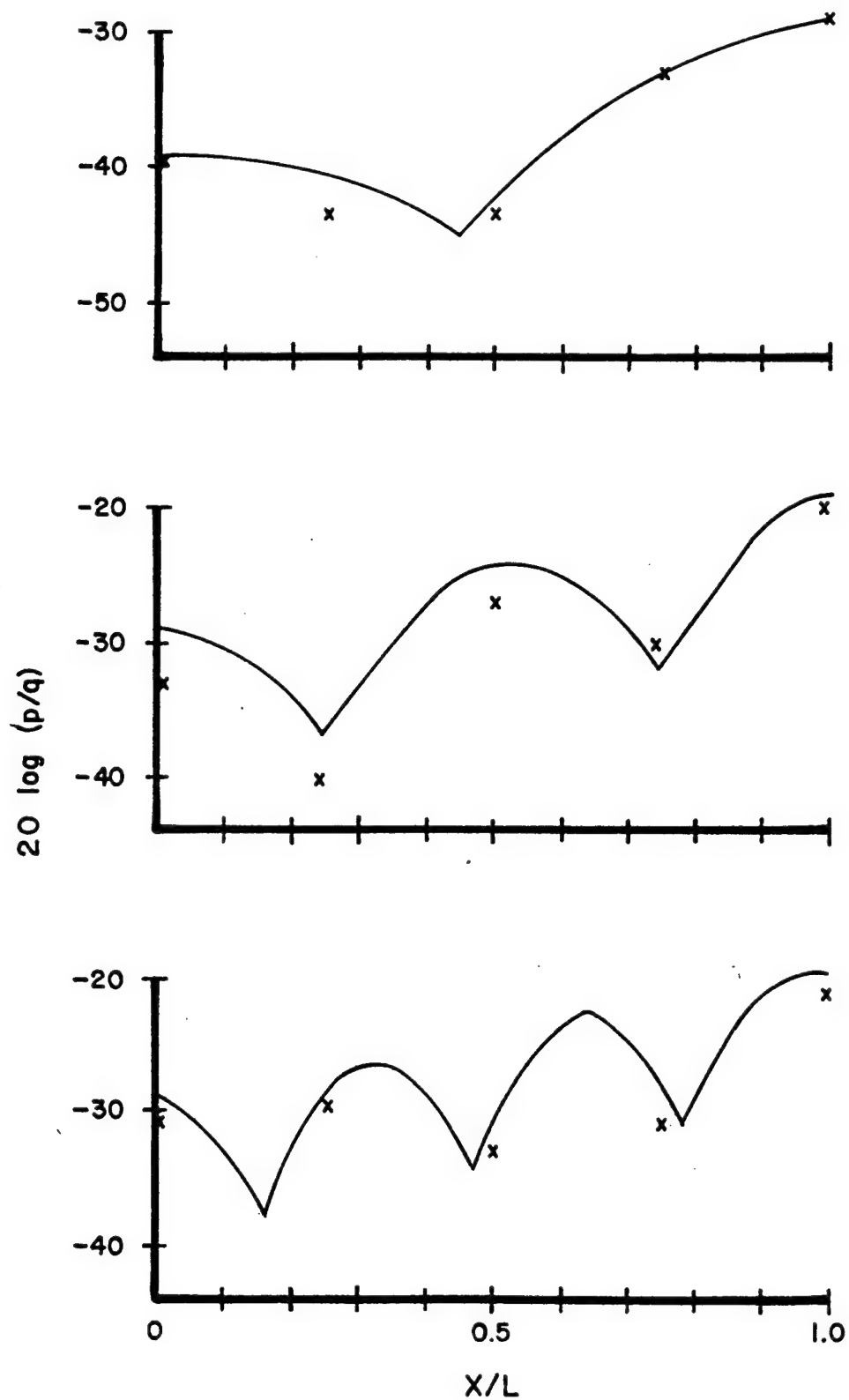


FIGURE 61 COMPARISON OF THE PREDICTION SCHEME WITH DATA FOR
 $L/D = 5$ FROM 3,000 FOOT ALTITUDE AND MACH 0.82

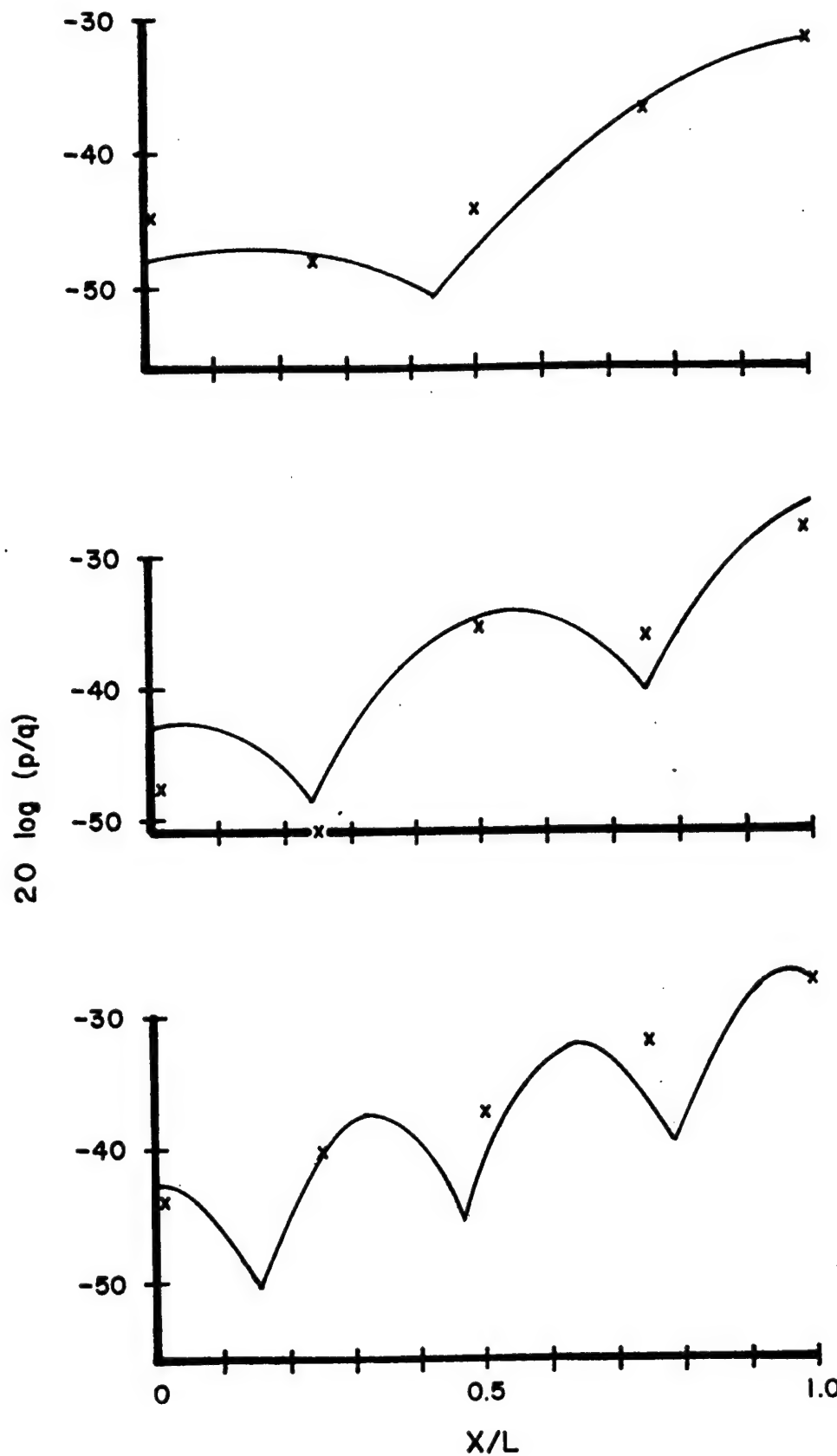


FIGURE 62 COMPARISON OF THE PREDICTION SCHEME WITH DATA FOR
 $L/D = 7$ FROM 3,000 FOOT ALTITUDE AND MACH 0.82

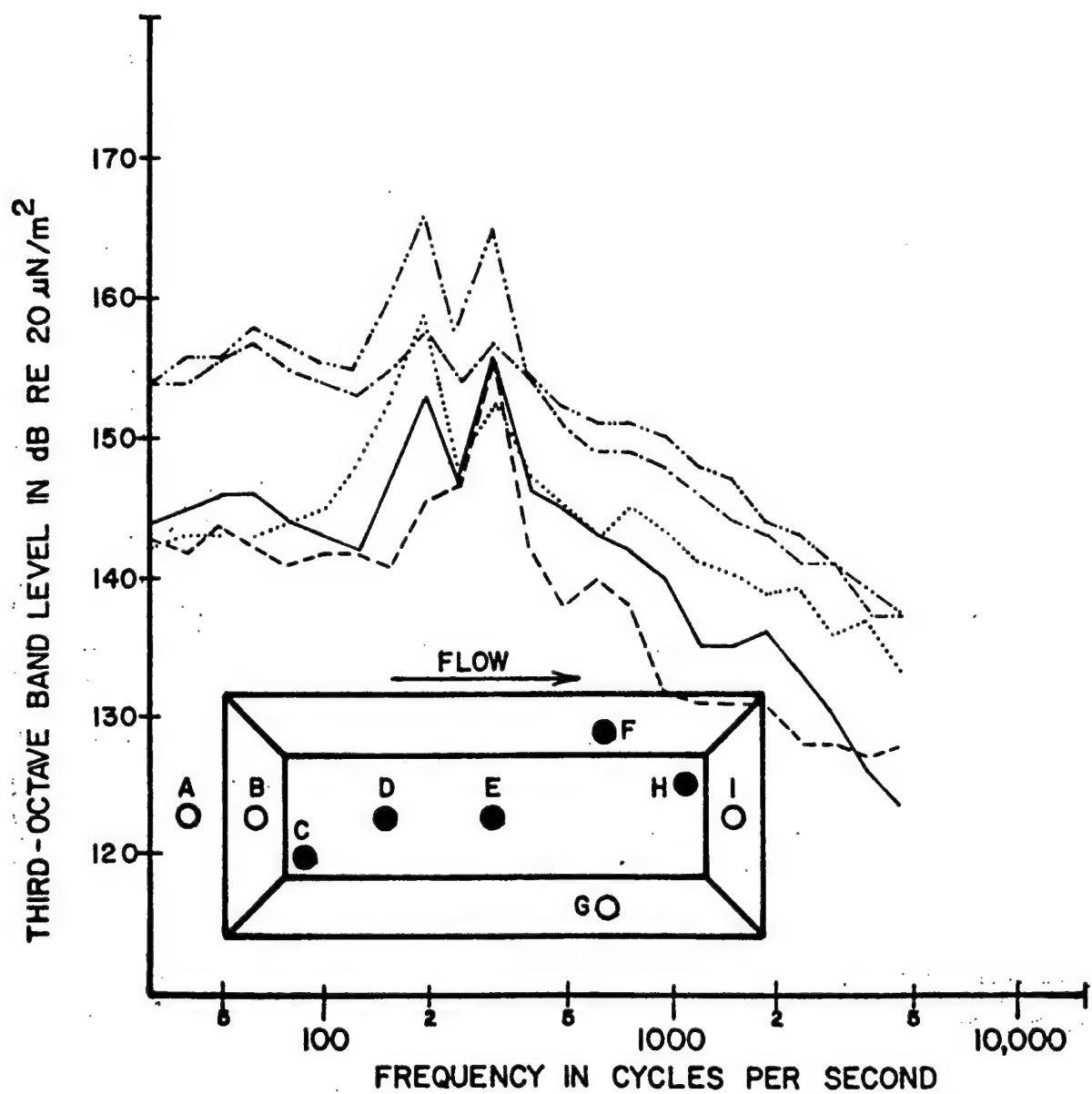
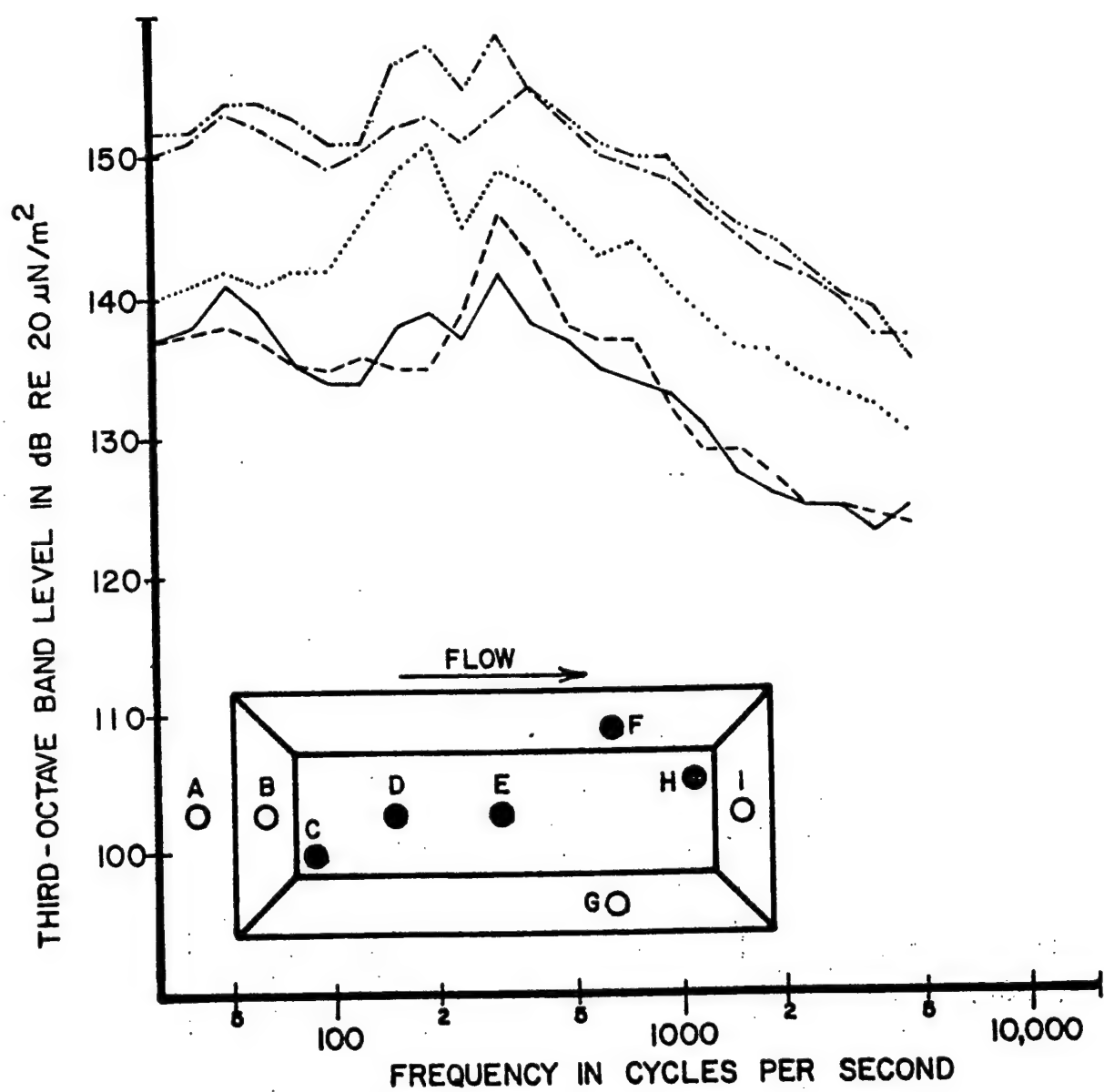


FIGURE 63 ONE-THIRD OCTAVE BAND SPECTRA FROM THE L/D = 5 CONFIGURATION DEPICTING LONGITUDINAL BROADBAND VARIATION



MICROPHONE C ———
 MICROPHONE D - - - - -
 MICROPHONE E
 MICROPHONE F - - - - -
 MICROPHONE H - - - - -

L/D = 7
 3000 FT. ALTITUDE
 MACH 0.82

FIGURE 64 ONE-THIRD OCTAVE BAND SPECTRA FROM THE L/D = 7
 CONFIGURATION DEPICTING LONGITUDINAL BROADBAND
 VARIATION

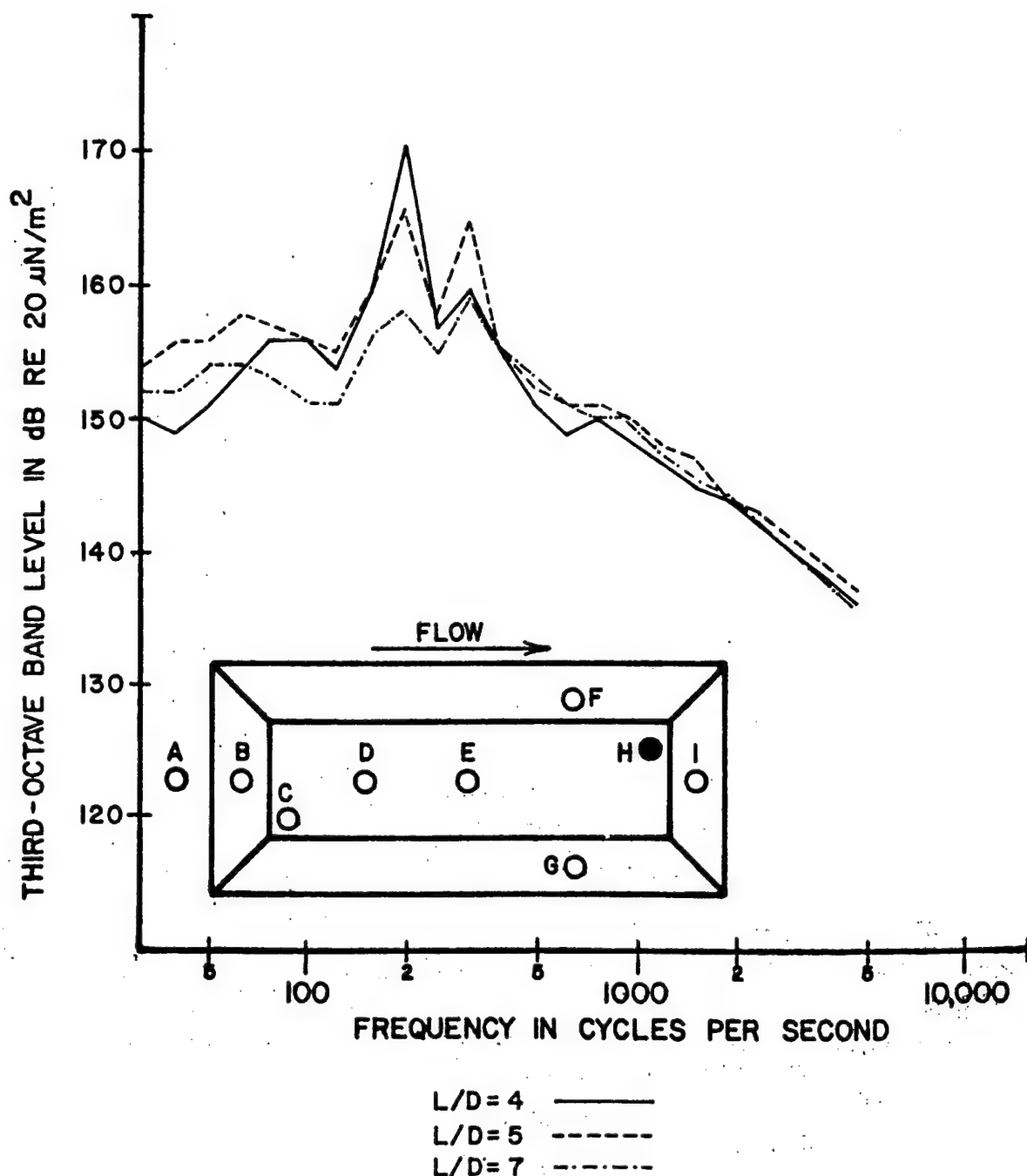


FIGURE 65 ONE-THIRD OCTAVE BAND SPECTRA FROM MICROPHONE H
FOR A MACH NUMBER OF 0.82 DEPICTING L/D EFFORT

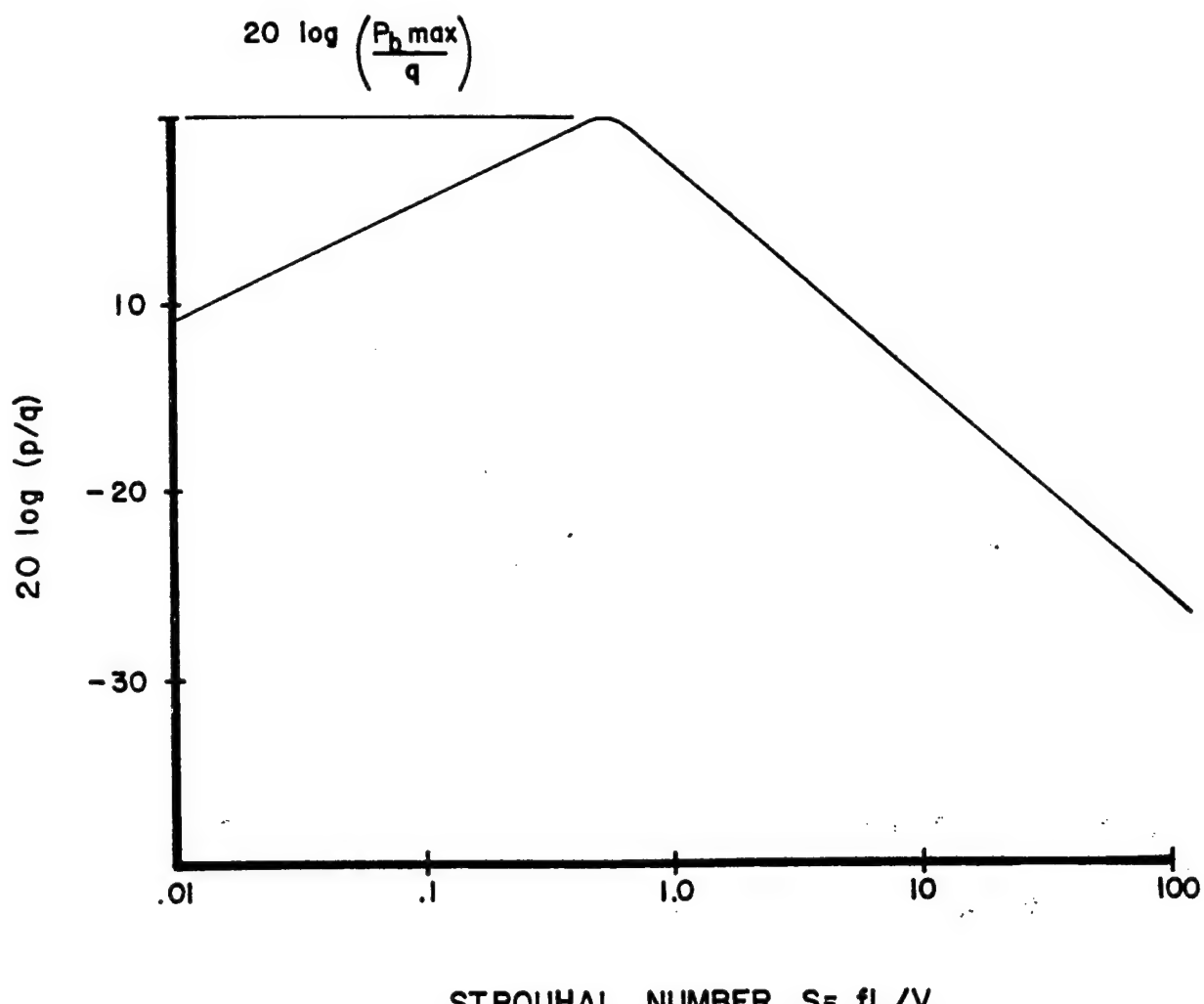


FIGURE 66 BROADBAND LEVEL VERSUS STROUHAL NUMBER

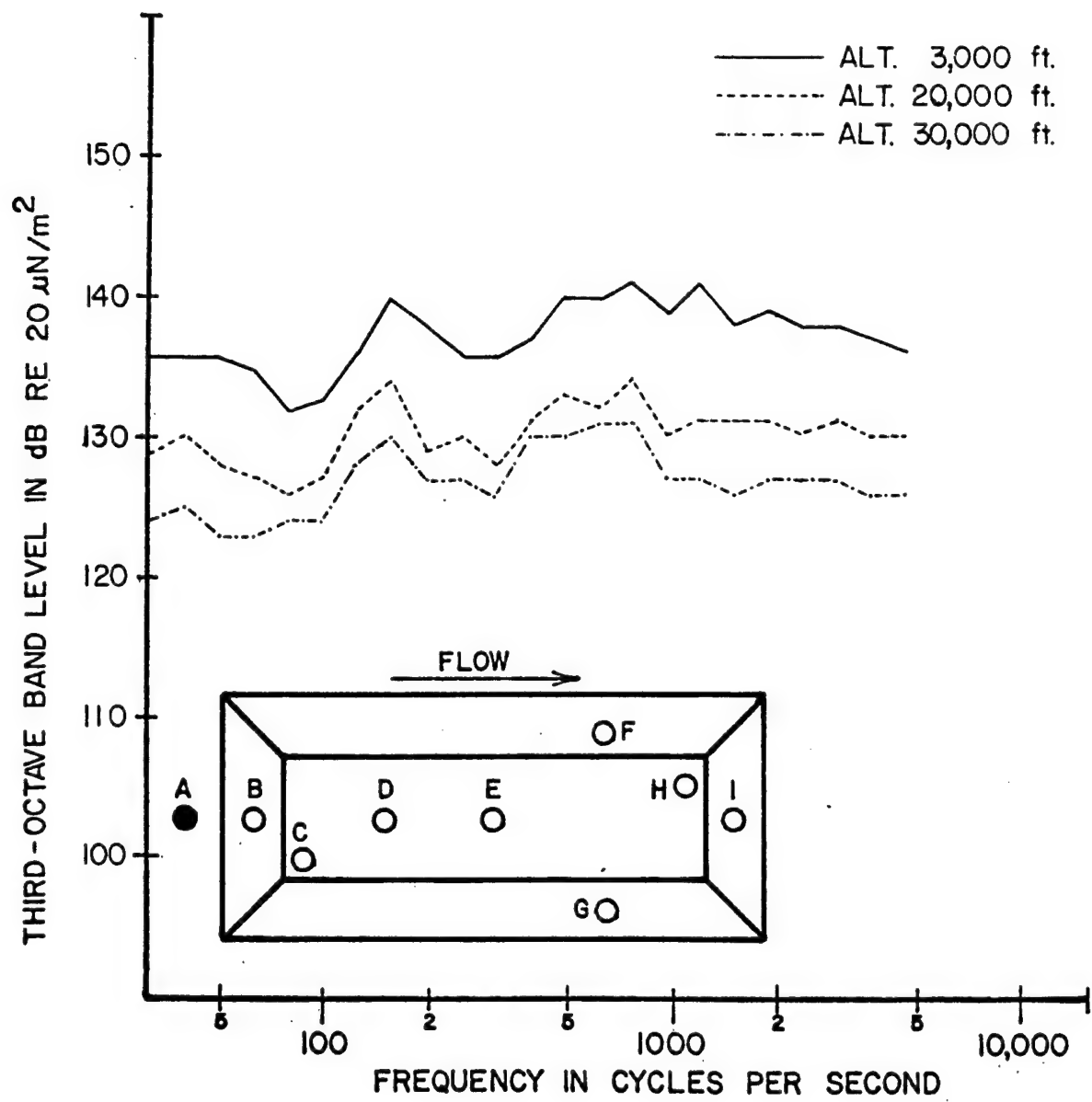


FIGURE 67 ONE-THIRD OCTAVE BAND SPECTRA FROM MICROPHONE A OF THE
 $L/D = 7$ WITH STORE CONFIGURATION AT A MACH NUMBER OF 0.82

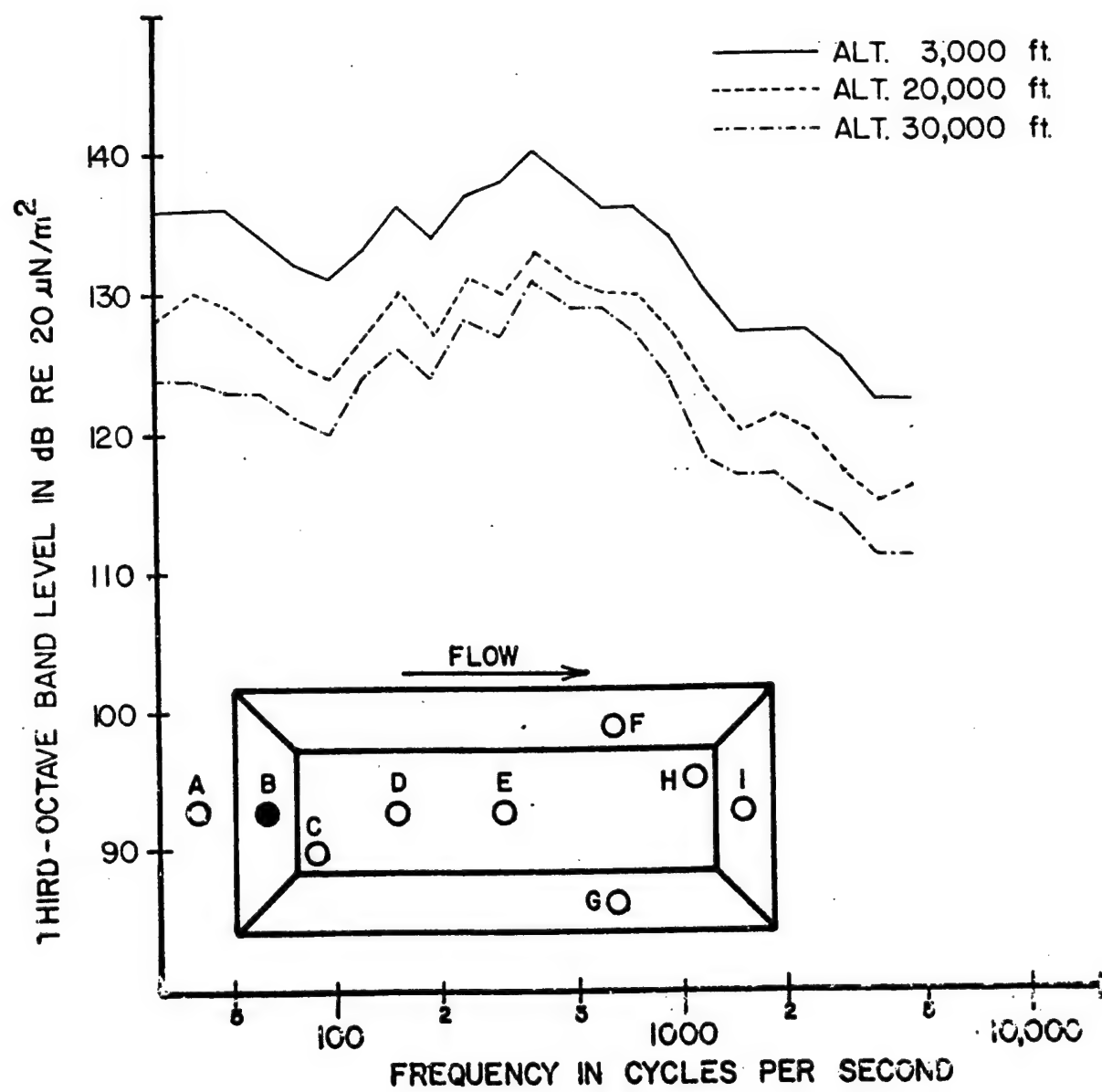


FIGURE 68 ONE-THIRD OCTAVE BAND SPECTRA FROM MICROPHONE B OF THE
 $L/D = 7$ WITH STORE CONFIGURATION AT A MACH NUMBER OF 0.82

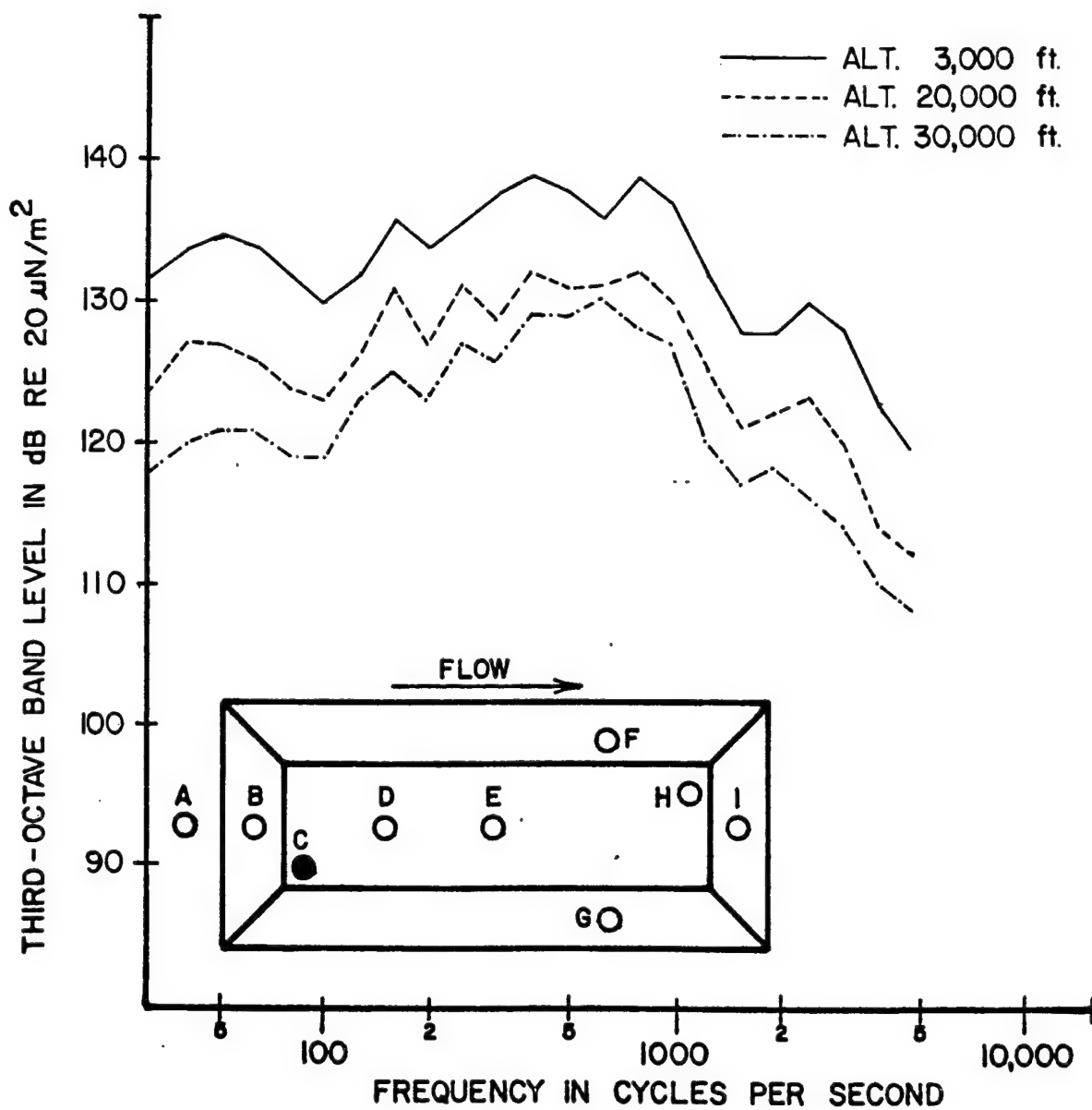


FIGURE 69 ONE-THIRD OCTAVE BAND SPECTRA FROM MICROPHONE C OF THE L/D = 7 WITH STORE CONFIGURATION AT A MACH NUMBER OF 0.82

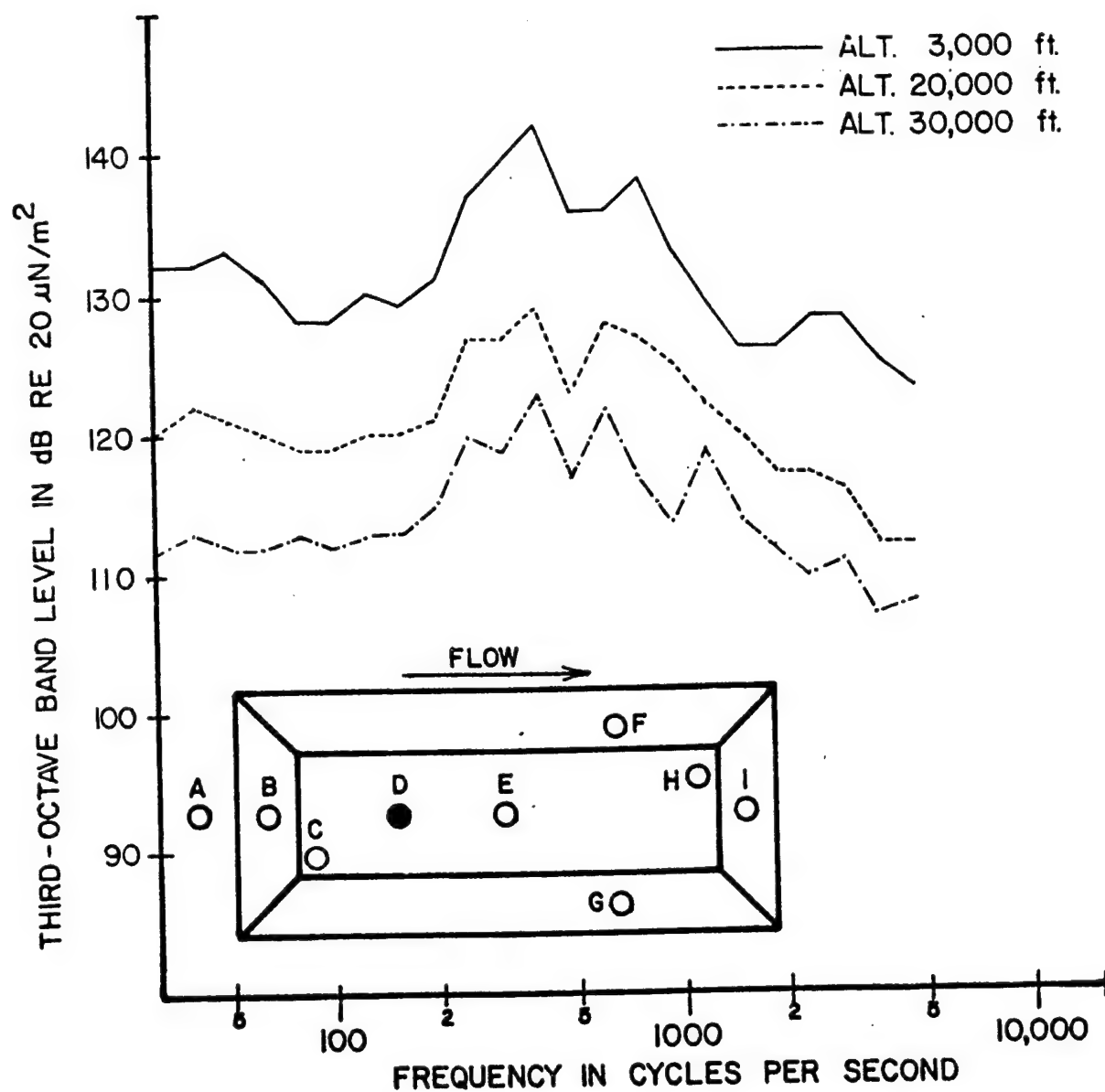


FIGURE 70 ONE-THIRD OCTAVE BAND SPECTRA FROM MICROPHONE D OF THE
 $L/D = 7$ WITH STORE CONFIGURATION AT A MACH NUMBER OF 0.82

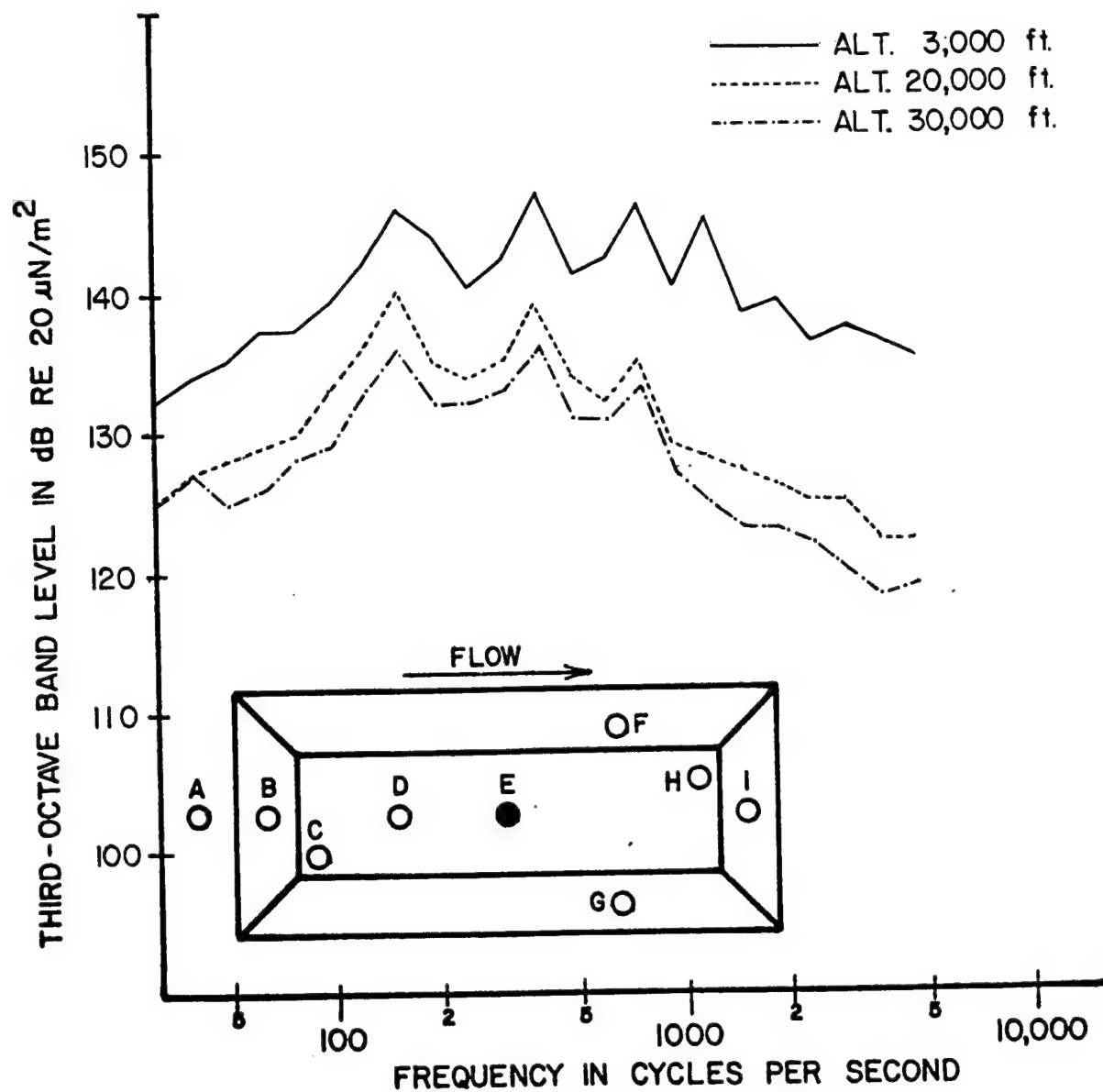


FIGURE 71 ONE-THIRD OCTAVE BAND SPECTRA FROM MICROPHONE E OF THE
 $L/D = 7$ WITH STORE CONFIGURATION AT A MACH NUMBER OF 0.82

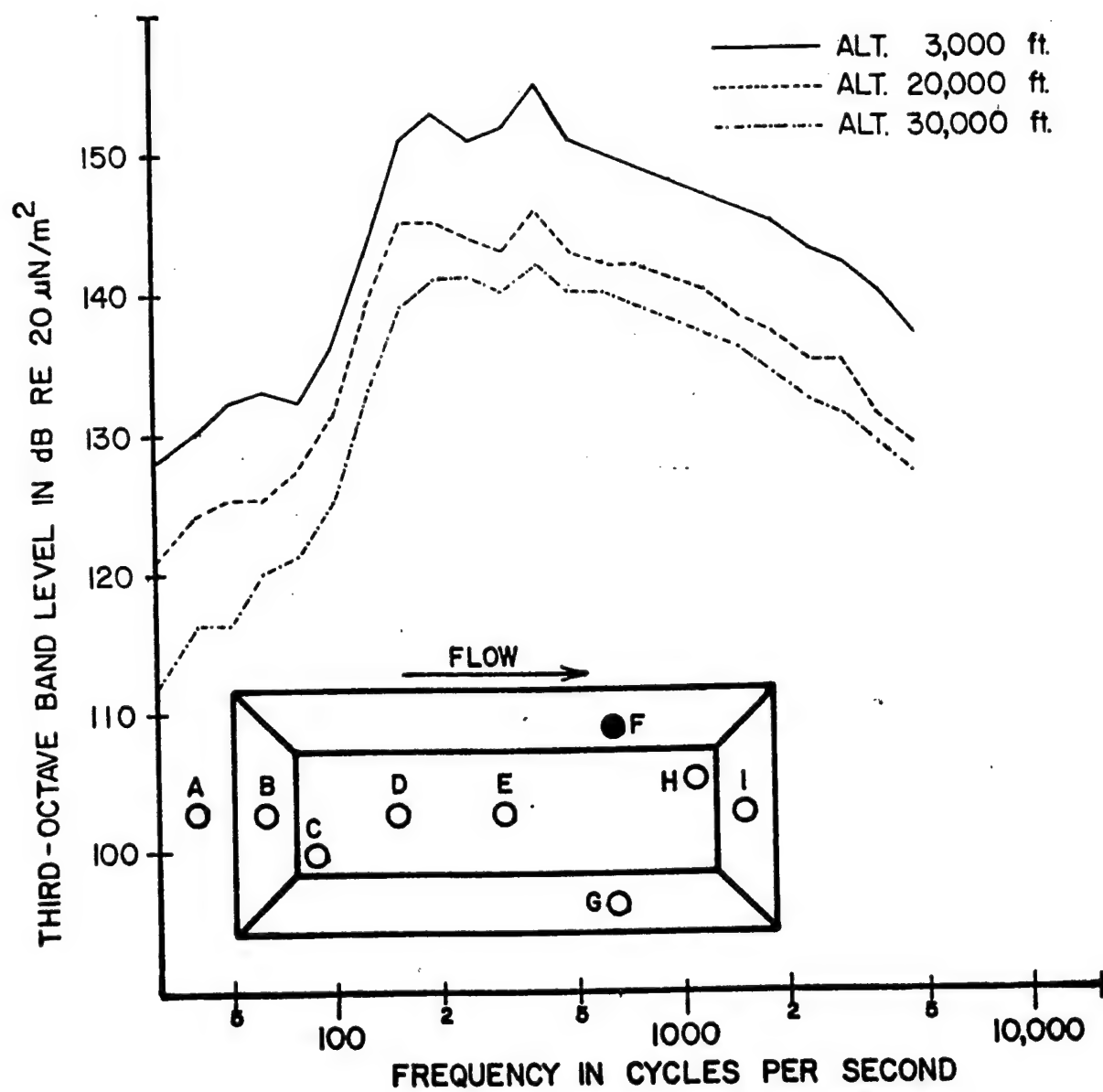


FIGURE 72 ONE-THIRD OCTAVE BAND SPECTRA FROM MICROPHONE F OF THE
L/D = 7 WITH STORE CONFIGURATION AT A MACH NUMBER OF 0.82

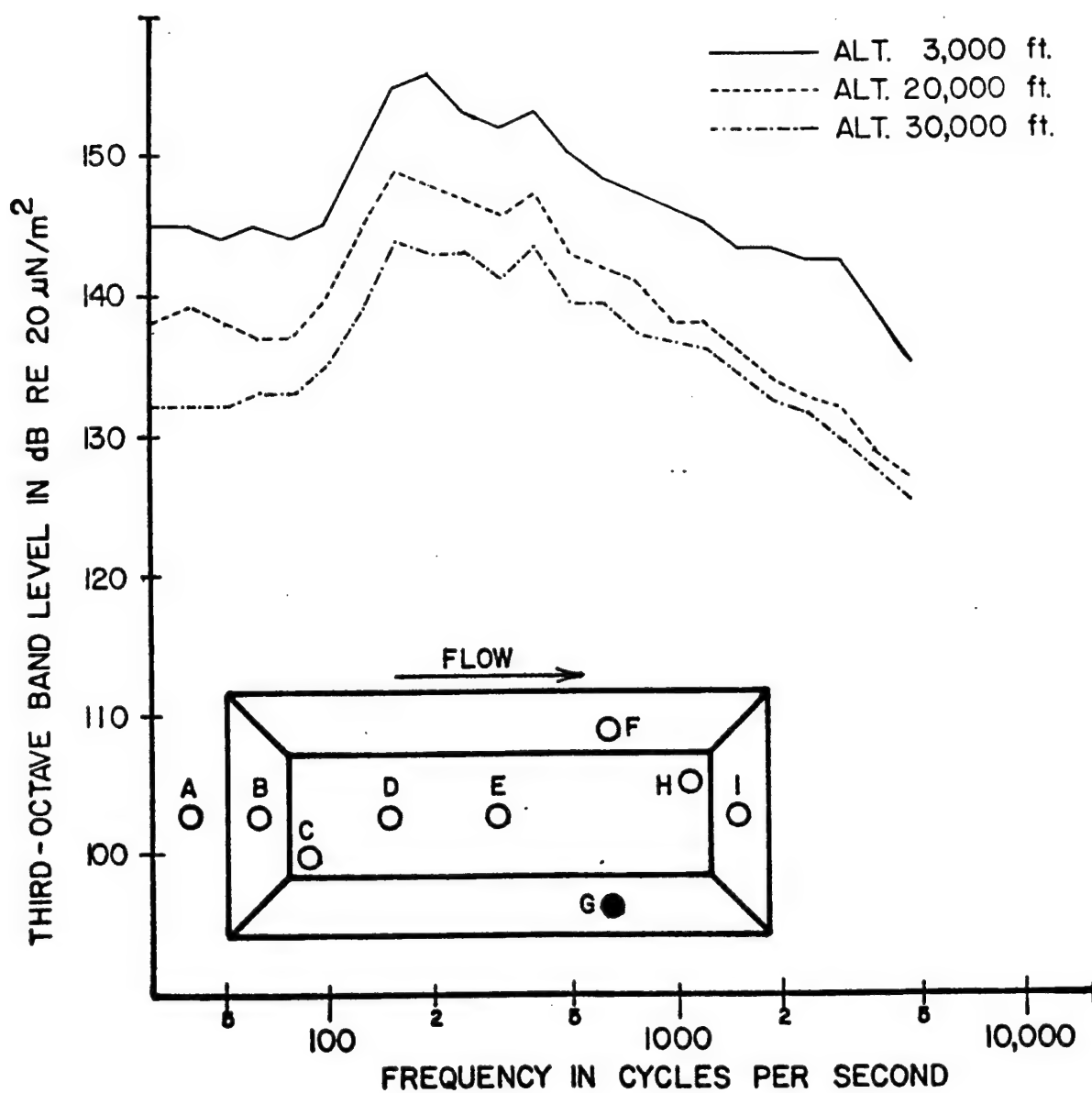


FIGURE 73 ONE-THIRD OCTAVE BAND SPECTRA FROM MICROPHONE G OF THE L/D = 7 WITH STORE CONFIGURATION AT A MACH NUMBER OF 0.82

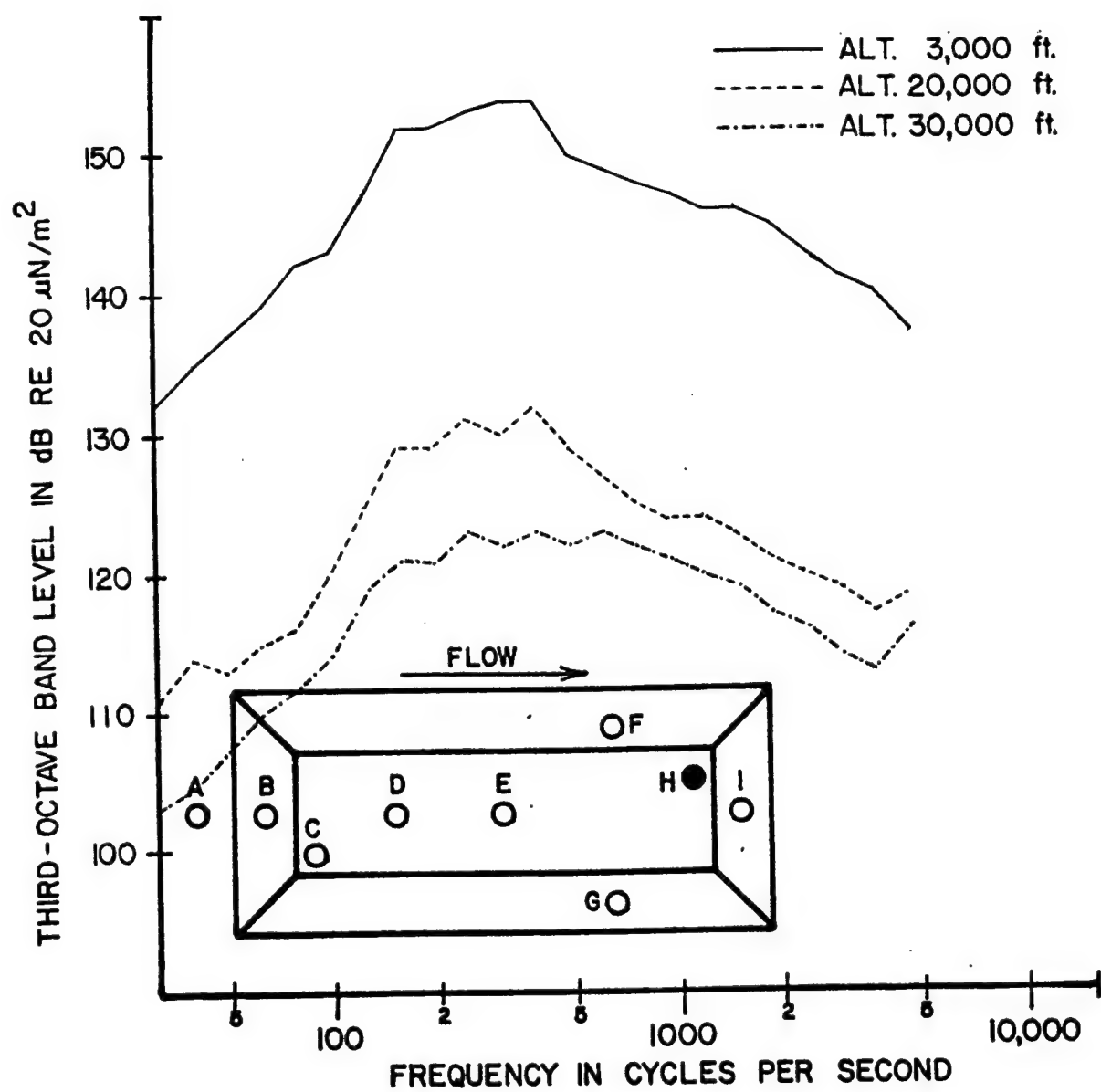


FIGURE 74 ONE-THIRD OCTAVE BAND SPECTRA FROM MICROPHONE H OF THE L/D = 7 WITH STORE CONFIGURATION AT A MACH NUMBER OF 0.82

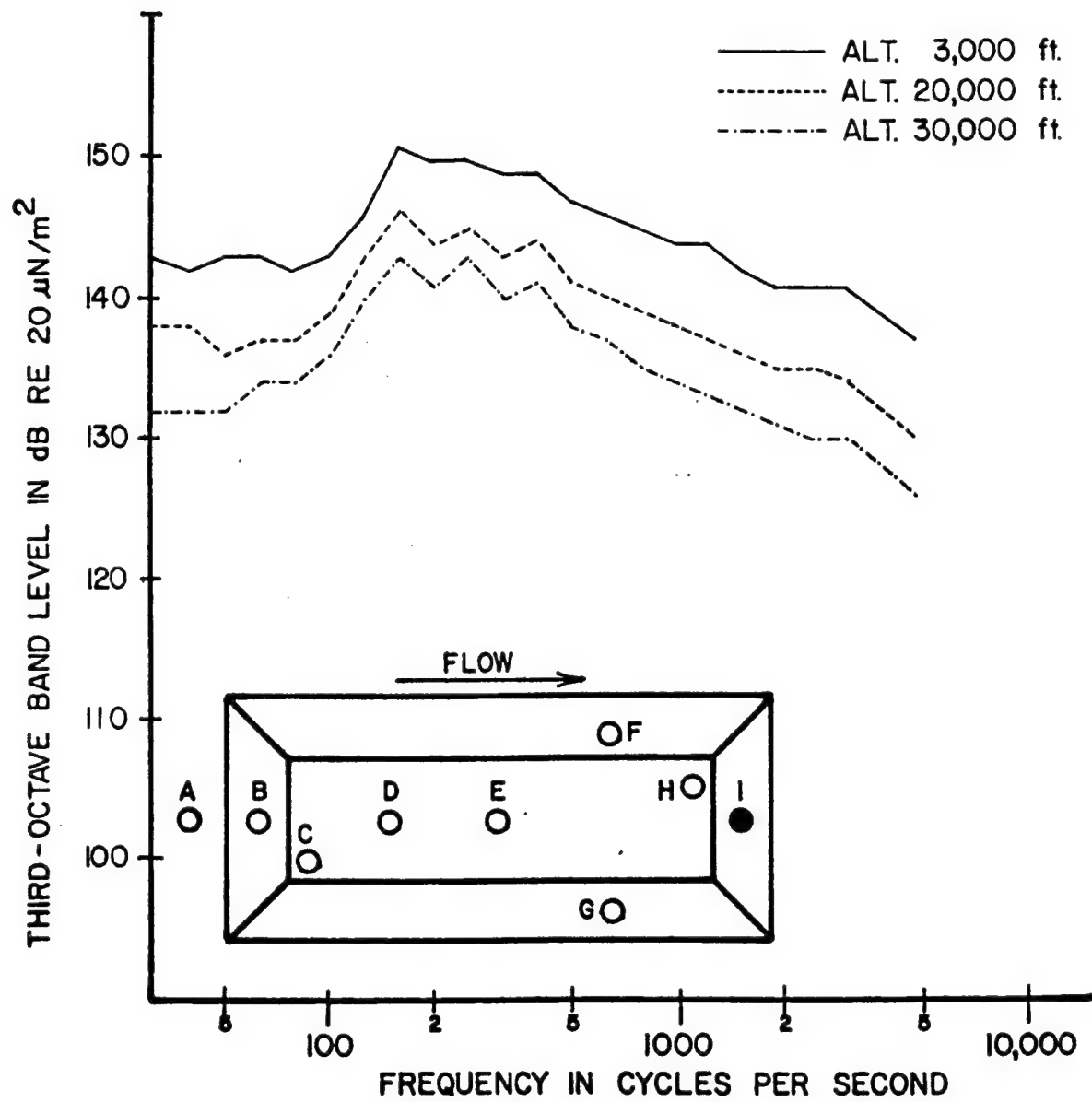


FIGURE 75 ONE-THIRD OCTAVE BAND SPECTRA FROM MICROPHONE I OF THE
 $L/D = 7$ WITH STORE CONFIGURATION AT A MACH NUMBER OF 0.82

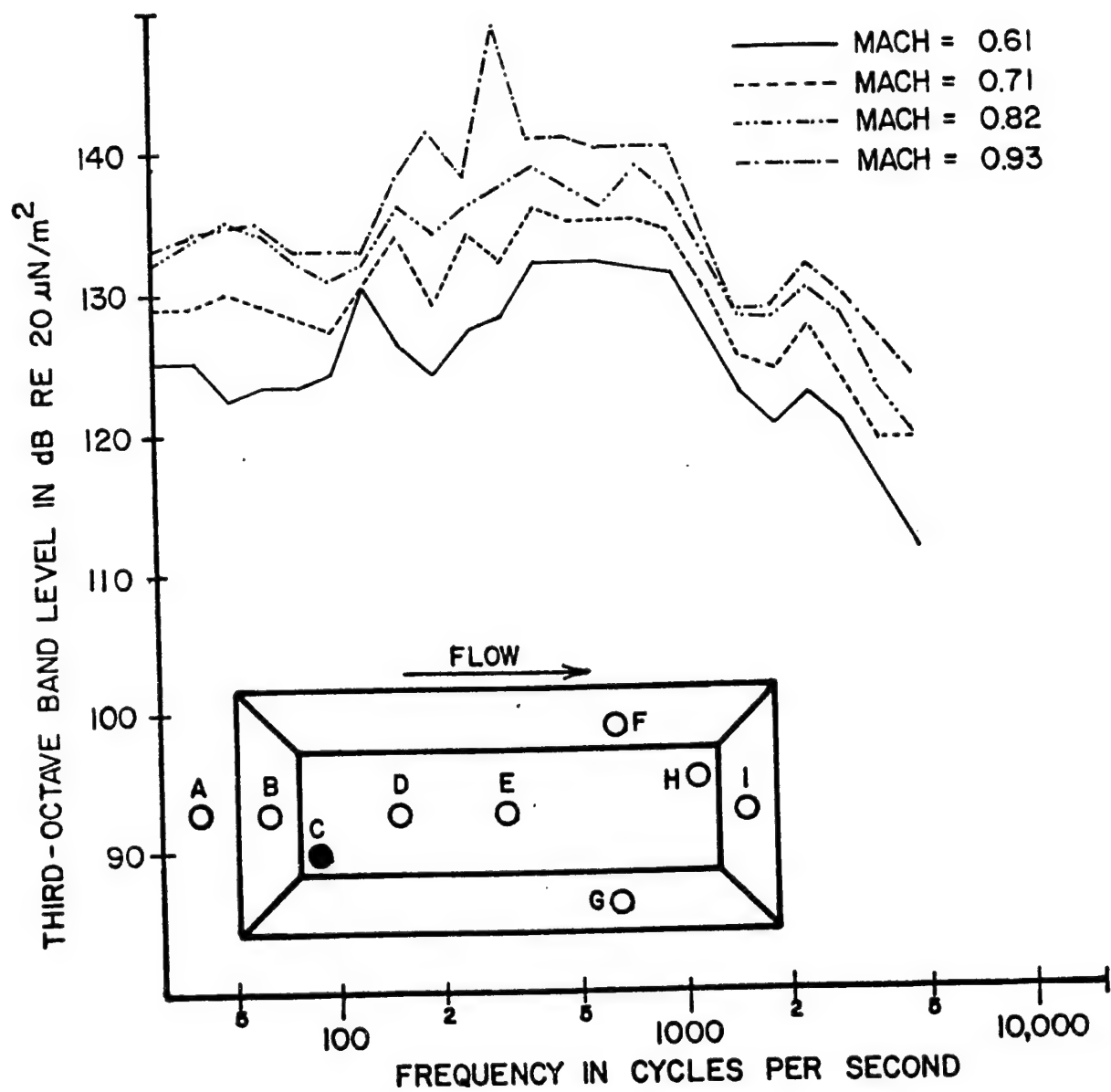


FIGURE 76 ONE-THIRD OCTAVE BAND SPECTRA FROM MICROPHONE C OF THE
 $L/D = 7$ WITH STORE CONFIGURATION FOR AN ALTITUDE OF 3,000 FEET

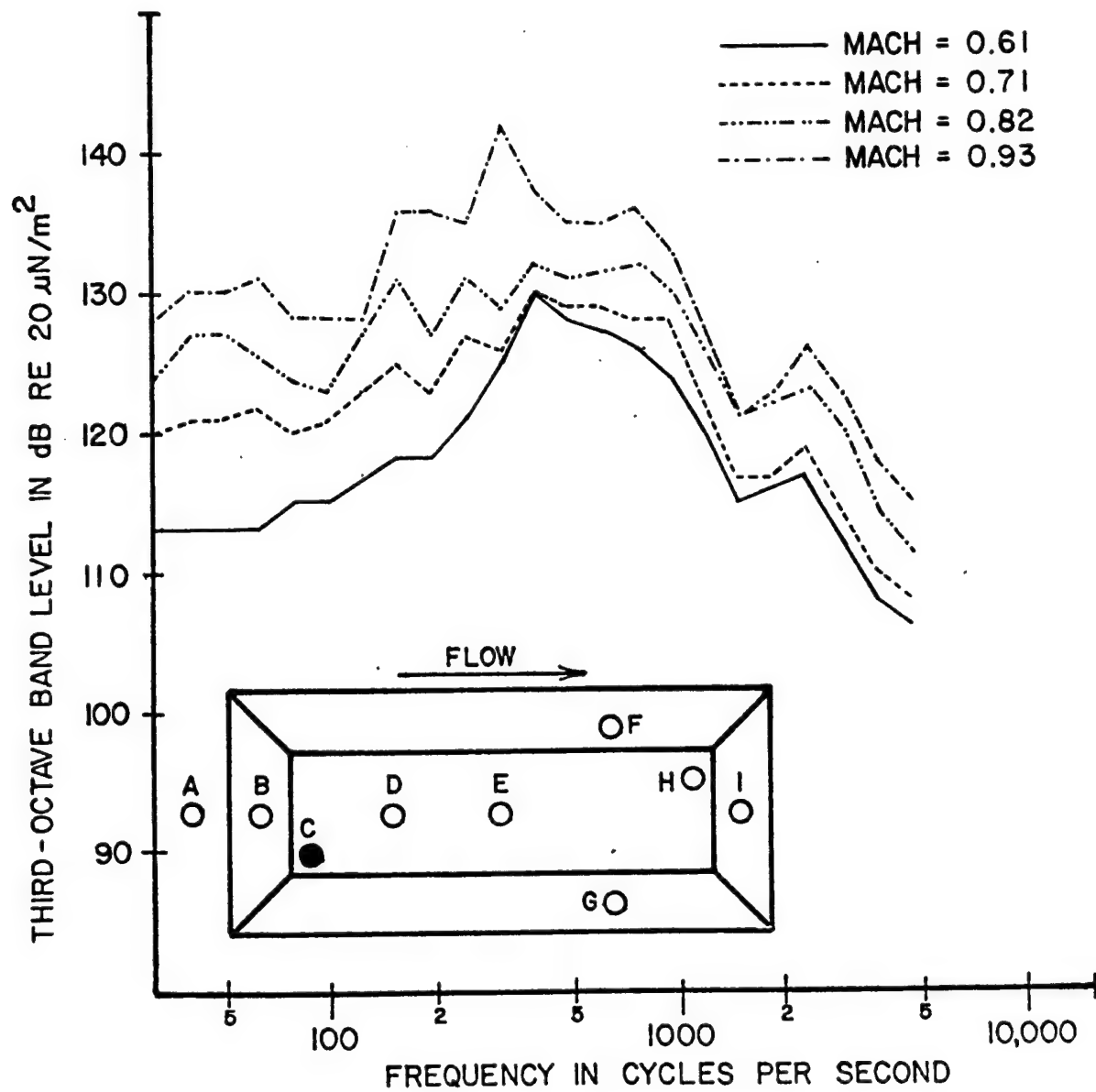


FIGURE 77 ONE-THIRD OCTAVE BAND SPECTRA FROM MICROPHONE C OF THE L/D = 7 WITH STORE CONFIGURATION FOR AN ALTITUDE OF 20,000 FEET

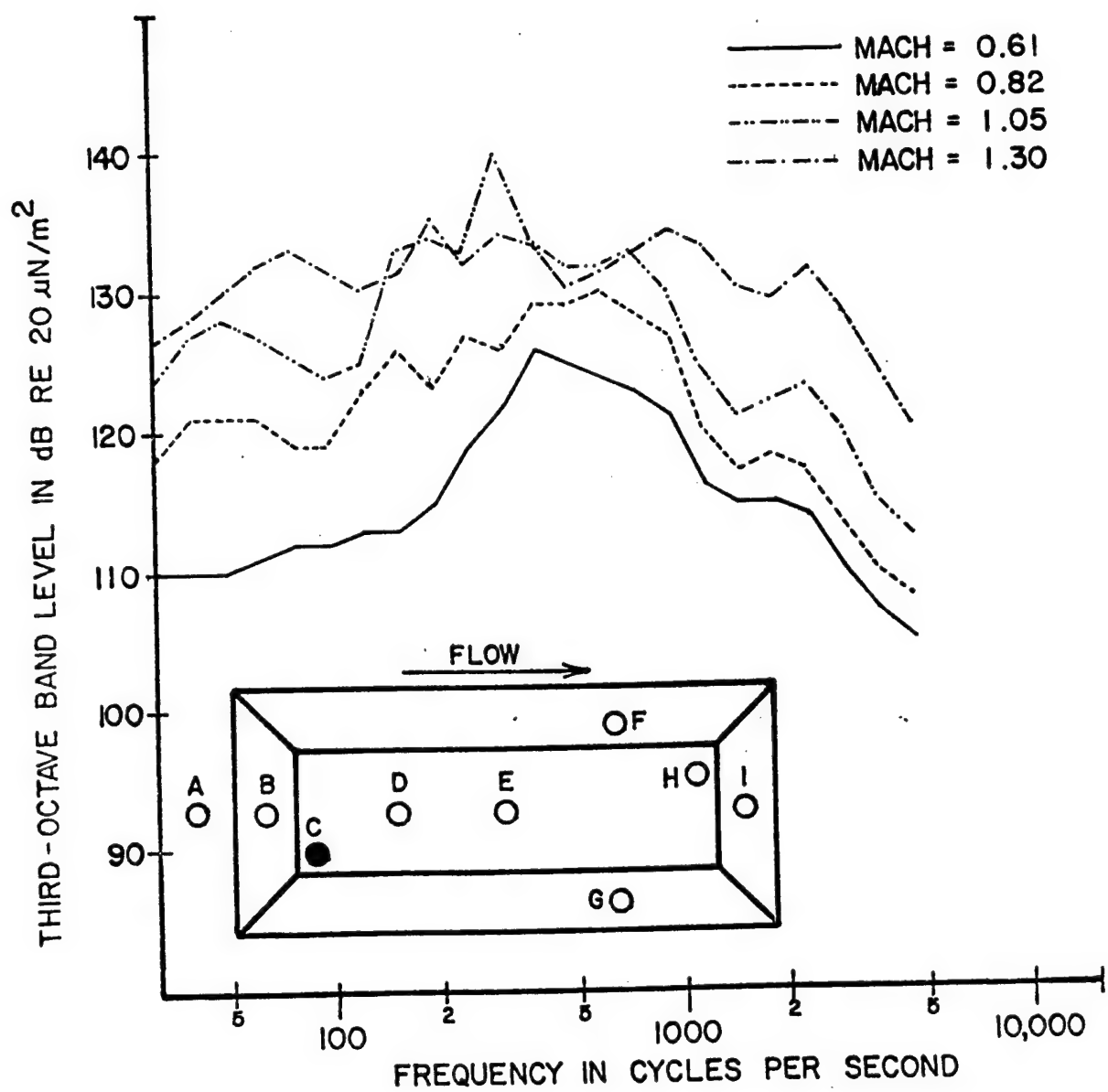


FIGURE 78 ONE-THIRD OCTAVE BAND SPECTRA FROM MICROPHONE C OF THE
 $L/D = 7$ WITH STORE CONFIGURATION FOR AN ALTITUDE OF 30,000 FEET

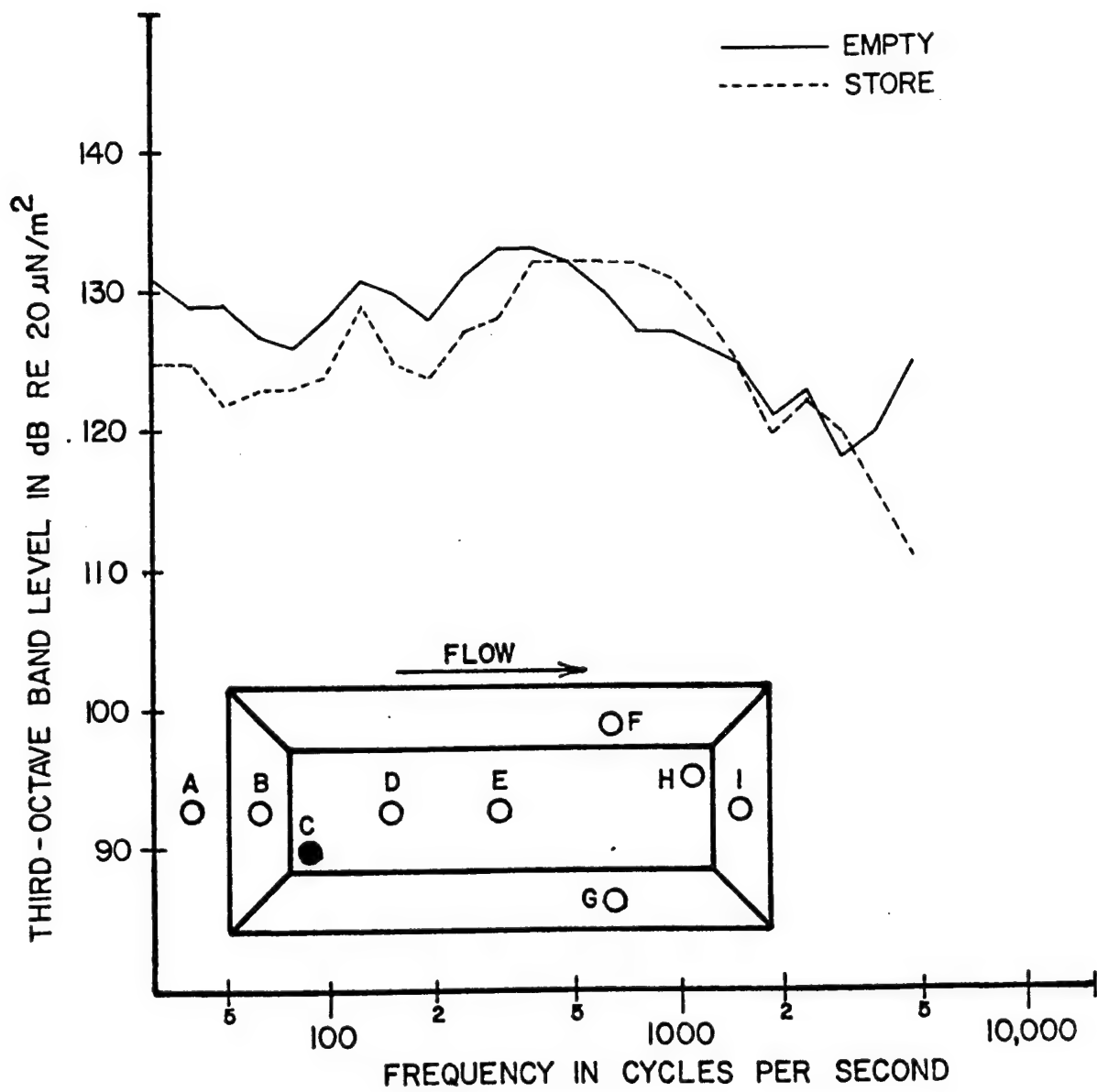


FIGURE 79 COMPARISON OF THE ONE-THIRD OCTAVE BAND SPECTRA FROM THE $L/D = 7$ EMPTY AND STORE CONFIGURATION FOR A MACH NUMBER OF 0.61 AND ALTITUDE OF 3,000 FEET

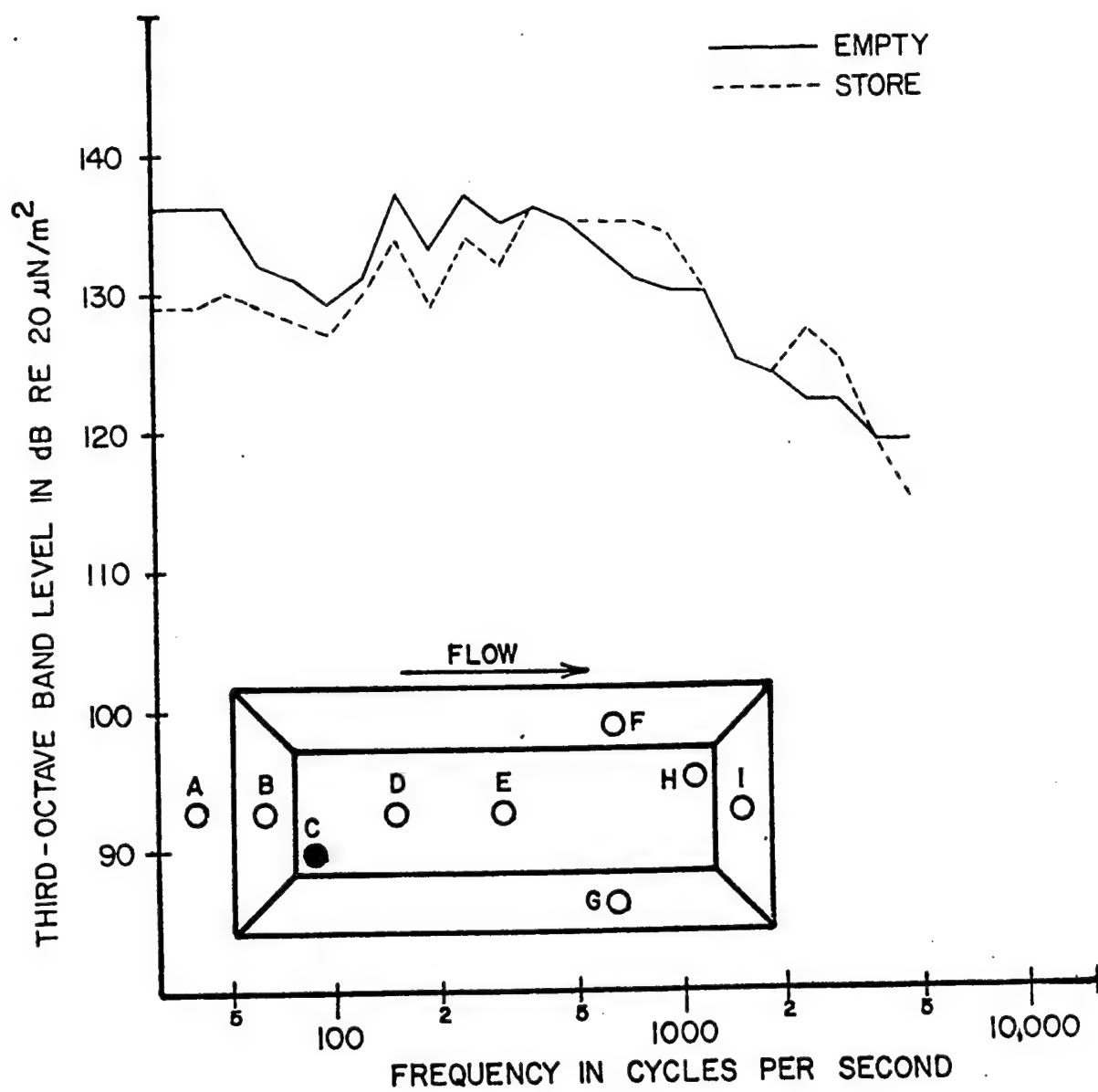


FIGURE 80 COMPARISON OF ONE-THIRD OCTAVE BAND SPECTRA FROM THE
 $L/D = 7$ EMPTY AND STORE CONFIGURATION FOR A MACH NUMBER
 OF 0.71 AND ALTITUDE OF 3,000 FEET

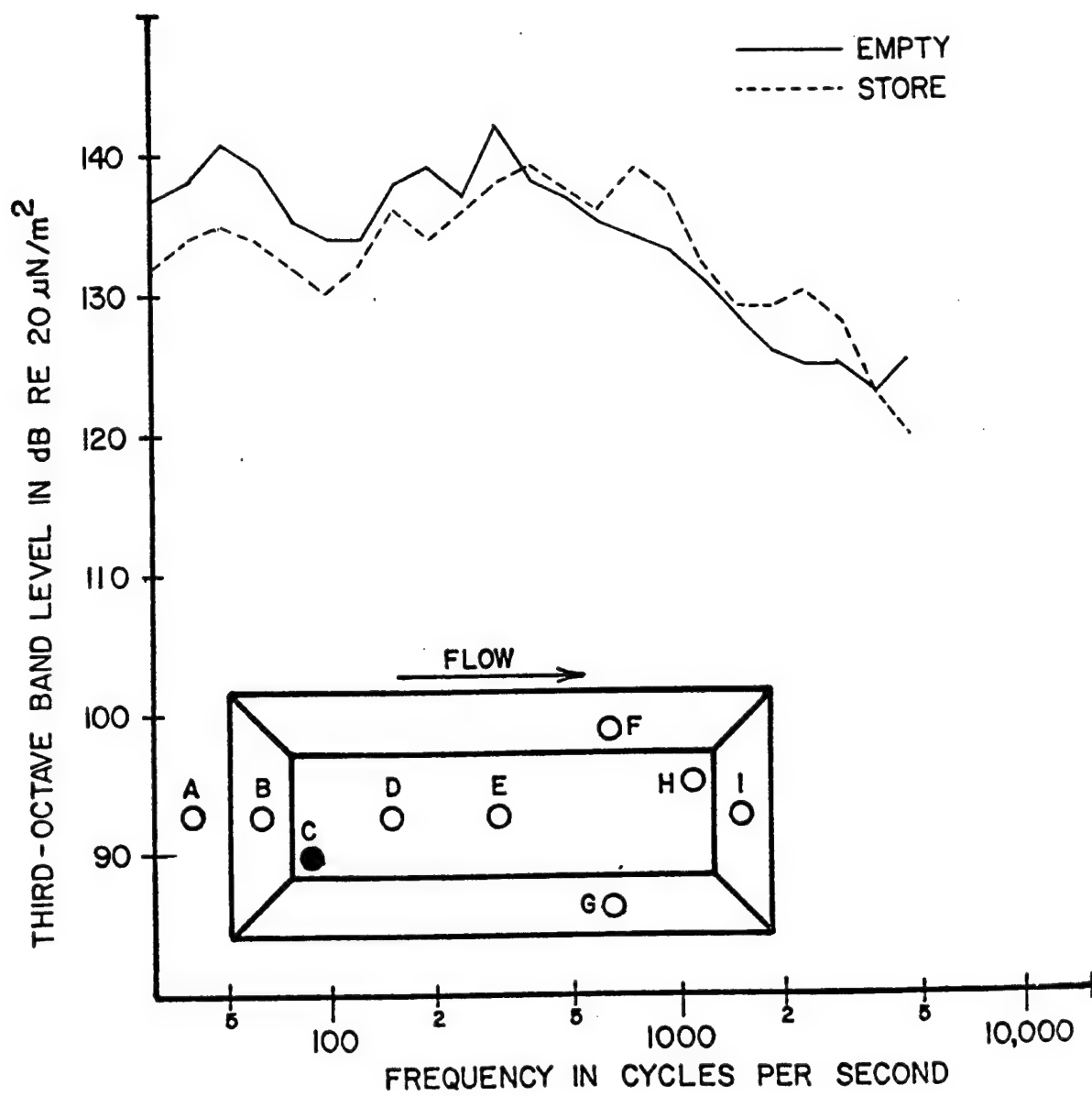


FIGURE 81 COMPARISON OF ONE-THIRD OCTAVE BAND SPECTRA FROM THE
 $L/D = 7$ EMPTY AND STORE CONFIGURATION FOR A MACH NUMBER
 OF 0.82 AND ALTITUDE OF 3,000 FEET

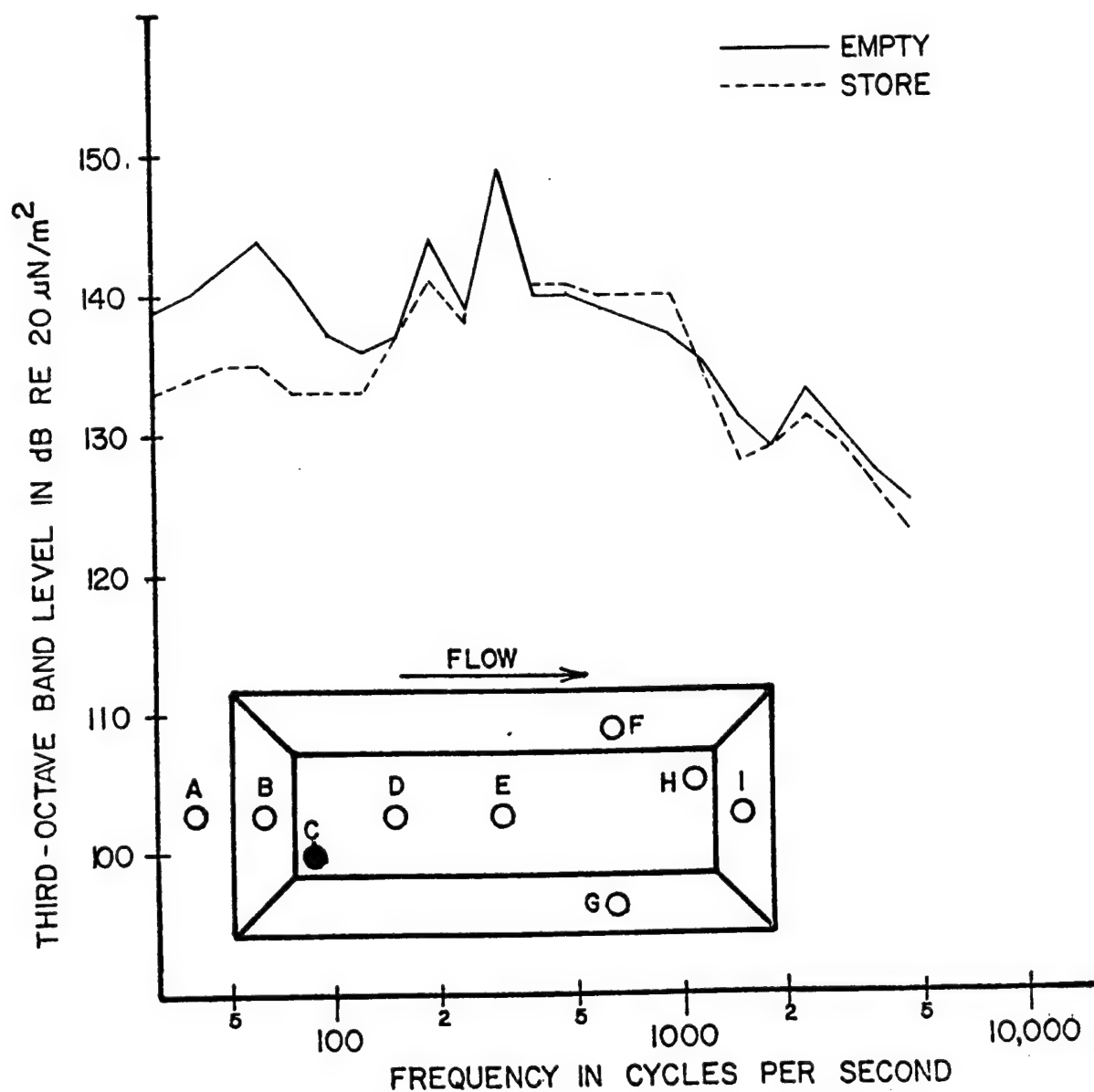


FIGURE 82 COMPARISON OF ONE-THIRD OCTAVE BAND SPECTRA FROM THE L/D = 7 EMPTY AND STORE CONFIGURATION FOR A MACH NUMBER OF 0.93 AND ALTITUDE OF 3,000 FEET

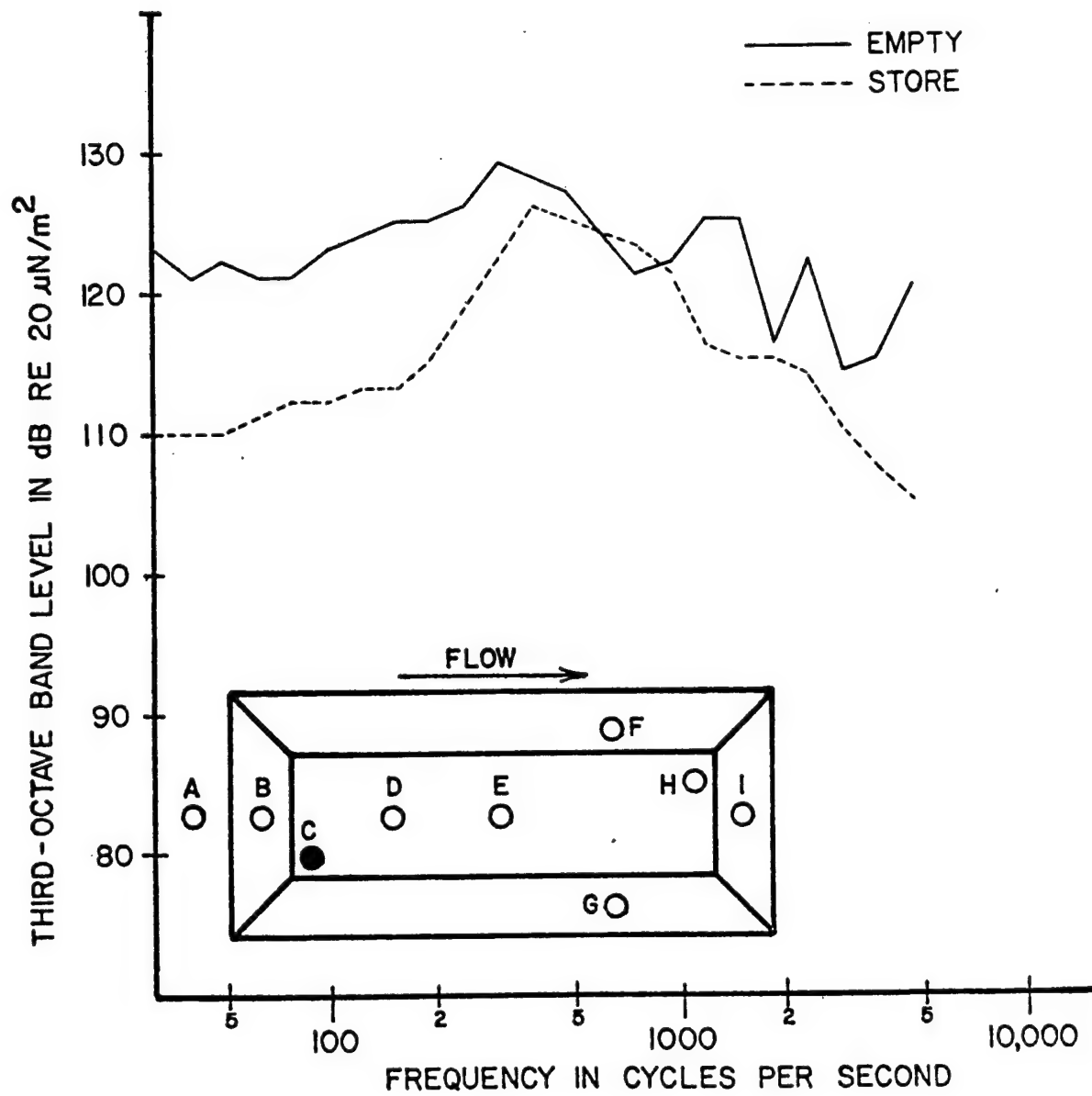


FIGURE 83 COMPARISON OF ONE-THIRD OCTAVE BAND SPECTRA FROM THE L/D = 7 EMPTY AND STORE CONFIGURATION FOR A MACH NUMBER OF 0.61 AND ALTITUDE OF 30,000 FEET

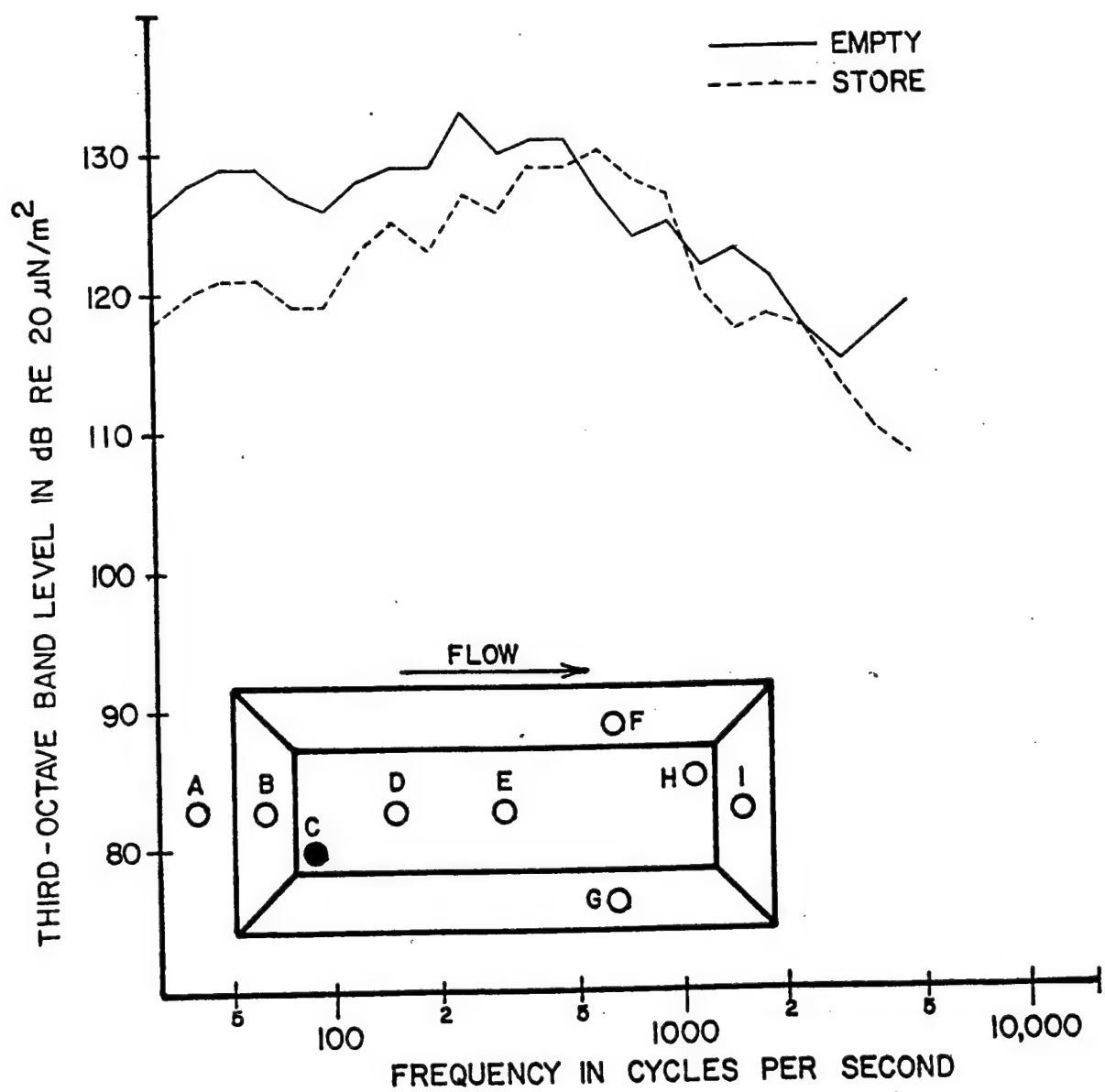


FIGURE 84 COMPARISON OF ONE-THIRD OCTAVE BAND SPECTRA FROM THE
 $L/D = 7$ EMPTY AND STORE CONFIGURATION FOR A MACH NUMBER
 OF 0.82 AND ALTITUDE OF 30,000 FEET

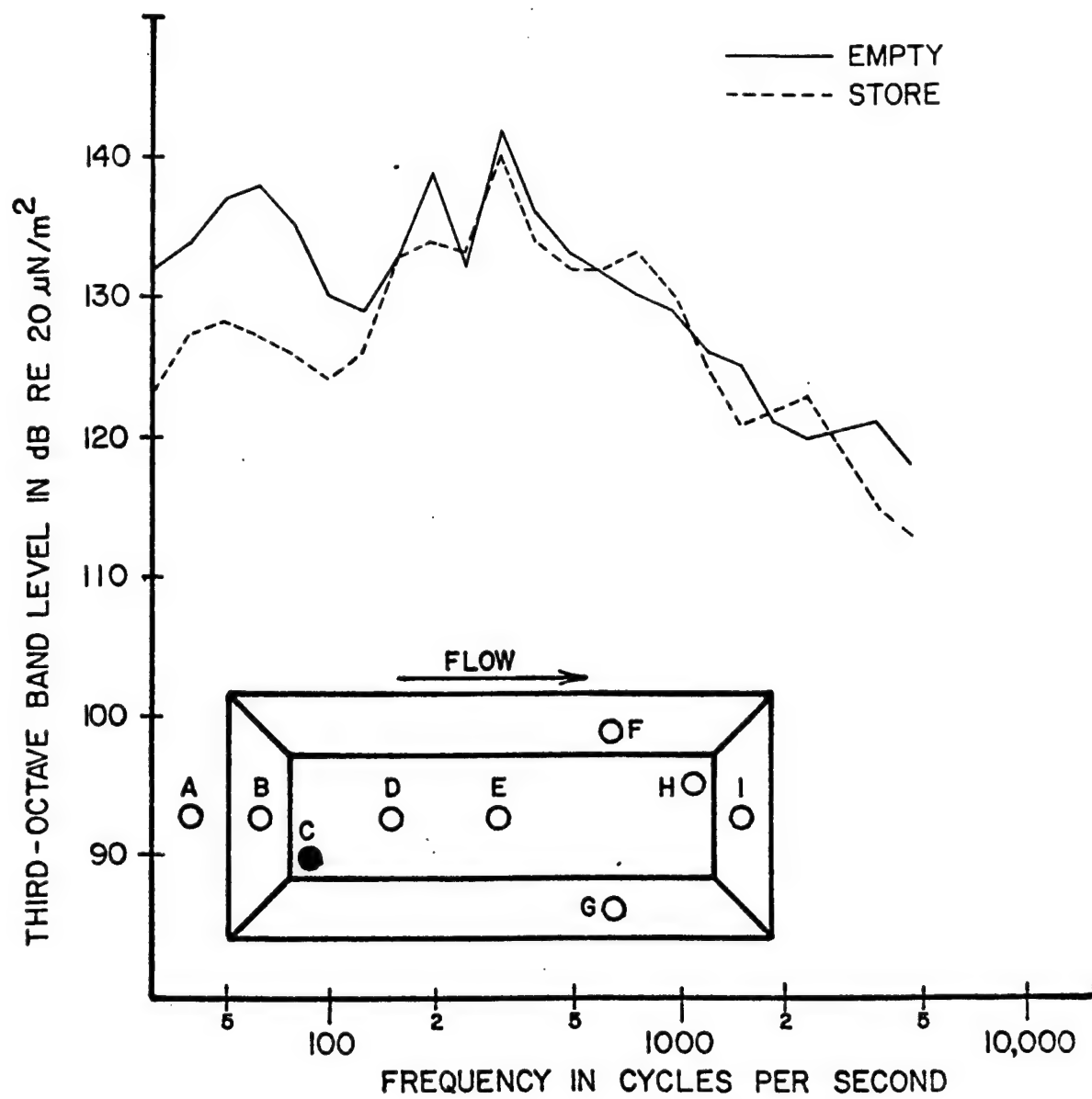


FIGURE 85 COMPARISON OF ONE-THIRD OCTAVE BAND SPECTRA FROM THE L/D = 7 EMPTY AND STORE CONFIGURATION FOR A MACH NUMBER OF 1.05 AND ALTITUDE OF 30,000 FEET

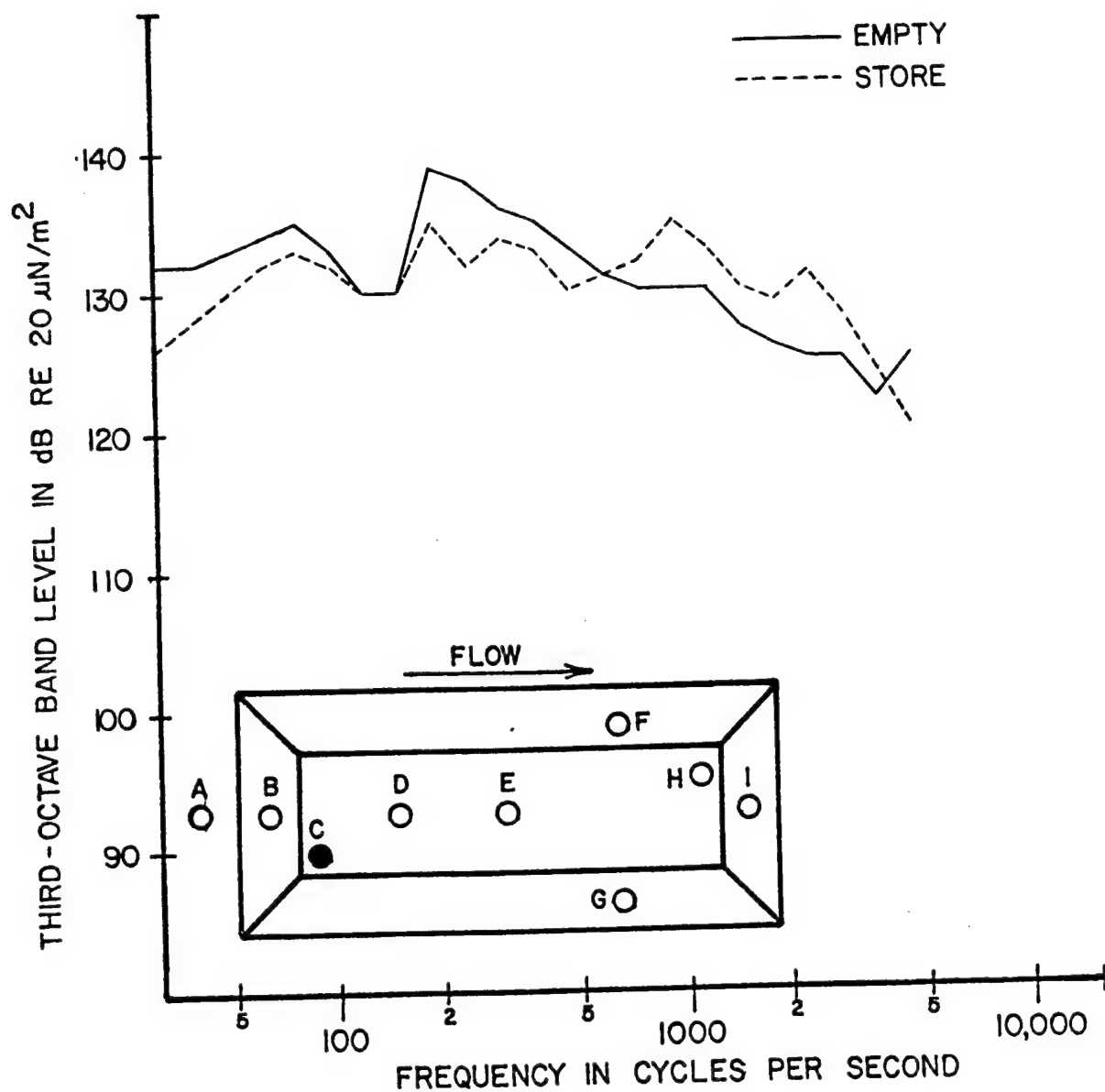


FIGURE 86 COMPARISON OF ONE-THIRD OCTAVE BAND SPECTRA FROM THE
 $L/D = 7$ EMPTY AND STORE CONFIGURATION FOR A MACH NUMBER
OF 1.30 AND ALTITUDE OF 30,000 FEET

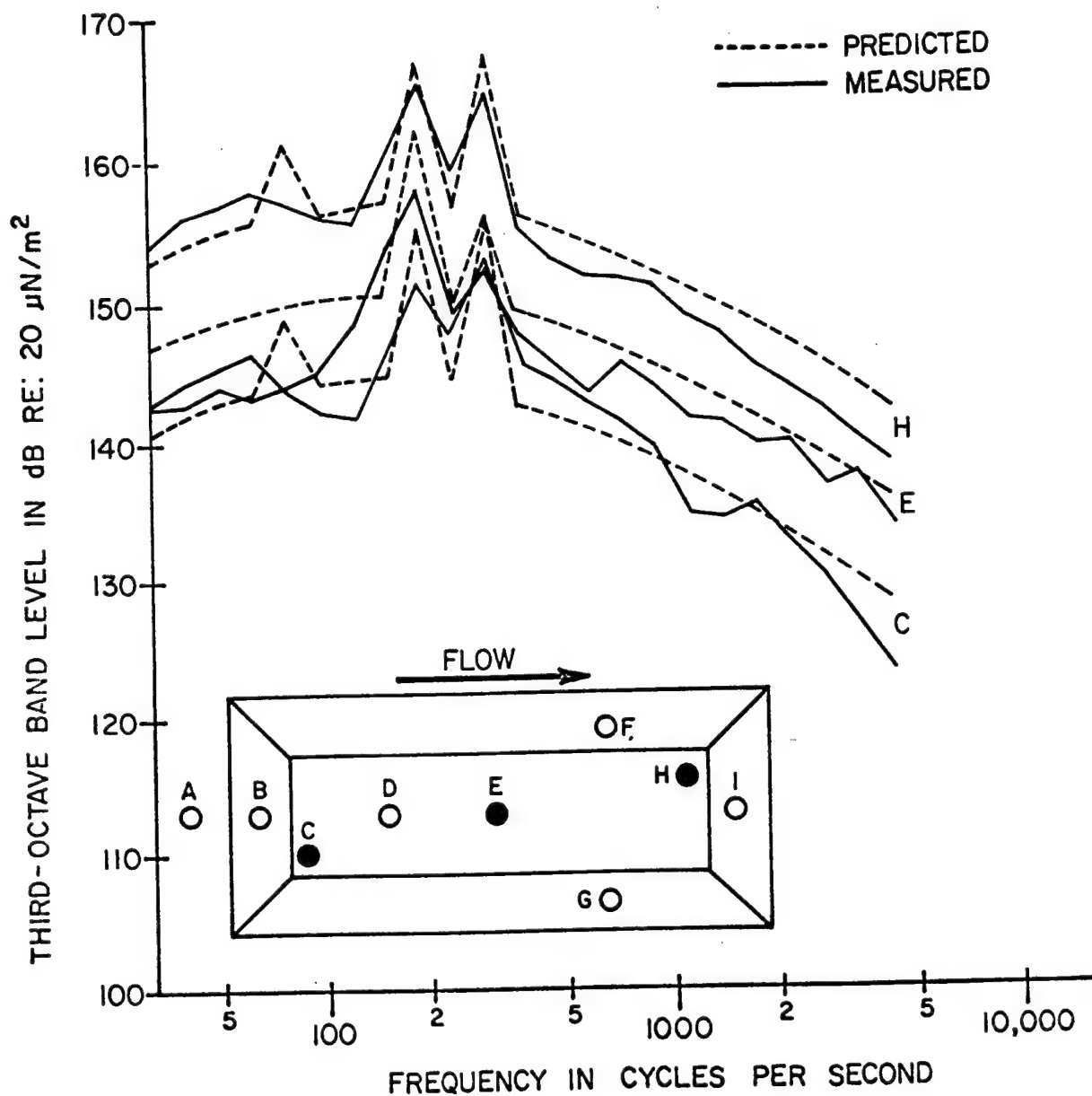


FIGURE 87 COMPARISON OF MEASURED AND PREDICTED ONE-THIRD OCTAVE BAND SPECTRA FOR $L/D = 5$ AND MACH NUMBER 0.82 at 3,000 FEET ALTITUDE

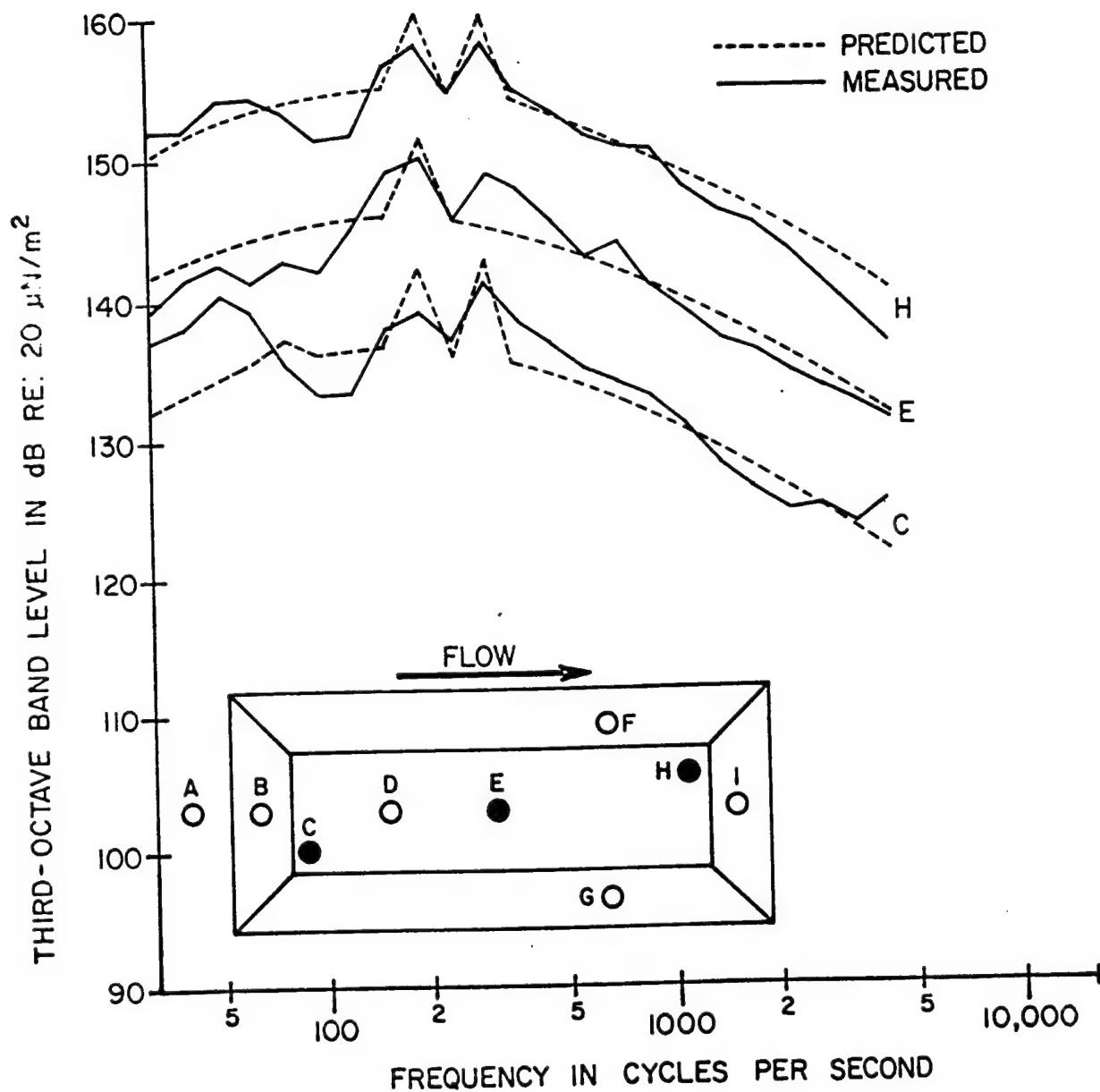


FIGURE 88 COMPARISON OF MEASURED AND PREDICTED ONE-THIRD OCTAVE BAND SPECTRA FOR $L/D = 7$ AND MACH NUMBER 0.82 AT 3,000 FEET ALTITUDE

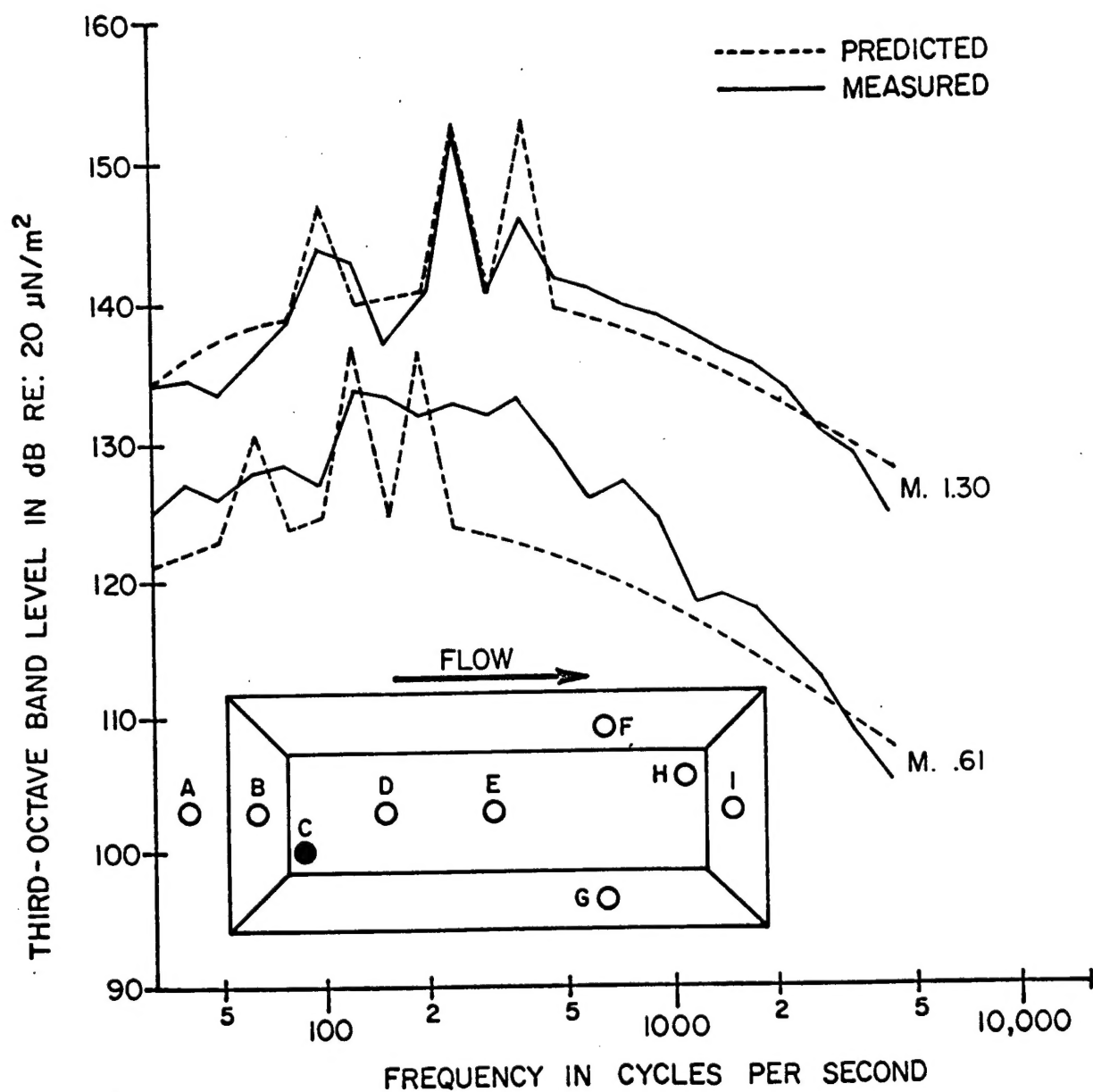


FIGURE 89 COMPARISON OF MEASURED AND PREDICTED ONE-THIRD OCTAVE BAND SPECTRA FOR $L/D = 5$ AT 30,000 FEET ALTITUDE

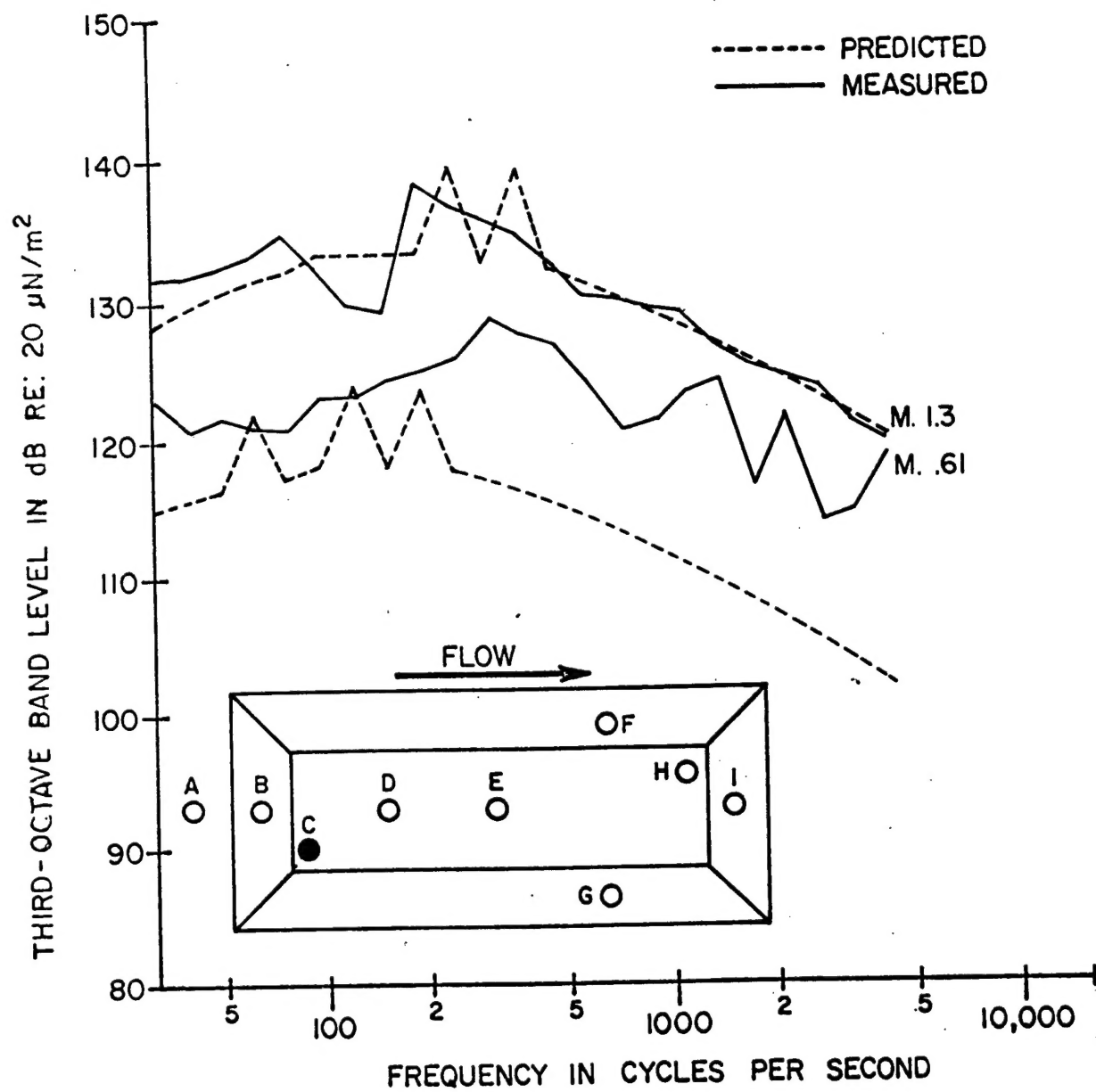


FIGURE 90 COMPARISON OF MEASURED AND PREDICTED ONE-THIRD OCTAVE BAND SPECTRA FOR $L/D = 7$ AT 30,000 FEET ALTITUDE

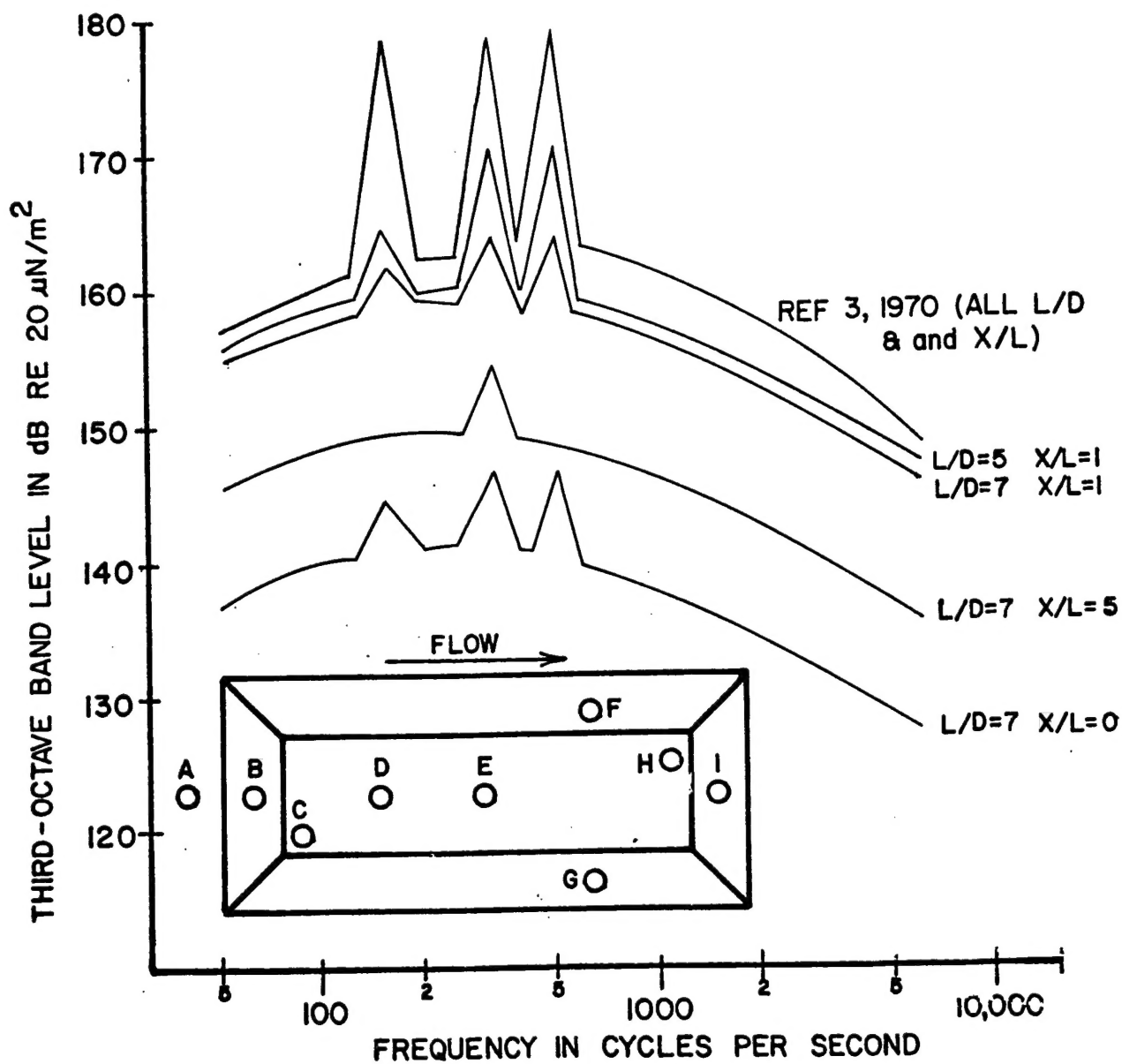


FIGURE 91 COMPARISON OF SPECTRA FROM THE WORKING EXAMPLE AND THE PREDICTION SCHEME FROM REFERENCE 3

REFERENCES

1. Shaw, L. L., Smith, D. L., Talmadge, R. D., Seely, D. R., "Aero Acoustic Environment of a Rectangular Cavity with a Length to Depth Ratio of Four", AFFDL-74-19, FYA. 1974.
2. East, L. F., "Aerodynamical Induced Resonance in Rectangular Cavities", Journal of Vibration and Sound, May 1966.
3. Heller, H. H., Holmes, G., Covert, E. E., "Flow-Induced Pressure Oscillations in Shallow Cavities", AFFDL-TR-70-104, Dec 70.
4. Krishnamurty, K., "Acoustic Radiation from Two-Dimensional Rectangular Cutouts in Aerodynamic Surfaces", NACA Tech Note, 3487, August 1955.
5. Maull, D. J., and East, L. F., "Three-Dimensional Flow in Cavities", Journal of Fluid Mech 16, p 620, 1963.
6. Plumblee, H. D., Gibson, J. S., and Lassiter, L. W., "A Theoretical and Experimental Investigation of the Acoustic Response of Cavities in Aerodynamic Flow", WADD-TR-61-75, 1962.
7. Roshko, A., "Some Measurements of Flow in a Rectangular Cutout", NACA Tech Note 3488, 1955.
8. Rossiter, J. E., "Wind Tunnel Experiments on the Flow Over Rectangular Cavities at Subsonic and Transonic Speeds", RAE Rep Nr 64037, R&M Nr 3438, 1966.
9. Chaump, L. E., Martellucci, A., Monfort, A., "Aeroacoustic Loads Associated with High Beta Re-Entry Vehicles", AFFDL-TR-72-138, May 1973.